Christoph Meraner

Doctoral Thesis

ISBN 978-82-326-4164-2 (printed version)
ISBN 978-82-326-4165-9 (electronic version)
ISSN 1503-8181

Doctoral theses at NTNU, 2019:284

NTNU
Norwegian University of
Science and Technology
Faculty of Engineering
Department of Energy and Process Engineering

NTNU
Norwegian University of
Science and Technology

NTNU

Doctoral theses at NTNU, 2019:284

Christoph Meraner

On the Scalability of a Partially Premixed Low NO_x Hydrogen Burner

NTNU
Norwegian University of
Science and Technology

Christoph Meraner

On the Scalability of a Partially Premixed Low NO_x Hydrogen Burner

Thesis for the degree of Philosophiae Doctor

Trondheim, October 2019

Norwegian University of Science and Technology
Faculty of Engineering
Department of Energy and Process Engineering

NTNU
Norwegian University of
Science and Technology

NTNU
Norwegian University of Science and Technology

Thesis for the degree of Philosophiae Doctor

Faculty of Engineering
Department of Energy and Process Engineering

ISBN 978-82-326-4164-2 (printed version)
ISBN 978-82-326-4165-9 (electronic version)
ISSN 1503-8181

Doctoral theses at NTNU, 2019:284

Printed by Skipnes Kommunikasjon as

Preface

The presented doctoral work was carried out at the Norwegian University of Science and Technology (NTNU) under the supervision of Prof. Dr. Terese Løvås and Dr. Mario Ditaranto.

The doctoral thesis has been produced with support from the BIGCCS Centre, performed under the Norwegian research program Centres for Environment-friendly Energy Research (FME). The authors acknowledge the following partners for their contributions: Gassco, Shell, Statoil, TOTAL, ENGIE and the Research Council of Norway (193816/S60).

The CFD simulations were performed on resources provided by UNINETT Sigma2 - the National Infrastructure for High Performance Computing and Data Storage in Norway.

Abstract

Increasingly stringent regulations on nitric oxide (NO_x) emissions led to the development of various low and ultra low NO_x combustion technologies over the last decades. These technologies are further challenged by the increasing demand for fuel flexibility and rising contribution of non-carbon fuels to the global fuel mix, such as for example hydrogen. Modern burners incorporate complex designs and flow regimes, to address the high burning velocities and temperatures associated with hydrogen and hydrogen rich fuels, allowing stable combustion and low NO_x emissions. The development process of such burners requires the scaling of the burner geometry to facilitate simulations and testing at laboratory scale. Scaling is conducted by employing scaling laws, that aim to preserve relevant burner characteristics.

The present doctoral thesis investigates the effect of the most commonly used scaling laws, constant velocity and constant residence time scaling, on complex burner designs. Both scaling laws are derived based on "simple" flames that can be defined by a single length and velocity scale. Previous studies have, however, indicated that such global scaling laws fail when applied to complex industrial burners, where flow conditions can vary significantly for different burner regions. The main focus of the present study is, therefore, the analysis of local effects on the combustion and NO_x characteristics. The analysis was conducted based on a partially premixed bluff body (PPBB) burner, which incorporates an inner and outer recirculation zone, stagnation point flow, staged fuel injection and varying degree of partial premixing; all typical features of complex, modern burner designs.

A numerical model of the PPBB burner was developed and validated against experimental data. The simulation of turbulent combustion processes, including detailed combustion kinetics, heat radiation and NO_x formation, at various burner scales is computational demanding. Hence, a compromise between model accuracy and costs is sought after. Considering this, a non reacting flow configuration of the burner was investigated first, which made it possible to conduct the CFD simulations with a wide variety of different turbulence models, ranging from steady state Reynolds averaged (RANS) to transient scale resolving simulations. Varying the complexity of the turbulence model allowed the identification of model requirements and exposed limitations for the cost effective RANS models. The non reactive model was, thereupon, further extended to incorporate species transport, detailed hydrogen combustion kinetics, turbulence chemistry interaction, radiation and NO_x formation. The extended model was employed to conduct twelve simulations of different operational conditions, i.e., secondary fuel fraction and thermal loads. Furthermore, a postprocessing routine was developed to incorporate scatter data, obtained from the CFD simulations, in combustion regime diagrams, leading to a more refined representation of the burner characteristics. Finally the burner geometry was scaled based on the constant velocity as well as the constant residence time scaling approach, and CFD simulations at various scales in the range of 10 kW to 500 kW were conducted. The simulations were used to study the effect of the two different scaling laws on the local NO_x formation rate and flame characteristics, and to compare the CFD prediction to scaling theory. The fluid domain was, furthermore, decomposed in order to investigate different burner regions, and their contribution to the NO_x formation individually. Based on the identified burner regions, work on a reactor network of the PPBB burner was initiated.

The non/reacting flow simulations showed, for all investigated turbulence models, good agreement between the simulated and the measured recirculation zone length. However, all RANS models generally overpredicted the velocity magnitudes, especially within the inner recirculation zone, while scaling resolving simulations resulted in a reasonable good agreement between simulation and experiment. The predicted NO_x emissions, for a wide range of operational conditions, were between +10% and -20% of the measured data, underpredicting them in average by 7%. The model was, furthermore, able to predict the overall NO_x trend for varying thermal loads, while it failed to reproduce the effect of a varying secondary fuel fraction on the NO_x emissions at low thermal loads, of 10 kW.

The detailed analysis of the flame characteristics in CFD based combustion regime diagrams revealed that primary fuel burns in a multi regime mode, mainly in the thin reaction zone regime, spanning a wide range of equivalence ratios, while secondary fuel is burned closer to the global and stoichiometric equivalence ratio. The simulations showed, furthermore, a transition from a fuel lean to a fuel rich mixture in the inner recirculation zone, when the secondary fuel fraction is increased from 0% to 30%. The numerical model was utilized to simulate the burner at various scales in the range of 10 kW to 500 kW. Constant velocity scaling leads to lower Karlovitz numbers and ultimately to a transition, for large parts of the flame, from the thin reaction zone regime to the corrugated flamelet regime. Constant residence time scaling, on the other hand, preserves the global Damköhler number. However, a significant part of the flame follows a constant Karlovitz number, close to unity, which is not expected based on scaling theory. Constant velocity scaling leads due to the larger volumes and residence times to overall higher NO_x emissions, with exception of the inner recirculation zone, even though constant residence time leads locally to the larger mean volumetric formation rates. An interesting finding, regarding flame stability, was found for constant velocity scaling, which led to the sudden breakup of the inner recirculation zone at a scale in-between 450 kW and 500 kW, while the flame is stable at 500 kW, when con-

stant residence time scaling is applied.

Acknowledgements

First and foremost, I would like to thank my main supervisor Prof. Terese Løvås for giving me the opportunity to work on this Ph.D. project and for believing in me throughout the whole journey. She gave me all the freedom I needed to grow as an independent researcher but always was ready to provide encouragement, motivation and from time to time a push in the right direction, if needed.

My co-supervisor Mario Ditaranto was always there for my questions and gave me valuable insights in the experiments that formed the basis for the model development. He also equipped me with the right tools to bring my ideas and thoughts to paper.

Special thanks to Tian Li, who always puts others first and never seemed to get tired of all the questions I had. Thank you for your support and the knowledge you shared with me. Without you I would not have been able to finish this project.

Fredrik Grøvdal, Jonas Krüger and Jingyuan Zhang, thank you for enduring me as your office neighbour and for all the interesting and fruitful discussions, on- and off-topic.

I would like to thank Karl Oskar Pires Bjørgen, Kathrin Weber, and Ning Guo for always having an open ear for my struggles and frustrations. Thank you for motivating and encouraging me.

To all my colleagues, thank you for creating such a friendly and enjoyable working environment. I'm very grateful for all the friends I made in the ComKin and ComCake group.

Above all I would like to thank my family Marie, Jonas and Filip. You helped me not to lose sight of the things that truly matter in life. Being a Ph.D.-student impacts you more than most other jobs. Becoming a father, however, is on a completely other scale. I'm grateful for every moment I have with you and would not trade it for anything else.

Bente and Trond, no matter what it was, being it building a home office in the mountains or on an island at the polar circle, travelling on short notice 500 km just to help at home, while I was working during weekends or travelling to conferences, you always supported me in my ambitions. I would like to thank you for that.

Last but not least, I would like to thank my parents, Johanna and Walter, my sister Marion, and the rest of my family and friends back home in Südtirol. It's not always easy to be so far apart, but it was you that taught me the determination and persistence, that was needed to finish the Ph.D. project.

To Jonas and Filip.

Scientific contributions

Selected publications included in this thesis

This doctoral thesis is based on the work presented in the following publications, which are referred to in the text by Roman numerals:

I. **Meraner C**, Li T, Ditaranto M, Løvås T. Cold flow characteristics of a novel bluff body hydrogen burner. *International Journal of Hydrogen Energy*, 43(14):7155-68, 2018. doi:10.1016/j.ijhydene.2018.02.062.

II. **Meraner C**, Li T, Ditaranto M, Løvås T. Combustion and NO_x emission characteristics of a bluff body hydrogen burner. *Energy and Fuels*, 33(5):4598-4610, 2019, doi:10.1021/acs.energyfuels.9b00313

III. **Meraner C**, Li T, Ditaranto M, Løvås T. Effects of scaling laws on the combustion and NO_x characteristics of hydrogen burners. *Submitted to Combustion and Flame*

The author's contribution to the selected publication

The scientific publications forming the basis of this doctoral thesis are co-authored. The contribution of the author to the publications is described in what follows.

Paper I. The author reviewed relevant literature, which provides the background for the publication and puts the conducted work into context with current state of the art research. Based on the findings of the literature review, the author decided on a suitable modelling approach in accordance with the scope and objective that was set for the work. The author created the numerical mesh, set up the numerical model and conducted the simulations in ANSYS Academic Fluent, Release 18.2. The author decided, furthermore, in cooperation with the co-authors on the operational conditions and boundaries for the computational simulations. The author carried the post processing of the data out and was, in cooperation with the co-authors, responsible for writing the paper, as well as interpreting and discussing the results.

Paper II. The author extended the numerical model from Paper I to incorporate hydrogen combustion, thermal radiation and NO_x formation. The author validated the model against experimental data for several operational conditions and conducted sensitivity simulations where required by the uncertainty in the given boundary conditions/submodels. The author developed and implemented, furthermore, a new post processing routine based on Python and Cantera to generate combustion regime diagrams and hexbin plots, a form of bivariate histogram, based on the obtained simulation data. The author wrote the paper in cooperation with the co-authors and was responsible for interpreting and discussing the results.

Paper III. The author reviewed relevant literature and decided on the scaling laws that were used for the study. The author, furthermore, investigated the theoretical effect of these scaling laws on the global Reynolds, Damköhler and Karlovitz number. All computational simulations were conducted by the author, utilizing the numerical model from Paper II. The scaled geometry and updated numerical grids for the simulations were prepared by the author. The author, furthermore, extended the post processing routine in Python/Cantera to include probability density distributions in the combustion regime diagrams and was responsible for post processing and interpreting all conducted simulations. The paper was written by the author in cooperation with the co-authors.

Additional publications and conference presentations

- Grøvdal F, **Meraner C**, Sannan S, Chen J-Y, Løvås T. Dimensional decomposition of turbulent reacting flows. (Prepared for submission)

- **Meraner C**, Ditaranto M, Løvås T. Combustion characteristics of a partial premixed low NO_x hydrogen burner. 37th International Symposium on Combustion. Dublin 2018. (Visual presentation)

- **Meraner C**, Ditaranto M, Løvås T. Characteristics of a partial premixed bluff body low NO_x burner. SIAM - 16th International Conference on Numerical Combustion. Orlando 2017. (Oral presentation)

- **Meraner C**, Ditaranto M, Løvås T. Numerical analysis of a downscaled partial premixed bluff body low NO_x burner. 36th International Symposium on Combustion. Seoul 2016. (Visual presentation)

Contents

Nomenclature

Symbols

c	normalized progress variable (-)
C_μ	model constant (-)
C_γ	model constant (-)
C_τ	model constant (-)
d	nozzle diameter (m)
D_0	characteristic burner diameter (m)
$D_{i,j}$	multicomponent mass diffusion coefficient (m^{2}s^{-1})
$\mathcal{D}_{ij}$	binary diffusion coefficient (m^{2}s^{-1})
G_{FO}	flame index (-)
k	turbulent kinetic energy (m^2 s^{-2})
K	proportionality constant (-)
L, l	length scale (m)
$\dot{m}$	mass flow rate (kg s^{-1})
Q	thermal input, heat loss (W)
$\bar{R}_i$	mean reaction rate for species i (kg m^{-3}s^{-1})
u	initial jet velocity (m s^{-1})

U_0	burner characteristic velocity (m s^{-1})
x	coordinate (-)
X_i	volume fraction of species i (-)
y^+	dimensionless wall distance (-)
Y	mass fraction (-)
$\tilde{Y}_i$	mean mass fraction of species i (-)
Y_i^*	mass fraction of species i in the fine-structures (-)
Y_i^0	mass fraction of species i in the surrounding fluid (-)
Z_{stoich}	stoichiometric mixture fraction (-)

Greek

γ_λ	mass fraction of the fine-structures (-)
ϵ	turbulent dissipation rate (m^{2}s^{-3}))
μ_t	turbulent viscosity (kg m^{-1} s^{-1})
ν	kinematic viscosity (m^2 s^{-1})
ρ	density (kg m^{-3})
$\bar{\rho}$	mean density (kg m^{-3})
τ^*	mean residence time in the fine-structures (s)
ϕ	equivalence ratio (-)

Subscript

rt	constant residence time
v	constant velocity
$\bar{}$	average value
$\tilde{}$	mass-weighted average value

Superscript

*	scaled property/fine scale property

Abbreviations

CCS	carbon capture and storage
CFD	computational fluid dynamic
CIVB	combustion induced vortex breakdown
DNS	direct numerical simulation
EBU	eddy breakup
EDC	eddy dissipation concept
FGM	flamelet generated manifold
FL	flame
IPF	immediate post flame
IRZ	inner recirculation zone
LBO	lean blowout
LES	large eddy simulation
MFC	mass flow controller
MILD	moderate or intense low-oxygen dilution
NO_x	nitrogen oxides
ORZ	outer recirculation zone
PDF	probability density function
PF	post flame
PFR	plug flow reactor
PIV	particle image velocimetry
PPBB	partially premixed bluff body
PSR	perfectly stirred reactor
RANS	Reynolds averaged Navier-Stokes
URANS	unsteady Reynolds averaged Navier-Stokes
WJ	wall jet

Chapter 1

Introduction

1.1 Motivation

Increasingly stringent regulations on the emission of nitrogen oxides (NO_x) motivated the development of various low and ultra low NO_x burners, throughout the last decades. However, changing requirements to combustion and industrial high temperature processes, related to the transition towards a sustainable energy systems, continue to challenge burner designs. Fuel flexibility and the use of hydrogen and hydrogen-rich synthetic fuels play an important role in this context [34, 131, 137].

An example for the combustion of hydrogen-rich fuels is pre-combustion carbon capture and storage (CCS). This technique utilizes either a gasification or reforming process to obtain syngas (i.e., carbon monoxide (CO) and hydrogen (H_2)) from solid, liquid or gaseous fuels. The CO in the syngas is in a subsequent water-gas-shift reaction, to large parts, converted to carbon dioxide (CO_2) which can be captured and stored before the remaining hydrogen-rich gas is combusted. Since the CCS process takes place before the combustion, and hence in absence of nitrogen, it is not required to use potentially harmful amines for pre-combustion CCS. Another benefit of pre-combustion CCS is the low relative concentration of CO in the shifted syngas, which consequently leads to low CO_2 emissions from the combustion [26, 27]. However, the reduced CO_2 emissions come at the cost of an increased flame temperature, which promotes the formation of NO_x, and an increased risk of flashback, due to the high reactivity of hydrogen (H_2). Pre-combustion CCS requires, therefore, the employment of burners that are capable of mitigating the NO_x formation caused by the elevated flame temperatures while maintaining stable combustion, ideally for a wide range of CO to H_2 ratios.

A burner design that aims to address these issues is the partially premixed bluff body (PPBB) burner developed by Spangelo et al. [119]. The PPBB burner has in recent years been investigated experimentally by Dutka et al. [35–38] and has shown promising results at laboratory scale with regards to NO_x emissions. However, the data obtained in the experimental campaigns is limited to global species measurements, including NO_x, for the burner firing into a combustion chamber and particle image velocimetry (PIV) for the operation without chamber. Furthermore, the scalability of the burner concept to larger, eventually industrial, scales has not been addressed by the experiments.

In order to assess the burner scalability, scaling laws need to be employed that ideally preserve the burner characteristics at all applicable scales. However, these laws cannot easily be derived by similarity theory, as many of the scaling parameters are mutually incompatible. Hence, partial scaling, as described by Spalding et al. [117] and Beér [9] needs to be employed. The requirement of partial scaling led to a large variety of scaling laws, found in the literature. The majority of these scaling laws, however, concern scaling effects at constant thermal loads [125] and fail to correlate NO_x emissions to different burner scales [55]. In this field much less work has been done and most studies rely on either constant velocity scaling or constant residence time scaling; both global scaling laws. Only very few studies consider that different burner regions, especially in modern complex designs, are likely to exhibit local scaling effects [21, 55].

The limited data and the lack of understanding the burner scalability, as well as the general knowledge gap regarding local scaling effects, motivated the numerical and theoretical investigation of the PPBB burner in the present doctoral thesis. The work aims to provide a more complete picture of the burner characteristics and scaling effects on complex burners.

1.2 Objective

The main objective of the present work is to provide missing information with regard to the combustion characteristics of the PPBB burner and its scalability. The work aims, furthermore, to fill the knowledge gap in the general understanding of localised scaling effects. The objective of the present thesis is, on this basis, divided into three parts which are as follows:

1. Establish a numerical model of the PPBB burner which is validated against experimental data obtained by Dutka et al. [35–38]. The aim of the numerical model is to investigate NO_x emissions at different burner scales, including large scale simulations at a thermal input of 500 kW. Controlling the model complexity and the associated computational costs is therefore a

key element in the model development.

2. Build an understanding of the governing fluid and thermodynamic characteristics of the PPBB burner at laboratory scale. This includes the effect varying operational conditions in terms of secondary fuel fraction and thermal load on the NO_x emissions.

3. Scale the burner incrementally up to semi-industrial scales in order to investigate the scalability of the PPBB burner concept and to study the global and local effects of different scaling laws on the combustion and NO_x characteristics of the burner. Special attention is given to the governing burner characteristics identified at laboratory scale. An important aspect of this effort is the identification of critical thermal loads that potentially limit the scalability.

1.3 Scope

The scope of the present doctoral thesis consists of the implementation and validation of a numerical model in the ANSYS Academic Fluent, Release 18.2 framework, the conduction of numerical simulation at various operational conditions and burner scales, and the application of different scaling laws in a numerical as well as a theoretical framework. The extended scope incorporates, furthermore, the development of a low order network model of the burner based on the Cantera [48] software package, which aims to preserve the main scaling characteristics while allowing to investigate the effect of isolated parameters such as the recirculation mass flow rate.

The model development comprises the identification of suitable submodels for the treatment of a wide range of physical phenomena, with the most important being turbulence, turbulence-chemistry interaction, boundary layer flow, combustion kinetics, radiation and NO_x formation. Important considerations for the model selection are, among others, the balance between model accuracy and model complexity and cost, as well as the compatibility of the different submodels. Considerations of the computational costs are, furthermore, crucial for the selection of the overall modelling approach, especially regarding the model application for large scale simulations of the burner. A detailed simulation of the PPBB burner by means of scale resolving simulations is therefore not prioritized in the present work as the computational costs associated with such models are prohibitive for their application at large burner scales. The scope is, furthermore, limited to the investigation of pure hydrogen as fuel which allows a considerable reduction in the complexity of the combustion and NO_x kinetics, but at the same time represents a challenging fuel for the burner.

The computational fluid dynamic (CFD) model of the PPBB burner forms the basis for the study of the combustion and NO_x characteristics. However, the quantitative analysis of NO_x emissions is ambitious given the limited experimental data available for the PPBB burner and the highly sensitive nature of NO_x formation regarding variations in temperature and radical concentrations. The scope of the present work focuses therefore on the qualitative analysis of NO_x trends, both with regard to varying operational conditions as well as varying burner scales.

In order to investigate the burner performance at larger scales, scaling laws need to be employed to adjust the burner length scales to the increased mass flow rates. The scope of the present work includes the study of two different scaling laws, namely constant velocity and constant residence time scaling, and their effect on the global Damköhler and Karlovitz number based on scaling theory. A more comprehensive analysis of their local effects is conducted based on detailed data obtained from the CFD simulations.

The extended scope of the present thesis includes scale resolving CFD simulations of the burner at laboratory scale. The main purpose of these simulations is to investigate the feasibility of such simulations for the PPBB burner and to outline a possible simulation strategy for future work. A further extension to the original scope of the present work is the establishment of a reactor network which represents a lower order model of the PPBB burner. The scope for this activity includes the implementation of the reactor network in the Cantera framework. The reactor network relies on the a priori definition of reactor volumes and certain characteristic mass flow rates, such as the recirculation mass flow rate. These data are obtained from the detailed CFD simulations.

1.4 Organization of the thesis

The present thesis is structured into six chapters. At this point the motivation, objective and scope of the present study were outlined in chapter 1.

The following chapter 2 provides the background for the present work, introduces the reader to the PPBB burner design and sets the study in context with relevant literature. Furthermore, a short overview of the relevant fundamentals for hydrogen combustion, NO_x formation, simulation of turbulent flames and scaling of burners, is given.

Chapter 3 presents the numerical model that was developed to simulate the combustion and NO_x formation in the PPBB burner.

The core of the research, which is published in three papers, collected in the present doctoral thesis, is summarized in chapter 4.

Additional work, that has been conducted during the course of the Ph.D. project and has reached considerable progress, but is not yet ready to be published in a scientific journal, is presented in chapter 5.

Finally the main conclusions and outlook for future work is presented in chapter 6.

Chapter 2

Background and fundamentals

This chapter presents the background for the conducted work and sets it in context with relevant literature. A brief overview of the fundamentals for hydrogen combustion and NO_x formation is provided. The emphasis is to outline important aspects of these topics with regard to the design and numerical simulation of the burner and ultimately their implications on the scaling of the burner. Available modelling approaches for the simulation of turbulent flames is presented and considerations that need to be made in the model selection process are discussed. Finally a review of scaling laws is provided.

2.1 Burner principles

A burner is a device that facilitates the controlled mixing and stable combustion of a specified amount of reactants (i.e., fuel and oxidizer) in a controlled region (i.e., in most cases with a controlled flame shape). Based on this definition a set of requirements can be established for any burner design, which are: metering of fuel and air, controlling of the mixing processes, stabilizing the flame and controlling the flame shape. Controlling the emissions of pollutant can be seen as an additional criteria for modern burner designs. A comprehensive review on burner designs can also be found in the John Zink combustion handbook [7], which is used as basis for the following discussion.

The first step in controlling combustion is to control the amount of fuel and air available to it. The metering system of a burner needs therefore to be designed such that the amount of fuel and air delivered to the flame region can be controlled, typically independent from each other. This allows to control the thermal input of the burner as well as the global equivalence ratio. Modern burner designs often employ multiple fuel ports, in order to control the fuel distribution to specific burner regions individually. The design of the fuel metering plays also an important role regarding combustion instabilities, as fluctuations in the fuel supply, for example due to pressure fluctuations, lead to fluctuation in heat release. If the local pressure and heat release fluctuations are in-phase a self-amplifying cycle, i.e. thermo-acoustic instability, is established [101].

The global equivalence ratio is, as already mentioned, controlled by the metering system. The local equivalence ratio, on the other hand, depends on the mixing processes. Mixing, furthermore, controls the local ratio between unburned and burned gas. Optimizing local mixing is therefore one of the major tools for the reduction of pollutant emissions. Based on the degree of mixing fuel and air before reaching the flame anchor point we distinguish between non-premixed, premixed and partially premixed burners. We can furthermore, distinguish between different techniques to facilitate and mixing. These are: entrainment/co-flow mixing, cross flow mixing and turbulence generation.

Entrainment occurs when a jet (e.g. round or wall jet) with higher momentum is released into a quiescent fluid. This can be a fuel jet released into air but also an unburned mixture released into the flue gas containing environment of a combustion chamber. Energy from the jet is transferred to the surrounding fluid. This leads to a decrease in the jet velocity at the same time the jet spreads, i.e. it increases its mass, by entraining more and more of the surrounding fluid, which leads to mixing of the two fluids. A well known example for a premixed burner that utilizes this concept is the Bunsen burner. The entrainment can further be enhanced, utilizing the so called Coanda effect by employing wall jets along a surface with a streamwise curvature, which increases the turbulence in the jet and hence the entrainment. This concept is for example used in tulip shaped Coanda flares [89]. If both fluids have a momentum in the same direction we talk about co-flow mixing. The entrainment, and hence mixing, is proportional to mass velocity difference between the two streams. Co-flow mixing is therefore slow when the difference is small. A more efficient mixing can be achieved in a cross-flow configuration, where the two streams intersect in an angle to each other, which leads to large shear energy and turbulent mixing. Turbulent mixing can also be achieved by adding local obstructions (e.g. bluff bodies), which generate a turbulent wake. This technique is often combined with co-flow or cross-flow fuel injections. An example for this is the fuel lance in the SEV burner of Alstom's GT24/GT26 gas turbine series, which is placed in the wake of wedge shaped vortex generators [40].

The most important function of a burner is to provide a specific and stable flame anchor point, in which fresh mixture is continuously ignited. In general two mechanisms for ignition at the flame anchor point can be distinguished, flame propagation and autoignition. An example for the latter type of flame stabilization can be seen in the vitiated coflow burner by Cabra et al. [14]. The hot products of the vitiated coflow are entrained into a central hydrogen-nitrogen jet and which leads after to autoignition of the jet at a certain lift-off height. The coflow burner by Cabra et al. is used to study combustion and validate numerical models. An example of autoignition in "real" burners is the aforementioned SEV burner. The SEV burner utilizes the exhaust gas of an upstream located lean burner as oxidizer. The elevated oxidizer temperature is sufficiently high to cause autoignition in the central, high velocity, region of the SEV burner, while the shear layers formed at the burner exit allow flame propagation [144]. An important difference between the two mechanisms is that autoignition allows flame stabilization in regions where the flow velocity exceeds the flame propagation speed. However, flame propagation is, despite this apparent disadvantages compared to autoignition, the most commonly used mechanism, as it can be facilitated by controlling the flow field. The most common burner designs for this type of flame stabilization are swirl burners and bluff body burners, or a combination of both. Bluff body burners stabilize the flame in the wake flow behind a single or multiple flame holders. The wake is characterized by lower velocities and recirculation of combustion products, and hence has favourable conditions for the flame stabilization. A typical design for bluff body burners is an axisymmetric central bluff body. These burners generate an inner as well as an outer recirculation zone, which is comparable to the axial and radial velocity field of swirl burners. The inner recirculation zone, not only provides low velocity regions, but also transports hot combustion products upstream and increases turbulence, leading to an increased flame speed. The main difference between bluff body and swirl burners is that the inner recirculation zone in swirl burners is not formed by a bluff body, but induced by changes in the vorticity field. Swirl burners use tangential or axial vanes to generate axial vorticity. The axial vorticity is partially converted to azimuthal vorticity when the flow follows an increase of the burner cross-section. The generation of azimuthal vorticity induces, following the Biot-Savart law, a axial velocity opposed to the main flow direction. A more detailed description of this mechanism can for example be found in the work by Batchelor [6].

2.2 The PPBB burner

This section introduces the reader to the PPBB burner concept, which has been shortly touched on in chapter 1. The PPBB burner was originally developed as a propane and natural gas burner for the use in boilers and furnaces. However, its design allows the adaptation to a wide range of different fuel compositions during operation. This makes the PPBB burner a promising candidate for the low NO_x combustion of syngas with high CO and H_2 concentrations. The PPBB burner is, despite its unique design, furthermore of interest as study case for the investigation of NO_x emission scaling since it incorporates many attributes that are commonly found in modern burners, among others a flame stabilizing inner recirculation zone, flue gas recirculation, staged fuel injection and a varying degree of partial premixing.

Figure 2.1 shows a cross sectional view of the PPBB burner. The burner consists of a central lance that holds a frustum shaped conical bluff body. The bluff body is partially submerged in the burner housing. The lance height, defined as the distance from the bluff body trailing edge to the burner throat, is variable. This is one of the main mechanisms to adapt the burner to changing fuel mixtures. The variable lance height allows the modification of the flow velocities independent from the mass flow rates. The diameter of the bluff body is, however, larger than the inner housing diameter at the burner throat. It is therefore not possible to submerge the bluff body completely in the burner housing, which would correspond to a more "classical" bluff body burner design as investigated for example by Dawson et al. [32] and Kariuki et al. [60]. The bluff body holds in total twelve fuel ports. The ports are divided into eight primary fuel ports, located inside the burner housing, and four secondary fuel ports, located outside of the housing, downstream of the burner throat. The primary fuel ports are 2 mm in diameter, while the secondary fuel ports are 1.3 mm. The fuel ports are evenly distributed along the bluff body circumference. The secondary fuel ports are, in angular direction, offset to the primary fuel ports by 22.5°, which places one secondary fuel port in between every second pair of primary fuel ports. The port count and diameters have been investigated by Spangelo [118] and optimized for low NO_x emissions. However, the optimization was conducted for the operation with propane. In the current design only the diameters were adjusted specifically for hydrogen combustion, while the port count and distribution is unchanged. This provides the possibility for further improvements of the burner design, which is also indicated by the findings in Paper III.

Figure 2.2 illustrates the primary flow pattern generated by the PPBB burner. Air is provided through the annular duct formed by the burner housing and the lance/bluff body. The air stream is accelerated in the converging section of the burner and mixed with fuel, which is provided through the primary fuel ports. The amount of premixing is controlled by the momentum ratio between the fuel jets and the air cross flow. The momentum ratio depends on the lance height and the ratio between primary and secondary fuel, for a given global equivalence ratio and thermal input. The remaining fuel is provided through the secondary fuel ports and partially premixed in the conical wall jet, which is formed by the flow downstream of the narrow annular burner throat. However, secondary fuel has also the potential to

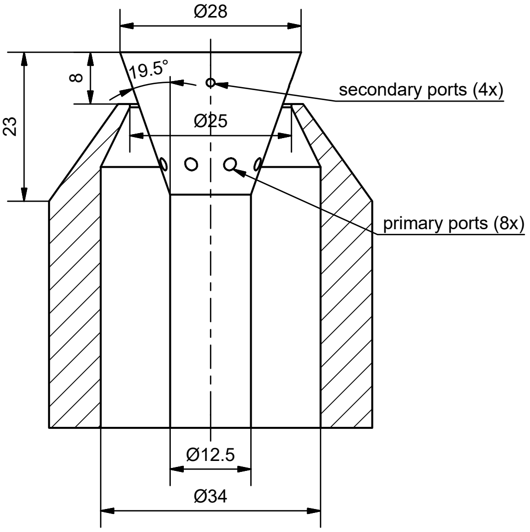

Figure 2.1: Cross sectional view of the PPBB burner (dimensions in mm). Reprinted from Meraner et al. [87].

penetrate the wall jet, depending on the momentum ratio. Primary and secondary fuel ports are controlled independently, which increases the flexibility of the burner design. At base conditions (i.e., 10 kW thermal load) for the operation with pure hydrogen, 70% of the fuel mass flow is provided through the primary fuel ports and the remaining 30% through the secondary fuel ports, based on the finding by Dutka et al. [38]. A recirculation zone is formed downstream of the bluff body, which transports hot combustion products upstream to the flame anchor point at the bluff body trailing edge and stabilizes the flame. This recirculation zone is further referred to as inner recirculation zone. A secondary, larger recirculation zone is formed in the outer region of the combustion chamber. The elevated bluff body position allows the entrainment of flue gas, which is recirculated in the outer recirculation zone, upstream of the flame anchor point and leads to a dilution of the fuel-air mixture.

As mentioned previously, the elevated and variable bluff body position is a unique feature of the PPBB burner and a crucial element for its fuel flexibility and has been studied in detail by Dutka et al. [35, 36, 38]. However, it is important to note that varying the lance/bluff body position affects several other parameters of the burner as well. Increasing the lance height, increases for instance also the burner throat opening and decreases therefore the air flow velocities for a given mass flow rate. This is an important difference to other studies of burners with elevated bluff bodies [16, 50, 105, 124]. The velocity in the fuel jets, on the other hand, is not

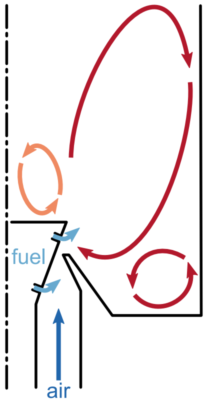

Figure 2.2: Illustration of the main flow features in the PPBB burner. Primary and secondary fuel ports are, for simplification, drawn in the same plane. Reprinted from Meraner et al. [87].

directly affected. Moving the bluff body changes, furthermore, the axial position of the fuel ports with respect to the burner throat and changes the distance between primary fuel ports and burner housing, due to the converging design of the housing. This can potentially cause an impingement of the fuel jet onto the burner housing. Since changing the lance height alters both the length of the conical wall jet as well as the characteristic velocity of it, also the entrainment and hence dilution with recirculated flue gas changes. Hence, it is ambiguous to attribute the effect of a varying lance position to any of these parameters individually. The present work investigates the impact of the lance height on the burner flow field, therefore, only under non-reacting conditions, which excludes effects linked to the fuel port position.

2.3 Hydrogen and hydrogen-rich fuels

This section follows the work by Taamallah et al. [123], but focuses more specifically on the implications of hydrogen and hydrogen-rich fuels for the investigated PPBB burner. Initially the effect of hydrogen on the thermodynamic and transport properties of a mixture are discussed. The impact of hydrogen on this microscopic level translates, furthermore, to altered flame properties which are scrutinized as well, followed by a discussion on combustion stability. The effect of hydrogen on NO_x formation is addressed in section 2.4, which furthermore gives a general overview on NO_x.

2.3.1 Thermodynamic and transport properties

Molecular and atomic hydrogen (H_2 and H) have significant higher thermal, mass and momentum diffusivities compared to other typical fuels and air. Figure 2.3 shows the thermal diffusivity of three different fuels mixed with air at various equivalence ratios, as well as the mass diffusivity of the respective fuel in the mixture. Methane (CH_4) and CO have comparable mass and thermal diffusivities. Their thermal diffusivity is, furthermore, similar to the thermal diffusivity of air. The effect of equivalence ratio variations on the thermal diffusivity of the fuel-air mixture is, therefore, negligible for these fuels and their Lewis number (i.e.,the ratio between thermal and mass diffusivity) is relatively constant close to unity. The Lewis number indicates indirectly how sensitive the combustion intensity for a given fuel is to fluid dynamic strain and flame front curvature (i.e., stretch). The thermal diffusivity of H_2, on the other hand, is approximately one order of magnitude larger than for air, which leads to a considerable variation of the thermal diffusivity for H_2-air mixtures depending on their equivalence ratio. The high thermal diffusivity of H_2-air mixtures compared to the mass diffusivity of oxygen (O_2) and nitrogen (N_2) leads, furthermore to a Lewis number larger than unity for fuel rich mixtures, while it is lower than unity for fuel lean mixtures, due to the high mass diffusivity of H_2 [13].

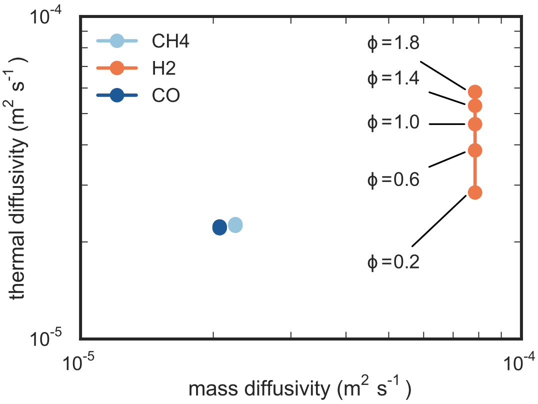

Figure 2.3: Thermal and mass diffusivity of different fuels mixed with air at various equivalence ratios, at 300 K and under atmospheric pressure. The fuels are methane (CH_4), hydrogen (H_2) and carbon monoxide (CO). The mass diffusivity is the diffusivity of the respective fuel in the mixture. The equivalence ratios for CH_4 and CO are not indicated, since the overlap with each other.

The unique properties of H_2 compared to other fuels have several implications on modelling approaches. The Lewis number for CH_4 and CO (see figure 2.3), and indeed for many species, is in the order of unity, which is frequently used as justification for models that assume a constant unity Lewis number for all species. Based on this assumption, the convective species mass fluxes cancel with the diffusive enthalpy fluxes leading to a simplified energy equation that can be written with temperature as the only dependent variable [99, 126]. However, generally this assumption is not true for hydrogen. Cuenot and Poinsot [29] investigated for example the effect of the unity Lewis number assumption on the computed adiabatic flame temperature (i.e., the maximum flame temperature that results from complete combustion without any heat losses) in diffusive flames with different Lewis numbers in the oxidizer and fuel streams. They showed that the correlation between the adiabatic flame temperature and the fuel Lewis number depends on the Lewis number in the oxidiser stream. The adiabatic flame temperature is for example a monotone function of the fuel Lewis number for oxidiser Lewis numbers above 0.6 and a non monotone function for oxidiser Lewis numbers below 0.6. This dependency is not captured by unity Lewis number models.

Another consideration that needs to be made is the description of the molecular diffusion, which is also discussed in Paper II. The simplest approach is to assume a constant diffusivity for all species and setting their diffusion coefficients equal. However, this approach is per definition not capable to account for the differential diffusion of H_2 and H. A more common strategy is to establish mixture averaged diffusion coefficients for each species. This is done by employing empirical models, such as the one proposed by Stefan [121]

$$D_{i,m} = \frac{1 - X_i}{\sum\limits_{j,j\neq i} \left(X_i/\mathcal{D}_{ij}\right)}, \tag{2.1}$$

where $D_{i,m}$ is the diffusion coefficient for species i in mixture m, X_i is the volume fraction of species i and $\mathcal{D}_{ij}$ are the binary mass diffusion coefficients, which can be obtained by employing the Chapman-Enskog theory [59], as for example shown in Paper II. Equation 2.1 is well known and has an error in order of 10% attributed to it. Full multicomponent diffusion is on the other hand, due to its complexity, less frequently employed. The full multicomponent approach requires that the computation of the diffusive flux for a species not only considers its own gradient, but all species gradients in the mixture. Because of this dependency, the diffusion coefficients in a multicomponent system D_{ij} are not a binary property and, hence, not equal to the diffusion coefficients in a binary mixture $\mathcal{D}_{ij}$.

2.3.2 Flame properties

The special chemical, thermodynamic and transport properties of H_2 affect both combustion and transport processes and lead therefore to unique flame properties for H_2 flames compared to other fuels. Figure 2.4 shows the adiabatic flame temperature for three different fuels. Both H_2 and CO are, at all equivalence ratios, characterized by higher flame temperatures compared to CH_4, with CO leading to the highest temperatures. Hence, syngas flames will generally lead to higher flame temperatures compared to natural gas. The flame temperature is an important factor for the formation of NO_x as will be discussed in chapter 2.4 and special considerations need to be made in the burner design to avoid increased NO_x due to the elevated temperatures.

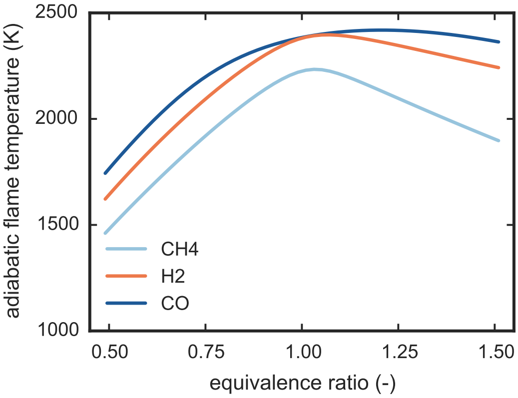

Figure 2.4: Adiabatic flame temperature of CH_4, H_2 and CO in air at atmospheric pressure, obtained with Cantera [48] using the GRI 3.0 mechanism [114].

Even though CO and H_2 have similar adiabatic flame temperatures, their laminar flame speed (i.e., the speed at which a laminar premixed flame propagates through an unburned quiescent mixture) is different. H_2 has a significantly higher laminar flame speed, which can be one order of magnitude larger than for other fuels. The high laminar flame speed of H_2 is caused by the large molecular diffusivity of H_2 and H, as well as by the higher chemical reactivity which intensifies the formation of a radical pool [106]. Hence, the laminar flame speed of syngas increases with increasing H_2 concentration.

The presence of H_2 in fuel-mixtures does not only affect the laminar flame speed, but also the sensitivity of it to stretch, which is important for the turbulent flame speed. To recap, both laminar and turbulent flame speed depend on the molecular diffusivity and the combustion kinetics. However, the turbulent flame speed is dependent on the flow conditions, while the laminar flame speed is defined independent of the flow. CH_4-H_2-air flames become diffuse-thermal unstable, when the H_2 mole fraction in the mixture exceeds 45%, while pure CH_4 flames are diffuse-thermal stable [106]. The preferential diffusion of H_2 leads to a locally increased equivalence ratio and increased consumption rate per unit area in positive curved (i.e., the centre of curvature lies in the product side) flame regions. This leads to the formation of cusps and enhanced flame surface area generation, as has been shown by direct numerical simulation (DNS) of a hydrogen enriched methane flame by Hawkes and Chen [51]. The increased flame surface area generation and burning rate per flame surface area lead to an overall increased turbulent flame speed [77].

Another important combustion property, of special relevance for H_2 combustion, is the ignition delay time, which is relevant for the control of auto-ignition. A typical definition for the ignition-delay time is the time delay between a sudden pressure increase, for example in a shock tube experiment, and the following rapid increase in hydroxyl (OH) emissions [147]. The ignition delay time of hydrogen is similar to other fuels below 1000 K, but becomes much shorter at higher temperatures [20]. This challenge becomes even greater at elevated pressure, for which also less research data exists [102]. Chiesa et al. [22] concluded therefore that H_2 cannot be safely proposed for dry low emission combustion. However, based on the available research it appears that auto-ignition in H_2 fuelled burners can be controlled, for example by enhanced rapidly mixing [75].

2.3.3 Combustion stability

The above discussed, unique flame characteristics of hydrogen and hydrogen rich flames affect the flame stability on a macro-scale level as well. Two important aspect of the flame stability are the tendency to blowout and flashback; generally both categorized as static instabilities. The lean blowout (LBO) limit, the leanest equivalence ratio at which the combustion is self-sustained, decreases generally with increasing H_2 concentration [146]. Zhang et al. [145] measured the effect of fuel composition on LBO in H_2/CO/CH_4 flames at different pressures and found that the dependency of the LBO limit on the H_2 concentration decreases with increasing pressure. Hence, the PPBB burner and other burners that operate at low pressures will exhibit a larger fuel composition dependency of the LBO limit compared to applications at elevated pressures, such as gas turbine combustors. The Damköhler number (i.e., the ratio of the characteristic flow time scale to the characteristic chemical time scale) is a well established scaling parameter for the definition of the LBO limit [54, 74]. However, preferential diffusion effects need to be considered, as suggested by Zhang et al. [145] following the work by Kido and Nakahara [63], in order to apply the Damköhler number scaling for fuel mixtures with a H_2 concentration exceeding 50%.

Flashback is a more complex phenomenon than blowout, in the sense that it can be caused by different mechanisms and depends on the location within the burner flow field. A typical area for flashbacks to occur are boundary layers, which are characterized by low velocities. The heat transfer between the fluid and the wall are important for these type of flashback, with the potential to quench the flame. Several studies have recently been conducted investigating flashbacks in boundary layers specifically for the combustion of syngas [31, 75, 76, 80]. Flashbacks that occur in the core flow are driven by high turbulent flame speeds, exceeding the bulk velocity, and can also be related to dynamic instabilities. Another flashback mechanism, special to swirl-stabilized burners is the combustion induced vortex breakdown (CIVB) [45]. It has long been known that H_2 increases the probability for flashbacks [129]. The probability increases, furthermore, with decreasing CO_2 concentration in the syngas [30]. Hence, combustion of syngas from pre-combustion CCS, with a high H_2 and low CO_2 concentration requires special consideration for burner designs. The staged (i.e., primary and secondary) fuel port design of the PPBB burner and the jet in cross flow configuration is intended to ensure rapid mixing and hence reduce the risk of autoignition. The majority of fuel is, furthermore, premixed in the converging burner section formed by the conical bluffbody and the burner housing. This ensures high bulk velocities and thin boundary layers, and hence contributes to minimize the risk for flashbacks.

Dynamic, thermo-acoustic, instabilities are highly dependent on the burner geometry and caused by the coupling of heat release and acoustic pressure fluctuations that leads to a self-sustained amplification of the fluctuations. Speth et al. [120] investigated for example dynamic instabilities in a swirl-stabilized syngas burner. Until recently, very little studies existed that investigated the effect of the H_2 concentration on thermo-acoustic instabilities, as the majority of research efforts pointed at CH_4 flames in this field. The limited existing literature indicated, that an increased H_2 concentration does not systematically lead to increased instabilities [123]. However, over the last few years several studies were conducted in this area and thermo-acoustic instabilities in syngas burners have become an important research area in the combustion community. The present work does not focus on instabilities and a further discussion of this topic is therefore not included. Work that is, due to certain similarities with the PPBB burner design, still worth mentioning are the paper by Baraiya and Chakravarthy [4] as well as the paper by Hussain et al. [56]. The latter showed reduced heat release oscillations and a reduced flame roll-up with the addition of H_2 to CH_4 and ethylene (C_2H_4) flames. The former revealed the transition from a instability at a single frequency in H_2-CH_4 flames to a bimodal instability across the investigated Reynold number range for H_2-CO flames (i.e., two different frequencies depending on the Reynolds number) .

2.4 NOx emissions

2.4.1 NO_x formation and modelling mechanisms

NO_x can be formed via different routes, which have been subject to research for the last four decades [47, 88]. We distinguish between thermal, prompt and fuel-bounded NO_x formation, as well as NO_x formation via the N_2O-intermediate and the NNH route. Hydrogen does not contain fuel-bound nitrogen. Hence, the fuel-bound NO_x route does not apply to hydrogen flames. Another route that can be discarded for hydrogen-air combustion, is the prompt mechanism, as it relays on the presence of carbon. That leaves three mechanisms applicable to hydrogen-air flames. These are the thermal NO_x [143], the N_2O-intermediate and the NNH mechanism [12].

The N_2O-intermediate route is a major contributor to NO_x formation in gas turbines, that operate at lean conditions and high pressures [28]. However, the pressure dependency of this route, due to the involved three-body reaction (equation 2.2), makes it less important for the PPBB burner that operates close to atmospheric pressure.

$$N_2 + O + M \rightleftharpoons N_2O + M. \tag{2.2}$$

The NNH mechanism equilibrates rapidly [65] and has therefore been shown to be of more importance relative to thermal NO_x for short residence times, below 1 ms [67, 68]. The NO_x formation is therefore directly proportional to the rate constant for the following reaction:

$$NNH + O \rightleftharpoons NH + NO. \tag{2.3}$$

The rate constant for reaction 2.3 is, however, subject to large uncertainties and it is expected that the NNH mechanism may be of less importance than early studies predicted [47].

Hence, thermal NO_x formation is the dominating route for the hydrogen-air combustion in the PPBB burner. The mechanism for thermal NO_x formation is well established and can be described by the Zeldovich mechanism [143], consisting of the following three elementary reactions:

$$O + N_2 \rightleftharpoons N + NO \tag{2.4}$$

$$N + O_2 \rightleftharpoons O + NO \tag{2.5}$$

$$N + OH \rightleftharpoons H + NO. \tag{2.6}$$

Reaction 2.4 is the rate limiting reaction step, with a high activation energy of 75 kcal/mol [8]. Thermal NO_x becomes, therefore, especially important at higher temperatures, exceeding 1700 K [133], as can also be seen in figure 2.5, which shows the thermal NO_x formation rate for an adiabatic hydrogen-air mixture.

The rate constant of reaction 2.4 is associated with a low uncertainty. Hence, it is generally expected that the model accuracy for thermal NO_x is determined by the accuracy of the temperature and turbulence-chemistry interaction prediction [47].

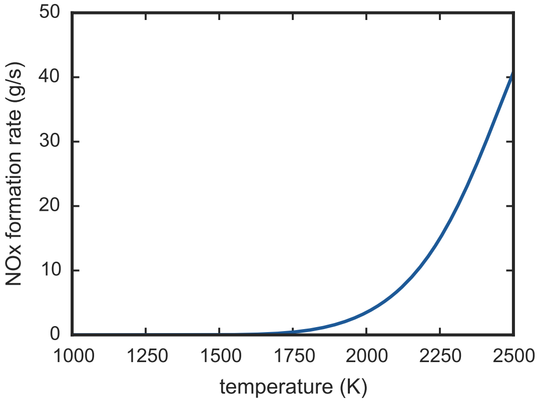

Figure 2.5: Thermal NO_x formation rate for a stoichiometric hydrogen-air mixture. Computed in Cantera [48] based on a zero dimensional, homogeneous, constant pressure reactor.

2.4.2 Effects of hydrogen on NO_x emissions

Considering the exponential temperature dependency of thermal NO_x, it is clear that any modification to a combustion process that increases the flame temperature will have a negative impact on thermal NO_x emissions. Hence, the high adiabatic flame temperature of CO and H_2 (see figure 2.4) make syngas combustion challenging in this regard.

One measure to counteract this undesired effect is to burn at leaner equivalence ratios, by exploiting the lower lean blowout limit for fuels with higher H_2 content. However, this is not always applicable. The PPBB burner is intended for the use in boilers and furnaces, which typically operate with 3% excess air. Leaner combustion is, for these applications, generally not desired due to the negative impact on the efficiency.

Another effect of increased H_2 concentrations is the lower effective Lewis number, due to the preferential diffusion of H_2 and H, which destabilizes the flame and leads to a cellular burning pattern with locally increased fuel concentrations in positive curved flame regions. Note, positive curvature refers in this context to curvatures with their centre located inside the products. The locally increased H_2 and H concentration leads to temperature peaks and, hence, to increased thermal NO_x production. [2, 10, 33, 51]

2.5 Numerical simulation of turbulent flames

2.5.1 Turbulent combustion models

The numerical simulation of turbulent flames has long been an important research topic. A discussion on the remaining challenges for the modelling of turbulent combustion is presented by Pope in [100]. The challenges he lists are the typically large number of species involved in the combustion process, the range of turbulent scales involved in it, the combination of non-linear chemical kinetics and large turbulent fluctuations, the large property variation and the coupling between reaction and molecular diffusion. For practical applications, the spectrum of turbulent scales is addressed either by Reynolds averaged Navier-Stokes (RANS) or large eddy simulation (LES). The RANS approach divides the flow field into mean values and fluctuations. For turbulent combustion this is done by employing a Favre-decomposition (i.e., a mass-weighted average). Following this approach a new set of equations is derived, which describes the mean quantities of the flow field. However, these new equations also contain terms that depend on the turbulent fluctuations which need to be modelled, the so called Reynolds stresses. Hence, RANS requires to model the full turbulent energy spectrum, since all information about the turbulent transport is contained in the Reynold stresses. LES, on the other hand calculates the effect of large scale turbulent fluctuations explicitly. However, the small scale turbulence, below a certain filter-size, still needs to be modelled, which is done by employing so called subgrid models. The smaller turbulence scales are less complex than the large scale turbulence and can, therefore, be addressed by simpler models compared to RANS. An example of such a subgrid model is the widely used model proposed by Smagorinsky [112]. Figure 2.6 illustrates how the temporal evolution of the temperature in a single point of a turbulent flame would be captured by RANS and LES models. The fundamental difference between these approaches has important implications for other submodels, as for example NO_x formation which is characterized by a non-linear temperature dependency.

The complex combustion chemistry is typically simplified by some sort of tabulation approach or reduction of the reaction mechanism [44]. A detailed reaction mechanism can be simplified by employing a quasi-steady state or partial equilibrium assumption to derive global reaction schemes. Tabulation on the other hand is based on a "complete" reaction mechanism. However, the reaction rates and species mass fractions are tabulated based on a initial computations in a "sim-

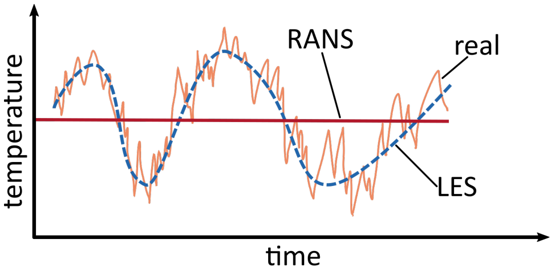

Figure 2.6: Illustration of the local temperature in a turbulent flame as captured by RANS (solid red line) and LES (dashed blue line), compared to the real (solid orange line) progression.

ple" one-dimensional flame configuration. Hence, only a few coordinates for the look-up tables, such as the mixture fraction, progress variable etc., need to be included in the CFD simulation. Many models, but not all, use either a flamelet or a probability density function (PDF) based approach to address the coupling between reaction and turbulence [99]. To be precise, the coupling between reaction and molecular diffusion, since turbulence does not directly interact with reactions, rather increases molecular diffusive fluxes by amplifying gradients. A third model category is formed by models that are based on the analysis of turbulent mixing processes, such as the eddy breakup (EBU) [116] and eddy dissipation model (EDC) [78, 79].

PDF-like models have shown the potential to accurately describe several laboratory jet flames [39, 52]. However, they are in general significantly more expensive than flamelet-like models or models base on turbulent mixing and therefore for many applications, including the present work, inaccessible. Flamelet-like models on the other hand, especially flamelet generated manifold models (FGM) [93], have become more and more popular and shown to perform very well for many different applications [130], even though they rely on strong assumptions. The basic concept of flamelet models is the idea that small elements of the turbulent flame (i.e., flamelets) are characterized by the same structure as a laminar flame and can be parametrized by a few variables such as the mixture fraction and scalar-dissipation. An important limitation for this assumption is that the reaction zone is thin and not affected by the turbulence. Hence, the applicability of these models is restricted to certain combustion regimes. The FGM approach, a flamelet-like model, does however not share this limitation. The FGM combines one-dimensional flamelets with a manifold approach, which is based on the idea that a chemical system can, independently of the initial conditions, after a relatively short time be described by only few variables (i.e., a low dimensional manifold). Figure 2.7 illustrates this concept. The illustration is for simplicity based on two species, A and B. The system converges independently of the initial composition a, b or c, towards the equilibrium e. The important factor is that the mass fraction $\mathrm{Y_A}$ and $\mathrm{Y_B}$ are from point m onwards directly linked to each other. The flame thickness in the FGM model is due to the manifold implementation generally not constant, but described by conservation equations.

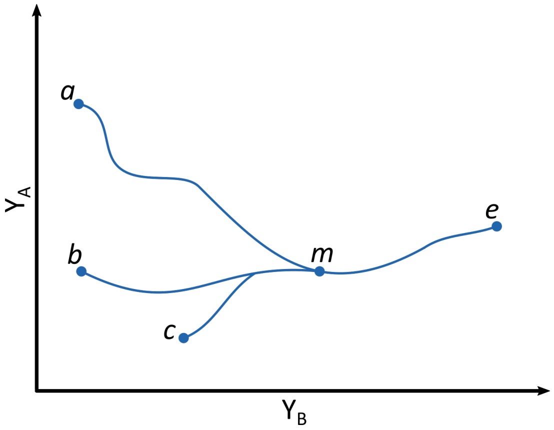

Figure 2.7: Illustration of the low dimensional manifold principle.

As already mentioned, besides flamelet-like and PDF-like models, different models based on turbulent mixing are proposed in the literature. One of the most prominent models in this category is the EDC model by Magnussen and Hjertager [78, 79]. The basic idea of this model is that all reactions occur in the so called fine-structures, where reactants are mixed at a molecular level and the turbulence energy is dissipated. On the basis of this assumption two concepts are employed; a cascade model [41, 78] for the energy transfer and a fine-structure reactor model. The fine-structures are in the same order as the Kolmogorov scales and cannot be resolved. Hence, a link between these scales and the flow field needs to be established. This is done by the cascade model, which describes the energy transfer from the largest eddies to successive smaller ones and thereby relates the fine-structure to the turbulent quantities obtained from the turbulence model. Based on the cascade model, the mass fraction of the fine-structures, γ_λ, is expressed as

$$\gamma_\lambda = C_\gamma \left(\frac{\nu\epsilon}{k^2}\right)^{1/4}, \tag{2.7}$$

where ν is the kinematic viscosity, ϵ the dissipation of turbulent kinetic energy, k. The model constant C_γ has a value of 2.1377. Furthermore, the mean residence time in the fine-structures, τ^*, is defined as

$$\tau^* = C_\tau \left(\frac{\nu}{\epsilon}\right)^{1/2}, \tag{2.8}$$

with a model constant C_τ of 0.4082. The fine-structure can be seen as a perfectly stirred reactor, which leads to the expression for the mean reaction rate, $\bar{R}_i$ for the species i

$$\bar{R}_i = \frac{\bar{\rho}\gamma_\lambda^2}{\tau^*(1-\gamma_\lambda^3)}(Y_i^* - \tilde{Y}_i), \tag{2.9}$$

where $\bar{\rho}$ denotes the density, $\tilde{Y}_i$ is the mean mass fraction of species i in the control volume and Y_i^* is the mass fraction of species i in the fine-structures. Note that some implementations, including the default implementation in ANSYS Fluent, use a plug flow reactor instead of the perfectly stirred reactor in order to simply the numerical solution process. This has, however, significant implications in flow regions with low turbulence, as discussed by Lewandowski and Ertesvåg [72]. The reactor model in ANSYS Fluent was, therefore, altered in the present work in order to reflect a perfectly stirred reactor. The mean mass fraction, $\tilde{Y}_i$, for species, i are computed from mass fraction in the fine-structures, Y_i^*, and the mass fraction in the surrounding fluid,Y_i^0,

$$\tilde{Y}_i = \gamma_\lambda^3 Y_i^* + (1-\gamma_\lambda^3)Y_i^0, \tag{2.10}$$

as proposed by Gran and Magnussen [49], while the original model used γ_λ^2 in equation 2.10, instead of γ_λ^3.

2.5.2 Modelling challenges

In the following different challenges regarding the simulation of NO_x formation in partially premixed hydrogen flames are discussed.

The treatment of molecular diffusion becomes especially important when the Schmidt number (i.e., the ratio of viscous to molecular diffusion rate) of the participating species differ from each other, and if the Lewis number can't be assumed to be unity, i.e., the thermal diffusivity is not equal to the mass diffusivity [91]. The importance of differential diffusion has been highlighted in various publications among them are [23, 71, 98, 132, 140]. An important case of differential diffusion is the preferential diffusion of H_2 and H in hydrogen combustion, as discussed in section 2.3. During the last two decades different approaches have been suggested to account for differential diffusion in flamelet-like models. The most noticeable are probably the unsteady flamelet model by Pitsch et al. [96, 97] and the FGM by van Oijen et al. [93, 130]. Oijen et al. [130] developed a FGM based on a generalized flame stretch theory, that accounts for effects of changes in pressure, enthalpy and elemental composition at the reaction layer by creating a multiple-dimensional manifold. Increasing the manifold dimension improves the accuracy of the FGM at the cost of increased memory demands for the computations.

A similar dilemma is faced whenever chemical processes are involved that span time scales that differ substantially from each other. An example of this is the formation of NO_x, which involves slow chemistry (i.e., much slower than the physical processes), while other combustion reactions are much faster than the physical processes (i.e., fast chemistry). This prohibits a successful tabulation of the NO_x mass fraction (Y_{NO_x}) based on a single combustion progress variable (Y_c), as the majority of changes in Y_{NO_x} accours for Y_c close to its equilibrium state. Zoller et al. [149] proposed to first generate a table based on the mixture fraction, scalar dissipation rate and radiation, and then to tabulate the NO source term as a function of Y_{NO} for each entry in the table. This approach, not only leads to very large tables and requires the computation of an additional transport equation for NO, but is also limited to moderate NO concentrations. Collonval [25] proposes to avoid large look up tables by algebraic modelling the evolution of the NO source term with a series of exponential functions. This approach was partially validated, but a series of limitations have been found. These include problems regarding the curve fitting of the algebraic model, the assumed shape of the model function and limitations of its applicability for partially premixed flames.

The mixing mode, in which the PPBB burner operates, represent another challenging aspect for the combustion model. Primary fuel and combustion air are only partially premixed and the mixture fraction varies along the burner circumferences. Adding secondary fuel to the system generates local fuel rich areas while still allowing the burner to be operated globally at fuel lean conditions. The PPBB burner can therefore, similar to many other practical combustion systems, not be categorized by a pure premixed or diffusive combustion regime. Research activities and model development have historically often been focused on one of theses two regimes at a time only. Although the understanding as well as modelling capability of homogeneous partially premixed flames has improved significantly over the last decade, inhomogeneous partially premixed and stratified flames, such as the PPBB burner, are still not fully explored [81, 100]. Inhomogeneous, in this context, follows the definition by Meares and Masri [81] as: "the situation where spatial gradients in mixture fraction or equivalence ratio exist so that mixtures exiting the burner may have pockets of reactive fluid adjacent to richer or leaner mixtures." While stratification refers to the existence of varying local gradients in the flammable mixture that lead to different local flame speeds.

Fiorina et al. [43] provides an overview over recent modelling approaches for stratified turbulent flames, comparing models from five different recognized research groups. All models were implemented in the context of LES, which represents the state of the art in turbulence modelling, but is still regarded as too expensive for many practical burner applications; especially at large scales. The simulation results were validated against the turbulent stratified flame configuration from the technical university of Darmstadt, analysed by Seffrin et al. [108]. A more recent stratified target flame has been developed by Meares and Masri at the university of Sydney [81] which is to date still challenging the research community. Perry et al. [94] has shown that even small inhomogeneities at the inlet of the Sydney burner lead to difficulties for classical single mixture fraction models. Both flames, from Darmstadt and from Sydney, are designed as target flames for the validation of numerical models. A more applied test-setup is for example the gas turbine model combustor investigated by [83, 136]. An interesting aspect of this burner is its rounded outer nozzle which results in a strong dependency of the flow pattern in the chamber, and hence the combustion, on the location of the flow separation point at the nozzle [107, 138]. This behaviour is not desired in a target flame for the validation of combustion models, however, it illustrates how intertwined the fluid dynamics and combustion kinetics are in practical systems, such as the PPBB burner. Numerical simulations of several other model burners at laboratory scale as well as of existing "real" engines have been reviewed by Gicquel et al. [46]. The review concluded that, despite considerable progress, LES is still not accessible for many industrial combustors, with an associated cost that is typically a 100 times larger than for RANS simulations.

In general all numerical simulations need to be set up under the premise that a compromise regarding computational cost and model accuracy needs to be made in order to achieve a balanced model configuration. The boundaries for the model costs for the present doctoral thesis, and hence model complexity, are defined by the large number of simulations, including simulations at large burner scales, that are necessary for the investigation of the burner scalability. This renders scale resolving simulations as well as PDF based combustion models impractical. Flamelet based models, on the other hand, struggle with the previously discussed challenges regarding differential diffusion effects and large time scale discrepancies, as most approaches to overcome these challenges lead to significant penalties in the computational simulations due to an increased memory demand. The usage of flamelet-like models is, depending on the specific model, often more restricted to certain combustion regimes. Simpler models, based on the analysis of turbulent mixing, are on this basis a viable option for the simulation of the PPBB burner. The EDC combustion model was therefore employed for the majority of simulations, conducted in the present doctoral thesis. The EDC model, in conjunction with a detailed combustion mechanism and transport equations for individual species, allows to consider the species specific transport properties and preferential diffusion. The model is, furthermore, well suited to be combined with a post processing approach for the computation of thermal NO_x, which utilizes the assumption that the NO_x formation can be decoupled from the combustion kinetics, to reduce computational costs. The theoretical background, which is based on the analysis turbulent mixing processes, makes the EDC independent from turbulent combustion regimes; a crucial property for the present study.

2.6 Scaling

Scaling laws and their global and local effects on complex partially premixed hydrogen burners are the central subject of the present doctoral thesis and an extensive discussion on the development of different scaling laws, their underlying assumptions and their shortcomings is given in Paper III. The present sections focuses, therefore, on presenting the fundamental concepts of scaling, approaches that have historically been pursued and their limitations, which motivated the present doctoral study. Some of the basic relations between thermal input and constant velocity or constant residence time scaling, which are necessary for the reader to understand the discussed concepts, are therefore described in the present section as well as in Paper III.

Scaling of combustion systems to various sizes, ranging from laboratory to industrial scale, both in the context of numerical simulations as well as experimental campaigns, is a crucial part in the design and optimization process of burners. The possibility to conduct simulations and experiments at smaller scales becomes, especially with increasing burner complexity, more and more important for the reduction of research and development costs.

Successful scaling, requires to preserve the burner characteristics across different scales. To achieve this, scaling laws need to be established. However, similarity theory dictates such a large number of scaling parameters, many of them mutually incompatible, that a complete scaling becomes unobtainable. The necessity for partial scaling, to relax the strict requirements from similarity theory, has therefore long been acknowledged and led to a large variety of different scaling laws [9, 117].

The first studies that investigated the scaling of NO_x emissions focused on the development of scaling laws for axisymmetric, non-premixed, turbulent, jet flames, which provide a well-defined flow field. However, early studies from Lavoie and Schlander [70], as well as Peters [95], based on an equilibrium assumption for the temperature and oxygen atom (O) concentration, failed to reproduce experimental data with acceptable accuracy. Subsequently, several scaling laws were proposed that take non-equilibrium effects, as well as effects of radiative heat losses, into account [18, 19, 62, 115]. A common finding of these studies is the improved model accuracy when an additional term $(u_0/d)^{0.5}$, reflecting the non-equilibrium conditions due to flame strain, is considered [5, 15], were u_0 is the initial jet velocity and d the nozzle diameter.

Research in this area, has historically focused on diffusion flames. The work by Røkke et al. [103] is one of the few studies that specifically deals with partially remixed jet flames. Their model has, furthermore, been evaluated by Weber [134] for the application in industrial burners. Weber concluded that the radiative heat losses in the post flame region need to be included in the scaling methodology, as well as the effect of flue gas entrainment in case of internal or external flue gas recirculation. Joo et al. [58] investigated recently the potential of artificial neural networks to establish scaling models for partially premixed flames. This novel approach, could however not reach the same accuracy as the established empirical models.

For moderate or intense low-oxygen dilution MILD combustion, good results where achieved with a simple furnace temperature and global residence time scaling [122], following the suggestions by Turns et al. [127, 128]. However, it is argued that [55] this type of scaling laws will fail for burner designs with a more defined flame-sheet and near-burner regions and, hence, larger gradients of temperature and species concentration. Hsieh et al. [55] found that the near-burner region dominates the NO_x formation at larger burner scales, of 12 MW and beyond. However, at smaller scales, around 30 kW, also the contribution of the flame-sheet region needs to be considered, while the furnace region can be neglected.

Most scaling laws are, as previously mentioned, developed based on "simple" jet flames. Their applicability to complex burner designs is therefore limited and typically only two scaling laws are considered for industrial applications [55, 134]. These are constant velocity and constant residence time scaling. Both scaling laws are derived based on the basic global equation for the thermal input:

$$Q = K\rho_0 U_0 D_0^2, \tag{2.11}$$

where K is a proportionality constant, ρ_0 the inlet fluid density, D_0 the characteristic burner length scale and U_0 the characteristic burner velocity. Keeping the characteristic burner velocity in equation 2.11 constant leads to:

$$D_0 \propto Q^{1/2}, \tag{2.12}$$

and further to the relation for the scaled burner diameter, $D^*_{0,v}$:

$$\frac{D^*_{0,v}}{D_0} \propto \left(\frac{Q^*_v}{Q}\right)^{1/2}, \tag{2.13}$$

where the star superscript indicates scaled properties and the v subscript stands for constant velocity scaling. Keeping the ratio between the characteristic burner diameter and velocity, D_0/U_0, in equation 2.11 on the other hand leads to the relations for constant residence time scaling:

$$D_0 \propto Q^{1/3}, \tag{2.14}$$

and

$$\frac{D^*_{0,rt}}{D_0} \propto \left(\frac{Q^*_{rt}}{Q}\right)^{1/3}, \tag{2.15}$$

where the rt subscript indicates constant residence time scaling. Equation 2.13 and 2.15 require geometrical similarity and are based on the assumption of momentum controlled turbulent flow, which allows neglecting of Reynolds and Froude number effects.

Constant residence time scaling preserves the convective time scale, which equals the residence time in simple flames. The macro-mixing characteristics are, therefore, in theory maintained [104, 134]. However, constant residence time scaling leads, with increasing burner scales, to an increasing flow velocity proportional to $Q^{1/3}$, which leads, hence, to excessive pressure drops. Constant velocity scaling is therefore generally preferred for industrial applications, even though it does, per definition, not preserve the macro-mixing characteristics. A comprehensive data set for constant velocity scaling was obtained by the SCALING 400 project [135], a cooperated research effort by the International Flame Research Foundation and the Gas Research Institute, which investigated the NO_x emissions of swirl burners in the range of 30 kW to 12 MW, experimentally. The study has later been extended numerically by Bollettini et al. [11] to include constant residence time scaling.

It is worth mentioning that similar scaling laws have been proposed, such as the scaling law by Ballester et al. [3] which lies in-between constant velocity and constant residence time scaling, with an exponent for the scaling law $D \propto Q^x$ in the range of $x = 1/2.3 - 1/2.6$, or the scaling law proposed by Cole et al.[24], which scales the burner diameter proportional to $Q^{1/4}$ and the burner velocity proportional to $Q^{1/2}$. These scaling laws are further discussed in paper III, however, they are not as frequently applied as constant velocity or residence time scaling.

It can be argued that a single length and velocity scale, which form the basis for constant residence time and constant velocity scaling, are not sufficient to represent a complex burner. Hence, the advantage of constant residence time scaling, in preserving the macro-mixing time scale is negated in this case, as several characteristic local macro-mixing time scales exist. Indeed some studies, such as Bollettini et al. [11] and Smart and Van Kamp [113] found none of the two scaling laws to be superior over the other when applied to typical pulverised coal burners, while Megalos et al. [82] found constant velocity scaling to be more suitable.

Hsieh et al. [55], as well as Cheng et al. [21] argue that successful scaling requires to apply different scaling laws depending on local burner regions. The concept, that global scaling laws will have different effects based on the local conditions in complex burner designs forms the bases of the present doctoral thesis and is finally scrutinized in Paper III.

Chapter 3

Computational tools and modelling techniques

This chapter presents the numerical model that was developed during the course of this doctoral thesis. The main focus lies on the CFD model, developed in the ANSYS Academic Fluent framework. Discussions of the model that did not find space in the presented publications are given more emphasis here, while aspects that are already well described in the respective papers are summarized briefly. The majority of the model development and validation was conducted in Paper I and II, with minor changes in Paper III.

3.1 Grid and fluid domain

The generation of a numerical mesh, that describes the three-dimensional fluid domain with a finite number of control volumes, is a crucial step in any mesh based CFD analysis. The mesh defines which model resolution can be expected and has a strong impact on the convergence properties and numerical costs of the CFD model. Furthermore, the mesh requirements vary depending on the overall modelling approach (e.g., RANS versus LES) and other employed submodels (e.g. resolved boundary layers versus wall functions). It is, therefore, not unusual that the meshing process constitutes a large part of a CFD based study. Several different meshing strategies, i.e. hexahedral (hex), tetrahedral (tetra), polyhedral (poly), cut-cell and tetrahedral/hexahedral hybrid mesh, were considered for the simulation of the complex PPBB burner (see figure 3.1). A short discussion on their advantages and disadvantages can be found in Paper I.

Structured hex meshes limit generally the mesh induced diffusivity, given that the

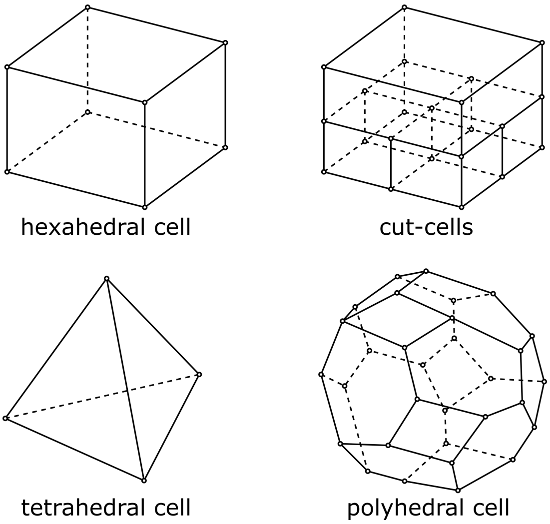

Figure 3.1: Illustration of different cell types.

flow is aligned with the mesh, require less memory and improve the model convergence compared to unstructured meshes. Hence, they are typically the first choice. However, for complex geometries, such as the PPBB burner with its several fuel ports, it can be challenging to generate a structured hex mesh. Hex meshes can, furthermore, lead to large aspect ratios if the the difference between the smallest resolved length scale and the domain size is big. The cut-cell topology addresses the issue of large aspect ratios, by allowing hanging nodes. However, they require a layer of unstructured mesh cells close to the geometry. The wall adjacent cells can, depending on the geometry complexity, be characterized by very high skewness. Preliminary simulations of the PPBB burner with a cut-cell type mesh showed that these few "bad" cells, especially close to the lateral walls of the conical buff body, severely harmed the model accuracy and convergence. An alternative approach is to generate unstructured meshes, often consisting of tetrahedral or polyhedral cells. These meshes can be generated automatically, with more or less user control on the size and quality distribution, and are therefore especially well suited for the simulation of complex geometries. Both tet and poly meshes can easily adapt to complex geometry. However, tet meshes require a much larger cell count compared to poly mashes, at a comparable accuracy. The polyhedral grid topology was, therefore, chosen for the simulation of the PPBB burner.

Reducing the model complexity, by initially focusing on the non-reacting flow in the burner, allowed the exploration of different modelling approaches, including models that are too expensive for the simulation of reacting flows in an up-scaled burner. The requirements for the numerical mesh were therefore different in Paper I compared to Paper II and III. All simulations presented in Paper I resolved the boundary layers by using multiple inflation layers (i.e., prism cells adjacent to walls) to maintain a dimensionless wall distance (y^+) close to unity. The simulations in Paper II and III, on the other hand, utilized a single inflation layer in conjunction with wall functions to minimize numerical costs.

Paper I investigated the burner in an unconfined configuration, which requires a larger fluid domain compared to the combustion chamber investigated in the other papers. The fluid domain in Paper I extends 20 bluff body diameters downstream of the burner and has a width of 10 bluff body diameters. In Paper I a total of 5.2 M cells were used to simulate the 8 mm lance height configuration and 4.0 M cells to simulate the 16 mm configuration. The simulations in Paper II and III were conducted on a 3.5 M cell mesh.

All steady state simulations were conducted on a quarter domain, utilizing periodic boundary conditions, while all transient simulations were conducted on the full domain (i.e., four times the cell count) to allow for turbulence development close to the burner axis (see figure 3.2).

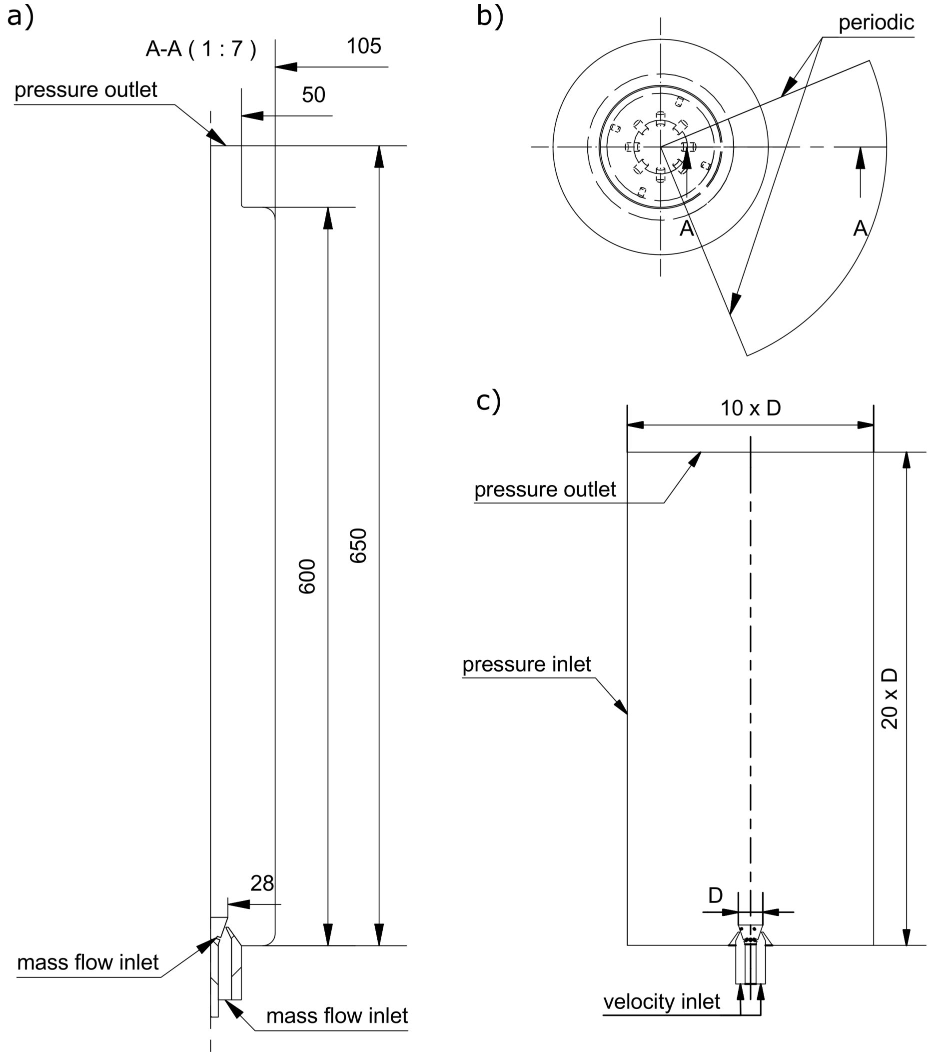

Figure 3.2: Illustration of the computational domain including boundary types. All unspecified boundaries are walls. a) side view and b) top view of the quarter domain with combustion chamber, used in Paper II and III. c) side view of the full, unconfined domain, used for the transient simulations in Paper I. Note the drawings are not to scale.

3.2 Numerics

All conducted simulations were based on the finite volume method, discretising the governing equations for the conservation of mass, momentum, energy, turbulence and species with a second order upwind scheme. A point implicit (Gauss-Seidel) solver in conjunction with an algebraic multigrid method was employed to solve the equation system. The density was computed based on the incompressible ideal gas law and a cell-based least-square method was used to calculate gradients and derivatives on the highly unstructured poly mesh. A second order central difference scheme was applied for the pressure recovery at cell faces, necessary due to the co-located scheme employed in ANSYS Academic Fluent. The pressure-velocity coupling was realized with the semi-implicit method for pressure linked equations-consistent (SIMPLEC) algorithm in Paper I, and changed to the pressure-implicit with splitting of operators (PISO) algorithm with skewness correction in Paper II and III, aiming to improve the model stability.

The most significant differences between the numerical setups in the presented papers are related to the scale resolving simulations, conducted in Paper I. The convective terms in the RANS transport equations were discretised with a second order upwind scheme. However, upwind schemes are too numerical dissipative for scale resolving simulations. A bounded central difference scheme was therefore used for all LES and stress-blended eddy (SBES) simulations. Furthermore, it is not possible to apply the steady state assumption to scale resolving simulations. The non-iterative time advancement (NITA) algorithm was therefore with all transient simulations, which furthermore allowed the usage of the fractional-step method (FSM), a slightly less computationally expensive method compared to PISO.

3.3 Submodels

Table 3.1 provides an overview of the submodels, that were used in the simulations for the scaling of the PPBB burner and hence represent the most comprehensive CFD model of the PPBB burner. During the model development special attention was given to the turbulence model, boundary layer treatment, combustion kinetics, and turbulence-chemistry interaction.

A variety of different turbulence models were investigated in Paper I, including unsteady Reynolds averaged Navier-Stokes (URANS) and scale resolving simulations employing the WALE subgrid model in a LES framework, as well as the novel SBES turbulence model that allows the application of LES models in the free flow (i.e., flow outside of wall boundary layers), while still treating boundary layers by means of RANS models. The investigated RANS and LES turbulence models are well documented in the literature [69, 84, 90, 111]. The SBES model [85, 86], however, has only recently been made available and is therefore described in more detail in Paper I.

Another modelling aspect that has been addressed by different approaches is the boundary layer treatment. Resolving boundary layer flows requires not only a fine

Table 3.1: Summary of the employed submodels.

Phenomenon	Model
Turbulence	realizable k-ϵ [111]
Wall treatment	non-equilibrium wall function [64]
Turbulence-chemistry interaction	eddy dissipation concept [78, 79]
Combustion kinetics	Li et al. [73]
NO_x kinetics	extended Zeldovich [143]
Radiation	discrete ordinates
Absorption	weighted sum of grey gases
Viscosity and thermal conductivity	kinetic theory
Diffusive flux	dilute approximation
Binary mass diffusion coefficients	modified Chapman-Enskog [59]

enough grid resolution close to walls, as described in section 3.1, but also a turbulence model that is valid throughout the whole boundary layer. The enhanced wall treatment was therefore employed in Paper I. This model has the advantage of behaving like a standard two-layer model for sufficiently fine grid resolutions, while not significantly deteriorating in accuracy on coarser wall meshes, by incorporating an enhanced wall function as fallback [1]. The enhanced wall function implementation in ANSYS Fluent can, hence, be seen as a hybrid model. The near wall grid resolution for all simulations in Paper I fulfilled the grid requirement for the two-layer approach, i.e. $y^+ \approx 1$. The two-layer approach obtains the turbulent dissipation rate, ϵ, in the viscous sublayer based on:

$$\epsilon = \frac{k^{3/2}}{l_\epsilon}, \tag{3.1}$$

and the turbulent viscosity, μ_t, based on [139]

$$\mu_t = \rho C_\mu l_\mu \sqrt{k}. \tag{3.2}$$

The length scales l_ϵ and l_μ are computed following Chen and Patel [17]. A blending function, proposed by Jongen [57], is applied to ensure a smooth transition between ϵ and μ_t in the viscous sublayer and the high-Reynolds number region.

Paper II extended the CFD model for the simulation of reacting flows, which increases the model complexity and costs significantly. The objective of Paper II was, furthermore, to develop a model that is appropriate for the simulation of the burner at multiple scales. The modelling approach for the boundary layer treatment was, therefore, changed to a less expensive wall function approach. An initial attempt, using standard wall functions, failed to reproduce the flow conditions in the combustion chamber. As a consequence the nonequilibrium wall function was employed for all further simulations [64]. The key features of the nonequilibrium wall function are the sensitivity of the log-law for the mean velocity to pressure gradients and the calculation of a turbulence kinetic energy budget at the wall adjacent cells, which partly accounts for non-equilibrium effects.

An important aspect of combustion simulations are the appropriate description of the combustion kinetics. Two different reaction mechanisms were investigated for the simulation of the hydrogen combustion in the PPBB burner, one mechanism was developed by Li et al. [73], the other by Conaire et al. [92]. Both mechanisms are based on 19 reversible elementary reactions and were implemented for the 9 species modelled in the PPBB burner simulations. Both mechanisms led to very similar results. All simulations, presented in this doctoral thesis, were therefore performed utilizing the mechanism by Li et al. [73].

Three different approaches for the modelling of the turbulence-chemistry interaction have been investigated. These were the eddy dissipation concept (EDC), a premixed flamelet generated manifold (FGM) and a diffusion FGM model. For the majority of simulations, including all simulations published in paper II and III, the EDC was employed, due to its advantages regarding computational costs, as discussed in section 2.5.

Chapter 4

Summary of publications

This chapter presents a summary of the three paper that form the basis of this doctoral thesis. The employed numerical model was with each paper successively extended and improved. Links between the papers are highlighted.

4.1 Paper I - Cold flow characteristics of a novel bluff body hydrogen burner

This paper represents the first step in the model development towards the full simulation of the PPBB burner, including chemical reactions, species transport, radiation, etc. and focuses on the simulation of the non-reacting flow field. The paper provides, furthermore, an extensive introduction to the unique burner design and utilizes the new model to study flow features of the burner that where not accessible to the previous performed experimental studies.

A computational fluid dynamic (CFD) model of the PPBB burner was developed utilizing the commercial multi-physics software ANSYS Academic Fluent, Release 18.1. High priority was given to the selection of an appropriate turbulence model, which not only dominates the description of the non-reacting flow field, but also builds the foundation for the simulation of species transport, turbulence-chemistry interaction and other submodels for following studies of the reacting flow. A set of steady-state and unsteady Reynolds averaged (RANS) simulations for the burner operating with a lance height of 8 mm was conducted. Three different turbulence models were employed for these simulations; namely the standard k-ϵ, realizable k-ϵ, shear stress transport (SST) k-ω. The simulations were validated against PIV measurements from Dutka et al. [38]. All models were capable to reproduce the extend of the recirculation zone, but over predicted the velocity magnitude, both in the recirculation zone as well as in the wake flow. The SST k-ω showed the largest deviation between experiments and simulations, while both the standard as well as the realizable k-ϵ model were able to predict the peak velocity in the wake flow reasonable well. All models showed an improvement when employing an URANS (i.e., unsteady RANS) approach. The URANS SST k-ω model was the only model capable to reproduce the velocity decay along the burner axis. It was concluded that the over predicted velocities downstream of the bluff body, are a consequence of the poor model performance in the wall jet and shear layer region close to the bluff body.

On this basis, scale resolving simulations with two different models, the novel stress-blended eddy simulation (SBES) and the WALE subgrid model in a large eddy simulation (LES) framework, where conducted for a lance height of 8 mm and 16 mm. The performance of both models was nearly identical, leading to good results for the 8 mm lance height case and very good results for the 16 mm lance height case. Based on these simulations, it was found that the recirculation zone length scales proportional to the lance height while the recirculation zone width is not affected by changes of the lance height. The recirculated mass flow rate decreases, furthermore, with increasing lance height.

Finally, the paper presents a detailed analysis of the near wall region close to the lateral walls of the bluff body. This region is characterized by a conical wall jet flow, a configuration which is rarely investigated, and was not accessible to the PIV measurements. For 8 mm lance height, a self similar velocity profile was observed at a normalized distance of 3.1 throat heights downstream of the throat opening which is in agreement with findings by other researchers [66, 109, 110]. The velocity profiles in the wall jet of the 16 mm case did not collapse as the normalized distance between throat opening and bluff body trailing edge is shorter.

4.2 Paper II - Combustion and NO_x Emission Characteristics of a Bluff Body Hydrogen Burner

This paper contains the extension of the CFD model, developed in Paper II, to incorporate species transport, combustion kinetics, turbulence-chemistry interaction, NO_x kinetics, thermal radiation and the confinement of a combustion chamber. The model is validated against experimental data for a wide range of operational conditions, and the effect of secondary fuel fraction and thermal input on the burner performance is explored.

In total twelve CFD simulations where conducted with the secondary fuel fraction ranging from 0% to 30% and the thermal input ranging from 10 kW to 25 kW. Overall a good agreement between predicted and measured NO_x emissions was achieved, with an average deviation of 7%. The dependency of NO_x emissions on the thermal input was captured well. The model was, however, not able to reproduce the emission dependency on the secondary fuel fraction at a thermal load of 10 kW.

The paper presents, furthermore, a novel combustion regime diagram, utilizing the detailed data obtained by CFD simulations. The proposed approach considers local variation of turbulence and combustion conditions; an important aspect of complex partially premixed burners. Employing such CFD based regime diagrams allows furthermore the visualization of an additional coordinate, such as the local equivalence ratio distribution. The analysis of the PPBB burner simulation at base case conditions, 10 kW thermal input and 30% secondary fuel, revealed two distinct regions for primary and secondary fuel in the regime diagram. Both are, to a large extent, located at Damköhler numbers exceeding unity for combustion close to the global and stoichiometric equivalence ratio. Especially primary fuel shows, however, a wide spread in the regime diagram, burning in a multi-regime mode, where lean mixtures are combusted at higher Karlovitz numbers.

The analysis of the mixture fraction distribution under different operational conditions revealed that the inner recirculation zone is characterized by a fuel rich mixture at base conditions. The conditions in the recirculation zone change, however, to a fuel lean mixture when all fuel is provided through the primary fuel ports, i.e. no secondary fuel. Adding secondary fuel decreases the recirculated mass flow rate in the inner recirculation zone, while it has only a negligible effect on the mass flow rate in the outer recirculation zone. Increasing the thermal input, on the other hand, affects both recirculation zones, leading to an increased mass flow rate in the outer and a decreased mass flow rate in the inner recirculation zone. The impact of the changed mass flow rates on the NO_x formation rate, due to an increased thermal input, was not quantified. However, a similar dependency of NO_x emission and mass flow rates in the internal recirculation zone were observed. The inner recirculation zone is an important contributor to the overall NO_x emissions. The highest NO_x formation rate is observed in the concave region of the stoichiometric mixture iso-surface. The stoichiometric fuel-air mixture is in this regions mixed with hot products from the inner recirculation zone, which leads to an elevated temperature and radical concentration; consequently local peaks in NO_x formation rates.

4.3 Paper III - Effects of scaling laws on the combustion and NO_x characteristics of hydrogen burners

The paper presents the scaling of the PPBB burner up to 500 kW based on two different scaling laws; namely constant velocity and constant residence time scaling. The CFD model, developed in Paper I and II, was employed to conduct in total 11 simulations at different burner scales. Only minor changes to the thermal wall boundaries have been made to prevent unrealistic boundary layer flashbacks at larger burner scales.

The effect of the two applied scaling laws on the Damköhler and Karlovitz number was scrutinized theoretically. Their local effect was furthermore investigated by means of the CFD based combustion regime diagrams, developed in Paper II, which were extended to incorporate hexagonal binning. The trends, predicted by the numerical simulations, agree well with the scaling theory for constant velocity scaling. The flame, which is originally to a large degree located in the thin reaction zone regime, displays increasing Damköhler numbers with increasing burner scales, and crosses the unity Karlovitz number iso-line at the 50 kW scale, into the corrugated flamelets regime. The motivation for constant residence time scaling is the theoretical preservation of the Damköhler number, which was, in the CFD simulations, confirmed for the global Damköhler number. However, the simulations showed that a significant part of the flame, mainly at the global equivalence ratio close to stoichiometry, is following a constant Karlovitz number instead. Both scaling laws led, at the 250 kW scale, to the collapse of the two distinct regions for primary and secondary fuel in the regime diagram, which were first observed in Paper II.

An apparent difference between the two scaling approaches was observed in between primary and secondary fuel ports. Constant velocity scaling leads in these regions to a significant local increase of the progress variable source term, at an equivalence ratio around 0.7. Constant velocity scaling leads, furthermore, to an overall larger variance in the equivalence ratio with more fuel burning at lean and rich conditions further away from stoichiometry, compared to constant residence time scaling.

Constant velocity scaling and constant residence time scaling lead at a macro scale to a fundamentally different shape of the stoichiometric equivalence ratio iso-surface. Constant velocity scaling causes the original four tips to collapse to a single one, while constant residence time scaling preserves them. However, constant residence time scaling leads to a transition from the fuel rich inner recirculation zone to a fuel lean recirculation zone. The inner recirculation zone is an important contributor to local NO_x formation peaks, due to the hot recirculated products that are mixed with an unburned, stoichiometric air-fuel mixture.

Both scaling laws lead to an increase of the global NO_x emissions and are not reaching a plateau within the investigated range. This may indicate that the investigated laboratory scale burner is too small to make realistic predictions for the full scale burner. However, it is still possible to utilize the burner as a case study to investigate the effects that constant velocity and constant residence time scaling has on the combustion and NO_x characteristics of the PPBB burner. The fluid domain was decomposed into the six following regions, in order to differentiate between local effects: walljet (WJ), flame (FL), inner recirculation zone (IRZ), outer recirculation zone (ORZ), immediate post flame (IPF) and post flame (PF). The immediate post flame, flame and inner recirculation zone regions were identified as the three main contributors to the overall NO_x emissions. Constant residence time scaling leads in all three regions to higher mean volumetric NO_x formation rates. However, the overall NO_x formation is for constant velocity scaling larger in the intermediate post flame and flame region, which is attributed to the larger volumes and longer residence times. The overall NO_x formation rate in the inner recirculation zone, on the other hand, remains close to constant for constant velocity scaling, while an increase is seen for constant residence time scaling. The mean volumetric NO_x formation rate in the inner recirculation zone is driven by the local oxygen atom (O) and OH concentrations, which is dependent on the flow conditions and entrainment into the inner recirculation zone.

This paper, furthermore, revealed a sudden break up of the inner recirculation zone in the narrow band between 450 kW and 500 kW, when constant velocity scaling is employed. The break up of the inner recirculation zone leads to the formation of a vortex pair in the outer chamber region and an outwards bending of the flame, which ultimately leads to a flame impingement onto the combustion chamber. The recirculation zone break up was attributed to the different scaling effect of constant velocity and constant residence time scaling on the momentum and length scale ratio of the annular jet and bluff body flow.

Chapter 5

Additional work

This chapter presents work that has been initiated during the present Ph.D. project, but has not yet reached a level that qualifies for publication in a scientific journal. However, a valuable foundation was created for future work on scale resolving simulations of the PPBB burner and a framework for a reactor network model of the burner was implemented. A short summary of these activities is, therefore, provided here, promoting future work and making existing achievements accessible.

The numerical model, which forms the basis for the majority of the present doctoral thesis, has been developed with focus on a good balance between model cost and accuracy; an important requirement for scaling of burners to different sizes. The following two approaches represent, in contrary, two extreme cases. First scale resolving simulations are presented, which generally provide a considerable increased model accuracy, however, comprise significantly larger computational costs. Following the scale resolving simulations, a reactor network is outlined. This simplified model is based on a variety of assumptions and aims to reproduce only few of the important burner characteristics.

5.1 Scale resolving simulations

Parts of the scale resolving simulations described in this section were presented in the form of a work in progress poster at the 37th international symposium on combustion in Dublin. The simulations were conducted employing an LES approach with the WALE subgrid model. In order to reduce the numerical costs only the fluid domain downstream of the burner throat was modelled. The inlet conditions at the throat were obtained by a preceding steady state RANS simulation. The grid for the LES simulations consists of 4.6 M polyhedral cells.

A major difference to the RANS model of the PPBB burner is, besides the turbulence model itself, the approach utilized to describe the hydrogen combustion. The LES simulations were conducted employing a FGM, parametrizing all species and temperature by the mixture fraction, progress variable, and enthalpy. The consideration of enthalpy is important in order to account for non-adiabatic effects, such as the heat exchange with the combustion chamber wall. The FGM was chosen over laminar flamelet models, as it is not based on the assumption of an intact thin flamelet, and hence, can theoretically be applied to a wider range of combustion regimes, as well as for the simulation of flame quenching and extinction. The reaction mechanism by Li et al. [73] containing 9 species and 19 reversible elementary reactions, which is the same as used for the RANS simulations, was employed to compute the FGM. The closure model by Zimot et al. [148], with a turbulent flame speed constant of 0.61, which is recommended for hydrogen combustion, was used for the turbulent flame speed calculation.

The mean source term is computed based on a presumed joint beta PDF and a flamelet library. Hence, an important factor for the performance of the FGM are the flamelet calculations that form the basis for the library generation. This is challenging for partially premixed flames, which cannot be entirely described by either premixed or diffusive flamelets. Different hybrid models, such as the model by Yadav et al. [141] have therefore been proposed, which generate both a premixed and a diffusive manifold, in order to calculate the mean source term based on a weighted average of those two. Challenging aspects of such an approach are the increased memory demand and the determination of a suitable blending function between the premixed and diffusive manifold. A more pragmatic approach is to base the FGM on only one flamelet type. The accuracy of such a model will, consequently, be higher for flames that behave similar to one of the extreme cases, i.e., either a fully premixed or a completely diffusive flame. It is therefore important to identify the predominant mixing mode, in order to choose the flamelet approach that resembles the flame the closest. Yamashita et al. [142] proposed a flame index, G_{FO}:

$$G_{FO} = \nabla Y_{H_2} \cdot \nabla Y_{O_2}, \tag{5.1}$$

to distinguish between premixed and diffusive flames. In the present work, three different flamelet approaches were investigated, a unstrained premixed, a strained premixed and a diffusive flamelet. Figure 5.1 shows the finite rate source as a function of the local equivalence ratio, for the simulation based on a strained premixed flamelet. The data points are coloured by the flame index, following equation 5.1, with positive values representing premixed and negative values representing diffusive flames. The premixed and diffusive data points are shown in the upper and lower subplots respectively, to increase the readability. The subplots on the left-hand side (i.e., a and c) show data obtained on a cut-plane crossing two primary fuel ports, while the subplots on the right-hand side (i.e., b and d) show data obtained on a cut-plane crossing two secondary fuel ports.

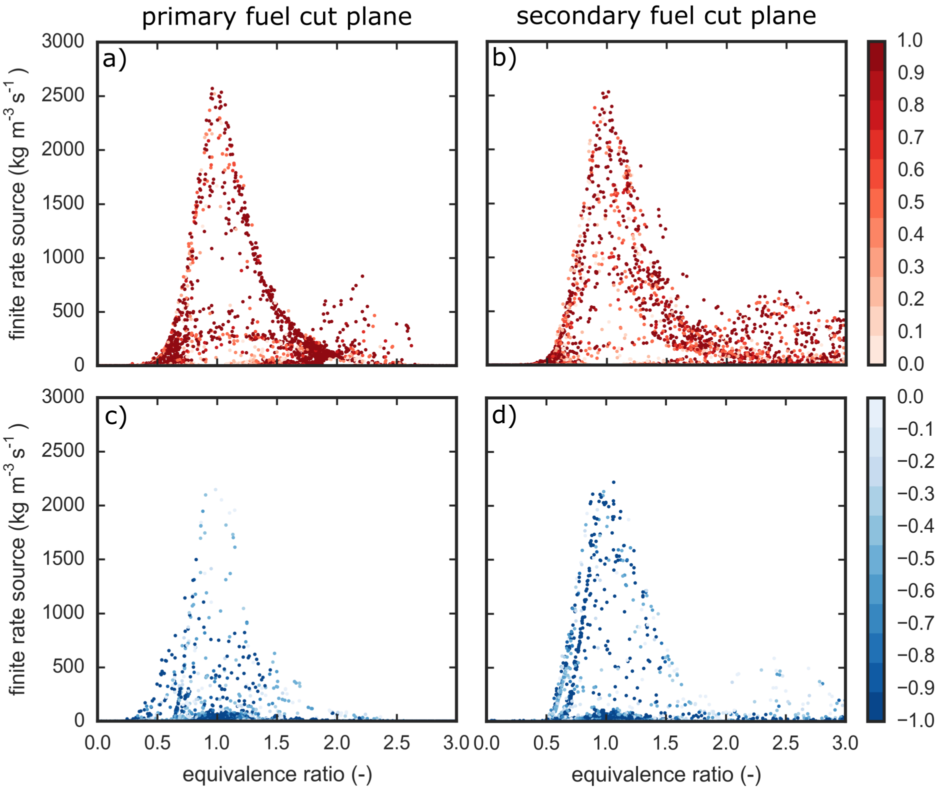

Figure 5.1: Finite rate source versus local the equivalence ratio, colour-coded by the flame index for premixed (red) and diffusive (blue) combustion in the primary fuel cut plane (a) and (c), as well as in the secondary fuel cut plane (b) and (d). Note, values that are exactly zero are duplicated in the plots.

The highest reaction rate is observed around stoichiometry. However, premixed data points are more frequently clustered at lean and rich equivalence ratios. Both scatter plots, showing premixed combustion, share a data point cluster in the equivalence ratio range of 0.6–0.7, which is leaner than the global equivalence ratio of 0.87. In the primary fuel cut plane another cluster is observed at rich equivalence ratios around a value of 1.5. The secondary fuel cut plane shows, on the other hand, a much wider spread for rich equivalence ratios, although generally at low reaction rates below 500 kg $m^{-3}s^{-1}$. Both cut planes show a contribution from diffusive combustion, however, the reaction in this mode is stronger for the secondary fuel cut plane. Note, the secondary fuel ports are located further downstream and, hence, closer to the flame anchor point, compared to the primary fuel ports, which reduces the time available for premixing air and fuel. A third cut plane, which is not shown here, in-between primary fuel ports, where no secondary fuel is located, was analysed as well. The combustion in that region is almost entirely dominated by a diffusive flame, which shows that the fuel is not fully premixed in tangential direction.

Figure 5.2 shows the a scatter plot in the temperature equivalence ratio space, coloured by the normalized progress variable. The scatter plot obtained from the primary fuel cut plane, shown in figure 5.2a, is characterized by a steep temperature drop at an equivalence ratio of approximately 2.0. The scatter plot obtained from the secondary fuel cut plane on the other hand, shows elevated also for richer mixtures, which exceed an equivalence ratio of 2.0. The flat temperature distribution at equivalence ratios between 0 and 0.5 corresponds to fluid close to the chamber wall, while the prominent temperature drop at a equivalence ratio of 1.5 is associated to the boundary layer on the trailing face of the bluff body. This indicates also that the inner recirculation zone is characterized by a rich mixture with an equivalence ratio of 1.5.

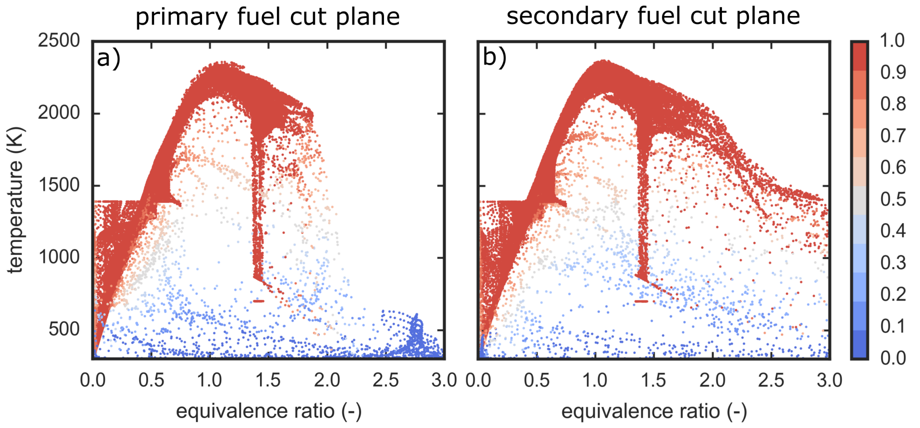

Figure 5.2: Temperature versus the local equivalence ratio colour-coded by the normalized progress variable.

The rich inner recirculation zone can also be seen in figure 5.3, which shows the mixture fraction distribution in the secondary fuel cut plane. The stoichiometric iso-line is located at the transition from blue to red contours. The overlaid greyscale iso-contours show the NO_x formation rate, which is largest for stoichiometric mixtures in the immediate post flame region, downstream of the inner recirculation zone. Note the NO_x formation rate is currently calculated based on the same post processing approach as utilized in the RANS simulations. This approach leads to an over prediction of the NO_x formation rate, when combined with LES simulations, since the model is based on mean values for species and temperature. Hence, resolved turbulent fluctuations are in addition modelled by the NO_x model. This issue still needs to be addressed and the model needs to be validated against experimental data. The initial results indicate that large parts of the flame burn in a premixed mode, however, the effect of the flamelet library approach on the NO_x emissions, the parameter of interest, has not been investigated yet.

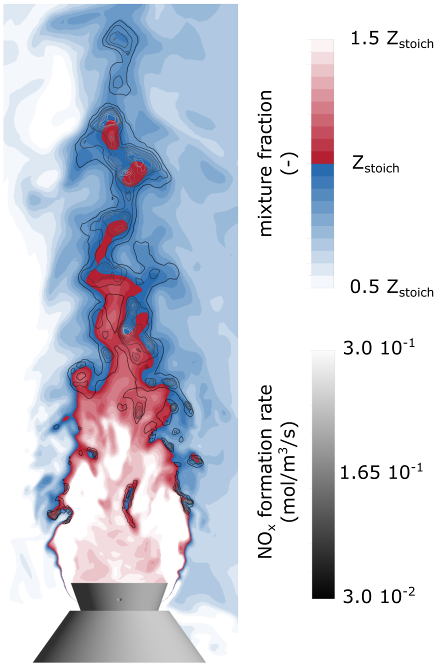

Figure 5.3: Instantaneous mixture fraction contours, overlaid by iso-lines of the instantaneous NO_x formation rate in grey scales, with red colour showing fuel rich regions and blue colour showing fuel lean regions.

5.2 Reactor network

A reactor network model of the PPBB burner, based on the open-source software Cantera [48] is presented. The reactor network consist of a set of zero-dimensional perfect stirred rectors (PSR), connected with each other in a predefined pattern. The governing equations for each reactor, i.e. conservation of mass, species and energy, are solved employing the SUNDIALS solver suite [53]. The model implementation is transient and is being advanced until steady state conditions are reached. The reader is referred to Kee et al. [61] for the detailed description of the governing equations.

PSRs are a good representation for the conditions in the inner and outer recirculation zones of the PPBB burner, however, in order to represent the other flow regions also plug flow reactors (PFR) are required. This is achieved by adding several PSRs in series, where the first and last PSR are used to connect the PFR to other reactors.

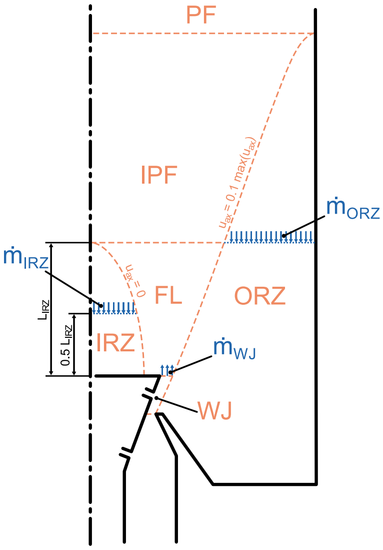

Figure 5.4: Illustration of the burner region and mass flow definitions. Note the drawing is not to scale and the fuel ports are, for illustration purpose, drawn in the same plane.

The reactor network does not solve the turbulent flow field itself. Hence, the main task for the network development is the definition of the reactor volumes, connections and mass flow controls (MFC), that regulate the mass and heat exchange between reactors, such that in practice a "frozen" flow field is resembled by the network. One approach to achieve this is to conduct CFD simulations with a fast chemistry solver and extract a detailed reactor network from the converged solution [42]. However, the objective of the present work is to develop a "simple" network that reflects the main flow features, such as the inner and outer recirculation zones, but remains small enough, so that empirical or phenomenological models can be employed to scale the network. One of the main motivations for the development of such a "simple" model is the ability to evaluate scaling laws at low costs, before validating them via CFD simulations and/or experiments. The nature of rector networks is, furthermore, of special interest for the evaluation of zone based scaling laws, such as the approaches suggested by Hsieh et al. [55] and Cheng et al. [21].

The flow domain of the PPBB burner has, on this basis, been divided into six regions. The regions are based on the CFD simulations performed in Paper III. An illustration of them is provided in figure 5.4. The region upstream of the burner throat is not modelled by the reactor network. The CFD simulations were furthermore used to establish the recirculation mass flow rates in the inner and outer recirculation zone, as well as, the mass entrainment into the wall jet. The entrainment into the flame region is derived based on the outer recirculation zone mass flow rate and the entrainment into the wall jet. At the 10 kW scale 24% of the recirculated mass is entrained into the wall jet, while 76% is entrained into the flame. Note that all volumes and mass flow rates are currently based on CFD simulations, including the simulations at larger scales, in order to evaluate the rector network performance independent from scaling models for these parameters.

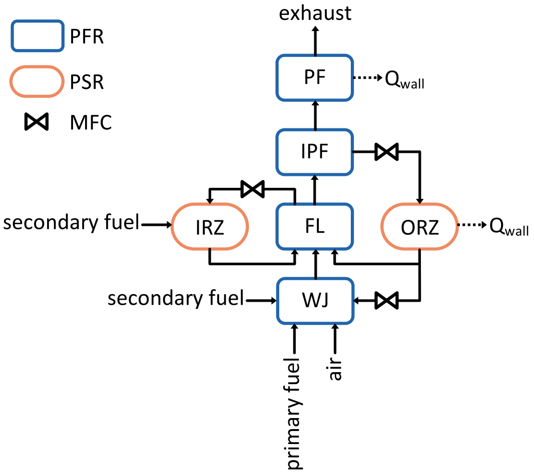

Figure 5.5: Reactor network layout. PSRs are modelled by a single reactor, while PFR are represented by several PSRs, which are not shown in the drawing

Based on the regions, shown in figure 5.4, a reactor network was established. The network layout is shown in figure 5.5. The presented network is in a early development stage and based on several simplifying assumptions. The inner recirculation zone only exchanges mass with the flame region, while the outer recirculation zone exchanges mass with the flame and the wall jet region. Heat losses to the combustion chamber are only accounted for in the outer recirculation zone and in the post flame. These two zones have both direct contact with the chamber wall. Radiative heat exchange between other reactors and the walls are neglected. From the CFD simulations it is known that increasing the secondary fuel fraction leads to an enrichment of the inner recirculation zone. A predefined fraction, currently 50%, of secondary fuel is, therefore, directly injected into the inner recirculation zone, while the remaining part is, together with the primary fuel, injected into the wall jet region. The direct secondary fuel injection into the inner recirculation zone, leads at the 10 kW scale to an equivalence ratio of 1.07 in the inner recirculation zone, compared to 1.05 in the CFD simulations. The outer recirculation zone, on the other hand, is characterized by an equivalence ratio of 0.87, which is equal to the global equivalence ratio. The heat exchange with the chamber wall and the relative long residence time in this region, leads furthermore to the equilibration between gas and wall temperature at 1300 K, while the CFD simulations predict a average temperature of 1442 K.

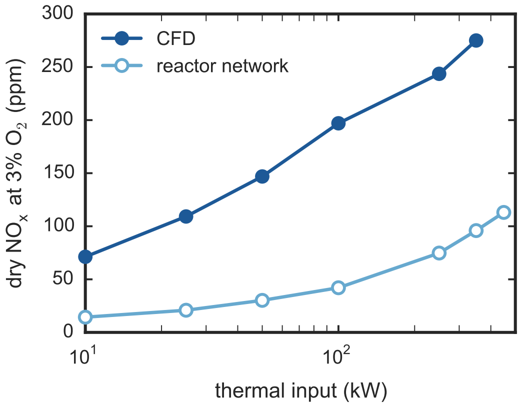

Figure 5.6: Predicted global NO_x emissions for constant velocity scaling based on CFD simulations and the reactor network model.

The combustion kinetic in the reactors is described by the mechanism by Li et al. [73], which is the same mechanism as in the RANS and LES simulations. NO_x is, at the current stage, computed simultaneously to the combustion processes, based on the extended Zeldovich mechanism [143]. Hence, only the mean reactor conditions are considered and the model is expected to underpredict NO_x formation, as discussed in section 2.6. Figure 5.6 shows the comparison between the NO_x predictions by the CFD model and the reactor network model for constant velocity scaling. Constant residence time scaling has not yet been modelled by the reactor network, since the model still needs to be further improved before it can be utilized to draw conclusions on the burner scalability. It can be seen that the emissions are, as expected, underpredicted. The overall trend is, however, similar in the CFD simulations and the network calculations.

5.2.1 Limitations and future work

It is clear that the reactor network model, in its current implementation, still has several limitations and future work is needed. Some of the limitations are inherent to the reactor network models and cannot be addressed by model improvements. Other limitations, linked to the scaling or the NO_x treatment, can however be further improved.

Reactor networks require the information on reactor volumes and to a certain degree mass flow rates. The simple model, presented in this chapter, is based on the assumption that the major flow characteristics of a burner are preserved over different scales. From paper 3 we know, however, that this assumption is not always true. The breakup of the inner recirculation zone, as observed in paper 3, cannot be predicted by a network model. Hence, the network model is intended to be used in conjunction with CFD and experiments, adding value by allowing the investigation of a wide parameter space at low costs and the analysis of specific parameters that cannot be modified individually in other models, such as the mass flow rate in the recirculation zones.

One of the most pragmatic assumption made in the model is the split of the secondary fuel injection between wall jet and inner recirculation zone, which is kept constant for all burner scales. However, the fuel distribution and premixing will be affected by the upscaling of the burner. Indeed, the CFD simulations showed an increase of the equivalence ratio in the inner recirculation zone with increasing burner scale. The reactor network, however, predicts decreasing equivalence ratios since it does not account for the changed mixing conditions of the secondary fuel stream. This represents a shortcoming of the current model and needs to be addressed by a variable model for the secondary fuel injections in order to achieve a better representations of the conditions in the inner recirculation zone at various burner scales.

From the CFD simulations we, furthermore, know that the PPBB burner exhibits large mixture variations in tangential direction. It is intended to extend the network model with several PFR "streams", mainly for the wall jet and flame region, to account better for tangential variations. This improvement may not be necessary for other burners, such as the often employed swirl burner, which typically are more uniform in tangential direction.

Further improvements for the model are the treatment of PFRs. Currently, only five PSR are used to represent one PFR. This allows a fast model evaluation and speeds the development process up. Initial tests have shown that further increasing the number of PSRs per PFR has little effect on the overall results. However, this has to be verified for the final model. It is also possible to apply different resolutions in the network based on individual PFRs. The flame region is, for example, expected to require a finer resolution compared to the post flame region, where the conditions do not change as rapid as in the flame. The volume of a PFR is, furthermore, uniformly distributed to all PSRs within the PFR. The volume distribution should be updated to reflect the jet expansion, which is of special importance in the immediate post flame region. Since, the PFRs are modelled by multiple PSRs it is possible to connect each single PSR to a neighbouring reactor, which would allow a more refined representation of entrainment. At the current stage the PFR are only connected by the first and last PSR to neighbouring regions, which corresponds to a more traditional PFR definition.

A main concern for the reactor model is the treatment of NO_x formation. It is well known that accounting for temperature fluctuations is crucial for a reasonable description of thermal NO_x in turbulent flames. Since, the current model is still based on mean conditions, this criteria is not fulfilled. Fluctuations can be accounted for by employing stochastic reactor network models. However, these models are more expensive as different states need to be accounted for. Hence, the present work suggests to separate the combustion calculation and NO_x formation, following the same approach as for the RANS simulations. In this way a presumed PDF approach can be employed for the NO_x formation. Work has been initiated to extend the NO_x model by incorporating a clipped-Gaussian PDF similar to the approach described by Hsieh et al. [55].

Chapter 6

Conclusions and outlook

A numerical model of a partially premixed bluff body burner was developed and validated for the analysis of NO_x emissions at various burner scales. Scaling effects, for constant velocity and constant residence time scaling, on the global and flame characteristics were investigated theoretically and numerically. CFD based combustion regime diagrams were employed to obtain a refined representation of the flame characteristics, which are strongly linked to the local flow and mixture conditions. The NO_x formation rate was furthermore scrutinized in predefined characteristic burner regions. The main conclusions regarding the model development, the burner characteristics at the base scale of 10 kW and the analysis of constant velocity and constant residence time scaling are presented in the following sections.

6.1 Model development and validation

The present work shows that the main flow features of the investigated burner, namely the inner and outer recirculation zone, and their extent can be well captured by cost efficient steady state RANS simulations. However, a limitation of these models for the prediction of velocity magnitudes was revealed. This limitation can be overcome by employing scale resolving simulations. A LES, as well as, a SBES modelling approach were successfully applied to two different, non-reacting flow configurations. Both approaches led to a significant improvement of the model accuracy, however, at a substantial increased cost, which are prohibitive for simulations of reacting flow at large burner scales.

The modelling of NO_x formation in partially premixed turbulent flames requires the application of various submodels, which are closely linked to each other. The overall accuracy is strongly dependent on the submodels and can be compromised by a single "weak" submodel. A well balanced model is, therefore, desired. A precise, quantitative prediction of NO_x emissions, for complex burner designs, cannot be expected from Reynolds averaged based models, involving various simplifications, such as wall functions and periodic boundary conditions. However, the present study showed that overall trends for varying operational conditions can be captured to a certain degree. An area that, nonetheless, needs to be further investigated is the effect of secondary fuel on the global NO_x emissions at a low thermal input of 10 kW, which could not be reproduced by the current numerical model. Work on scale resolving simulations, utilizing a FGM approach, has been initiated and forms the basis for future work on this issue.

6.2 Burner characterization

The incorporation of data obtained by detailed CFD simulations in traditional combustion regime diagrams, in the form of colour coded scatter plots and hexbin plots, was proposed for the investigation of combustion characteristics of partially premixed burners. This allows a more refined description of burners that show strong local variations in the combustion and mixing regimes.

The analysis of the combustion regimes showed that primary and secondary fuel burns in two distinct v-shaped regions, mainly in the thin reaction zone regime. The further away the air-fuel mixture is from stoichiometry, the larger is the scatter in the combustion regime diagram, spanning several regimes, including the corrugated flamelets and to a small degree the wrinkled flamelets regime. Primary fuel exhibits a larger equivalence ratio variation compared to secondary fuel, as the mixing time is longer. Since secondary fuel is injected closer to the flame anchor point, it contributes to the fuel enrichment of the inner recirculation zone, leading to a fuel rich recirculation zone at a secondary fuel fraction of 30% and a fuel lean recirculation zone when only primary fuel is utilized.

Adding secondary fuel leads to a shift in the NO_x formation, from the inner recirculation zone to the immediate post flame region, downstream of the inner recirculation zone. The temperature field was found to be relatively constant at high values throughout the inner recirculation zone and the NO_x formation rate showed, under these conditions, a stronger correlation to the O and OH concentration.

The highest NO_x formation rate was found in the concave region of the stoichiometric mixture iso-surface, where fresh air-fuel mixture is mixed with hot products from the inner recirculation zone. This indicates a potential for further NO_x reduction by optimizing the placement and size of the fuel ports, which should be investigated further.

6.3 Scaling analysis

Two different scaling laws, constant velocity and constant residence time scaling, were investigated. Constant velocity scaling showed a shift of the flame towards lower Karlovitz numbers, leading for the majority of the flame to a transition from the thin reaction zone to the corrugated flamelets regime. Constant residence time scaling, on the other hand preserves the combustion regime and the global Damköhler number. It was observed that the CFD simulation in a global representation correspond well with the behaviour expected from scaling theory. However, the analysis of the local scaling effects revealed that constant residence time scaling causes large parts of the flame to follow a constant Karlovitz number close to unity, which contradicts the theory, that is based on a global representation, and evidences the importance of local effects.

The separation between primary and secondary fuel becomes, for both scaling approaches, less distinct at larger scales and collapses at 250 kW. Both scaling laws lead, furthermore, to increased NO_x emissions, but do not reach a plateau within the investigated range. Constant velocity scaling was found to cause more NO_x emissions than constant residence time scaling. In both cases, the immediate post flame and the inner recirculation one were identified as the main contributors to the overall NO_x emissions. Constant residence time scaling leads in all regions to a higher mean volumetric NO_x formation rate. However, due to the larger volumes and residence time the total NO_x formation is larger for constant velocity scaling, with exception of the inner recirculation zone. This was attributed to a different change of the flow conditions and entrainment into the inner recirculation zone, based on the applied scaling approach.

A fundamental different mixing structure was also observed for the analysis of the stoichiometric iso-surface, which is especially apparent for the distribution of the secondary fuel streams. The iso-surface forms four distinct tips at base conditions, which resemble the location of the secondary fuel ports. These tips are preserved for constant residence time scaling but collapse to a single one for constant velocity scaling. Constant velocity scaling preserves, on the other hand, a fuel rich inner recirculation zone, while constant residence time scaling leads to a transition to a fuel lean mixture in the inner recirculation zone.

An important finding for the investigated burner was the sudden breakup of the inner recirculation zone at a scale between 450 kW and 500 kW, when constant velocity scaling is employed. The breakup of the recirculation zone causes the flame to bend outwards and to impinge onto the combustion chamber wall. It was concluded that the fundamental change of the flow field is caused by the different effect of the scaling methods on the velocity to length scale ratio and momentum of the annular jet flow. The annular jet is strongly dependent on the lance height, which can be changed by altering the axial position of the bluff body. This is a unique feature of the PPBB. It should be investigated if the variable lance height can be utilized to stabilize the recirculation zone for constant velocity scaling at scales exceeding 450 kW.

The PPBB is characterized by significant variations in tangential direction, which has a strong impact on the scalability of the burner. The scaling effects, studied in the present work, should therefore also be investigated for burners with a more uniform tangential profile, such as swirl burners, which will add to the general understanding of scaling. The present doctoral thesis confirmed the findings by Hsieh et al. [55] and Cheng et al. [21], that successful scaling requires the consideration of local effects. A reactor network was derived from the CFD simulations and implemented in the Cantera framework, forming the basis for future investigations of the scaling effects and providing the possibility to investigate a wide parameter space at low costs. Future work should, therefore, be focused on the further developing the network model, following the suggestions made in section 5.2.1.

Bibliography

[1] ANSYS_Inc. ANSYS® Academic Fluent, Release 18.1. In *Documentation, Theory Guide*, pages 1–850. ANSYS_Inc, 2017.

[2] A. J. Aspden, M. S. Day, and J. B. Bell. TurbulenceâĂŞflame interactions in lean premixed hydrogen: transition to the distributed burning regime. *Journal of Fluid Mechanics*, 680:287–320, aug 2011. doi: 10.1017/jfm.2011.164.

[3] J. M. Ballester, C. Dopazo, N. Fueyo, M. Hernández, and P. J. Vidal. Investigation of low-NOx strategies for natural gas combustion. *Fuel*, 76(5): 435–446, apr 1997. doi: 10.1016/S0016-2361(97)85521-4.

[4] N. A. Baraiya and S. Chakravarthy. Effect of syngas composition on high frequency combustion instability in a non-premixed turbulent combustor. *International Journal of Hydrogen Energy*, 44(12):6299–6312, mar 2019. doi: 10.1016/j.ijhydene.2019.01.115.

[5] R. Barlow and C. Carter. Raman/Rayleigh/LIF measurements of nitric oxide formation in turbulent hydrogen jet flames. *Combustion and Flame*, 97(3-4):261–280, jun 1994. doi: 10.1016/0010-2180(94)90020-5.

[6] G. K. Batchelor. An introduction to fluid dynamics. *Quarterly Journal of the Royal Meteorological Society*, 94(401):435–435, jul 1968. doi: 10.1002/qj.49709440128.

[7] C. Baukal and R. E. Schwartz. *The John Zink Combustion Handbook*. CRC Press LLC, first edition, 2001. ISBN 0849323371.

[8] D. L. Baulch, C. T. Bowman, C. J. Cobos, R. A. Cox, T. Just, J. A. Kerr, M. J. Pilling, D. Stocker, J. Troe, W. Tsang, R. W. Walker, and J. Warnatz. Evaluated Kinetic Data for Combustion Modeling: Supplement II. *Journal of Physical and Chemical Reference Data*, 34(3):757–1397, sep 2005. doi: 10.1063/1.1748524.

[9] J. Beér. The Significance of Modelling. *Journal of Insitute of Fuel*, 39: 466–473, 1966.

[10] J. Bell, M. Day, and M. Lijewski. Simulation of nitrogen emissions in a premixed hydrogen flame stabilized on a low swirl burner. *Proceedings of the Combustion Institute*, 34(1):1173–1182, jan 2013. doi: 10.1016/j.proci.2012.07.046.

[11] U. Bollettini, F. Breussin, and R. Weber. A study on scaling of natural gas burners. *IFRF Combustion Journal*, 2000.

[12] J. W. Bozzelli and A. M. Dean. O + NNH: A possible new route for NOX formation in flames. *International Journal of Chemical Kinetics*, 27(11): 1097–1109, nov 1995. doi: 10.1002/kin.550271107.

[13] H. J. Burbano, J. Pareja, and A. A. Amell. Laminar burning velocities and flame stability analysis of H2/CO/air mixtures with dilution of N2 and CO2. *International Journal of Hydrogen Energy*, 36(4):3232–3242, feb 2011. doi: 10.1016/j.ijhydene.2010.11.089.

[14] R. Cabra, T. Myhrvold, J. Chen, R. Dibble, A. Karpetis, and R. Barlow. Simultaneous laser raman-rayleigh-lif measurements and numerical modeling results of a lifted turbulent H2/N2 jet flame in a vitiated coflow. *Proceedings of the Combustion Institute*, 29(2):1881–1888, jan 2002. doi: 10.1016/S1540-7489(02)80228-0.

[15] C. D. Carter and R. S. Barlow. Simultaneous measurements of NO, OH, and the major species in turbulent flames. *Optics Letters*, 19(4):299, feb 1994. doi: 10.1364/OL.19.000299.

[16] S. Chaudhuri and B. M. Cetegen. Blowoff characteristics of bluff-body stabilized conical premixed flames with upstream spatial mixture gradients and velocity oscillations. *Combustion and Flame*, 153(4):616–633, jun 2008. doi: 10.1016/j.combustflame.2007.12.008.

[17] H. C. Chen and V. C. Patel. Near-wall turbulence models for complex flows including separation. *AIAA Journal*, 26(6):641–648, jun 1988. doi: 10.2514/3.9948.

[18] J.-Y. Chen and W. Kollmann. PDF modeling and analysis of thermal NO formation in turbulent nonpremixed hydrogen-air jet flames. *Combustion and Flame*, 88(3-4):397–412, mar 1992. doi: 10.1016/0010-2180(92)90042-N.

[19] R.-H. Chen and J. F. Driscoll. Nitric oxide levels of jet diffusion flames: Effects of coaxial air and other mixing parameters. *Symposium (International) on Combustion*, 23(1):281–288, jan 1991. doi: 10.1016/S0082-0784(06)80271-7.

[20] R. Cheng and A. Oppenheim. Autoignition in methane-hydrogen mixtures. *Combustion and Flame*, 58(2):125–139, nov 1984. doi: 10.1016/0010-2180(84)90088-9.

[21] R. Cheng, D. Yegian, M. Miyasato, G. Samuelsen, C. Benson, R. Pellizzari, and P. Loftus. Scaling and development of low-swirl burners for low-emission furnaces and boilers. *Proceedings of the Combustion Institute*, 28 (1):1305–1313, jan 2000. doi: 10.1016/S0082-0784(00)80344-6.

[22] P. Chiesa, G. Lozza, and L. Mazzocchi. Using Hydrogen as Gas Turbine Fuel. *Journal of Engineering for Gas Turbines and Power*, 127(1):73, 2005. doi: 10.1115/1.1787513.

[23] F. C. Christo and B. B. Dally. Modeling turbulent reacting jets issuing into a hot and diluted coflow. *Combustion and Flame*, 142:117–129, 2005. doi: 10.1016/j.combustflame.2005.03.002.

[24] J. A. Cole, T. P. Parr, N. C. Widmer, K. J. Wilson, K. C. Schadow, and W. R. Seeker. Scaling criteria for the development of an acoustically stabilized dump combustor. *Proceedings of the Combustion Institute*, 28(1):1297–1304, jan 2000. doi: 10.1016/S0082-0784(00)80343-4.

[25] B. Collonval, Frederic. *Modeling of auto-ignition and NOx formation in turbulent reacting flows*. PhD thesis, TUM, 2015.

[26] C.-C. Cormos. Evaluation of power generation schemes based on hydrogen-fueled combined cycle with carbon capture and storage (CCS). *International Journal of Hydrogen Energy*, 36(5):3726–3738, 2011. doi: 10.1016/j.ijhydene.2010.12.042.

[27] C.-C. Cormos. Economic implications of pre- and post-combustion calcium looping configurations applied to gasification power plants. *International Journal of Hydrogen Energy*, 39(20):10507–10516, jul 2014. doi: 10.1016/j.ijhydene.2014.05.033.

[28] S. M. Correa. A Review of NO x Formation Under Gas-Turbine Combustion Conditions. *Combustion Science and Technology*, 87(1-6):329–362, jan 1993. doi: 10.1080/00102209208947221.

[29] B. Cuenot and T. Poinsot. Asymptotic and numerical study of diffusion flames with variable Lewis number and finite rate chemistry. *Combustion and Flame*, 104(1-2):111–137, jan 1996. doi: 10.1016/0010-2180(95)00111-5.

[30] B. Dam, G. Corona, M. Hayder, and A. Choudhuri. Effects of syngas composition on combustion induced vortex breakdown (CIVB) flashback in a swirl stabilized combustor. *Fuel*, 90:3274–3284, 2011. doi: 10.1016/j.fuel.2011.06.024.

[31] D. Davu, R. Franco, A. Choudhuri, and R. Lewis. Investigation on Flashback Propensity of Syngas Premixed Flames. In *41st AIAA/ASME/SAE/ASEE Joint Propulsion Conference & Exhibit*, pages 1–11, Reston, Virigina, jul 2005. American Institute of Aeronautics and Astronautics. ISBN 978-1-62410-063-5. doi: 10.2514/6.2005-3585.

[32] J. Dawson, R. Gordon, J. Kariuki, E. Mastorakos, A. Masri, and M. Juddoo. Visualization of blow-off events in bluff-body stabilized turbulent premixed flames. *Proceedings of the Combustion Institute*, 33(1):1559–1566, 2011. doi: 10.1016/j.proci.2010.05.044.

[33] M. S. Day, J. B. Bell, X. Gao, and P. Glarborg. Numerical simulation of nitrogen oxide formation in lean premixed turbulent H2/O2/N2 flames. *Proceedings of the Combustion Institute*, 33(1):1591–1599, jan 2011. doi: 10.1016/j.proci.2010.06.128.

[34] S. Dunn. Hydrogen futures: toward a sustainable energy system. *International Journal of Hydrogen Energy*, 27(3):235–264, mar 2002. doi: 10.1016/S0360-3199(01)00131-8.

[35] M. Dutka, M. Ditaranto, and T. Løvås. Application of a Central Composite Design for the Study of NOx Emission Performance of a Low NOx Burner. *Energies*, 8(5):3606–3627, apr 2015. doi: 10.3390/en8053606.

[36] M. Dutka, M. Ditaranto, and T. Løvås. Emission characteristics of a novel low NO x burner fueled by hydrogen-rich mixtures with methane. *Journal of Power Technologies*, 95(2):105–111, 2015.

[37] M. Dutka, M. Ditaranto, and T. Løvås. Investigations of air flow behavior past a conical bluff body using particle imaging velocimetry. *Experiments in Fluids*, 56(11):199, nov 2015. doi: 10.1007/s00348-015-2068-6.

[38] M. Dutka, M. Ditaranto, and T. Løvås. NOx emissions and turbulent flow field in a partially premixed bluff body burner with CH4 and H2 fuels. *International Journal of Hydrogen Energy*, 41(28):12397–12410, jul 2016. doi: 10.1016/j.ijhydene.2016.05.154.

[39] T. Echekki and E. Mastorakos, editors. *Turbulent Combustion Modeling*, volume 95 of *Fluid Mechanics and Its Applications*. Springer Netherlands, Dordrecht, 2011. ISBN 978-94-007-0411-4. doi: 10.1007/978-94-007-0412-1.

[40] A. Eroglu, K. Döbbeling, F. Joos, and P. Brunner. Vortex generators in lean-premix combustion. *Journal of Engineering for Gas Turbines and Power*, 123(1):41–49, 2001. doi: 10.1115/1.1335481.

[41] I. S. Ertesvåg and B. F. Magnussen. The Eddy Dissipation Turbulence Energy Cascade Model. *Combustion Science and Technology*, 159(1):213–235, oct 2000. doi: 10.1080/00102200008935784.

[42] V. Fichet, M. Kanniche, P. Plion, and O. Gicquel. A reactor network model for predicting NOx emissions in gas turbines. *Fuel*, 89(9):2202–2210, sep 2010. doi: 10.1016/j.fuel.2010.02.010.

[43] B. Fiorina, R. Mercier, G. Kuenne, A. Ketelheun, A. Avdić, J. Janicka, D. Geyer, A. Dreizler, E. Alenius, C. Duwig, P. Trisjono, K. Kleinheinz, S. Kang, H. Pitsch, F. Proch, F. Cavallo Marincola, and A. Kempf. Challenging modeling strategies for LES of non-adiabatic turbulent stratified combustion. *Combustion and Flame*, 162(11):4264–4282, nov 2015. doi: 10.1016/j.combustflame.2015.07.036.

[44] B. Fiorina, D. Veynante, and S. Candel. Modeling Combustion Chemistry in Large Eddy Simulation of Turbulent Flames. *Flow, Turbulence and Combustion*, 94(1):3–42, jan 2015. doi: 10.1007/s10494-014-9579-8.

[45] J. Fritz, M. Kröner, and T. Sattelmayer. Flashback in a Swirl Burner With Cylindrical Premixing Zone. In *Volume 2: Coal, Biomass and Alternative Fuels; Combustion and Fuels; Oil and Gas Applications; Cycle Innovations*, page V002T02A021. ASME, jun 2001. ISBN 978-0-7918-7851-4. doi: 10.1115/2001-GT-0054.

[46] L. Gicquel, G. Staffelbach, and T. Poinsot. Large Eddy Simulations of gaseous flames in gas turbine combustion chambers. *Progress in Energy and Combustion Science*, 38(6):782–817, dec 2012. doi: 10.1016/j.pecs.2012.04.004.

[47] P. Glarborg, J. A. Miller, B. Ruscic, and S. J. Klippenstein. Modeling nitrogen chemistry in combustion. *Progress in Energy and Combustion Science*, 67:31–68, jul 2018. doi: 10.1016/j.pecs.2018.01.002.

[48] D. G. Goodwin, R. L. Speth, H. K. Moffat, and B. W. Weber. Cantera: An object-oriented software toolkit for chemical kinetics, thermodynamics, and transport processes, 2018.

[49] I. R. Gran and B. F. Magnussen. A numerical study of a bluff-body stabilized diffusion flame. Part 2. Influence of combustion modeling and finite-rate chemistry. *Combustion Science and Technology*, 119(1-6):191–217, 1996. doi: 10.1080/00102209608951999.

[50] P. Guo, S. Zang, and B. Ge. Technical Brief: Predictions of Flow Field for Circular-Disk Bluff-Body Stabilized Flame Investigated by Large Eddy Simulation and Experiments. *Journal of Engineering for Gas Turbines and Power*, 132(5):054503, sep 2010. doi: 10.1115/1.3205029.

[51] E. R. Hawkes and J. H. Chen. Direct numerical simulation of hydrogen-enriched lean premixed methaneâĂŞair flames. *Combustion and Flame*, 138(3):242–258, aug 2004. doi: 10.1016/j.combustflame.2004.04.010.

[52] D. Haworth. Progress in probability density function methods for turbulent reacting flows. *Progress in Energy and Combustion Science*, 36(2):168–259, apr 2010. doi: 10.1016/j.pecs.2009.09.003.

[53] A. C. Hindmarsh, P. N. Brown, K. E. Grant, S. L. Lee, R. Serban, D. E. Shumaker, and C. S. Woodward. SUNDIALS: Suite of Nonlinear and Differential/Algebraic Equation Solvers ALAN. *ACM Transactions on Mathematical Software*, 31(3):363–396, sep 2005. doi: 10.1145/1089014.1089020.

[54] S. Hoffmann, P. Habisreuther, and B. Lenze. Development and assessment of correlations for predicting stability limits of swirling flames. *Chemical Engineering and Processing: Process Intensification*, 33(5):393–400, nov 1994. doi: 10.1016/0255-2701(94)02011-6.

[55] T.-C. Hsieh, W. J. Dahm, and J. F. Driscoll. Scaling Laws for NOx Emission Performance of Burners and Furnaces from 30 kW to 12 MW. *Combustion and Flame*, 114(1-2):54–80, jul 1998. doi: 10.1016/S0010-2180(97)00289-7.

[56] T. Hussain, M. Talibi, and R. Balachandran. Investigating the effect of local addition of hydrogen to acoustically excited ethylene and methane flames. *International Journal of Hydrogen Energy*, 44(21):11168–11184, apr 2019. doi: 10.1016/j.ijhydene.2019.02.182.

[57] T. Jongen. *Simulation and Modeling of Turbulent Incompressible Flows*. PhD thesis, Lausanne, EPFL, 1992.

[58] S. Joo, J. Yoon, J. Kim, M. Lee, and Y. Yoon. NOx emissions characteristics of the partially premixed combustion of H2/CO/CH4 syngas using artificial

neural networks. *Applied Thermal Engineering*, 80:436–444, apr 2015. doi: 10.1016/j.applthermaleng.2015.01.057.

[59] H. A. jr McGee. *Molecular Engineering*. McGraw-Hill, New York, 1st edition, 1991. ISBN 0-07-044977-5.

[60] J. Kariuki, J. R. Dawson, and E. Mastorakos. Measurements in turbulent premixed bluff body flames close to blow-off. *Combustion and Flame*, 159 (8):2589–2607, aug 2012. doi: 10.1016/j.combustflame.2012.01.005.

[61] R. J. Kee, M. E. Coltrin, P. Glarborg, and H. Zhu. *Chemically Reacting Flow: Theory and Practice*. John Wiley and Sons, 2nd edition, 2017. ISBN ISBN: 978-1-119-18487-4.

[62] J. Kent and R. Bilger. The prediction of turbulent diffusion flame fields and nitric oxide formation. *Symposium (International) on Combustion*, 16(1): 1643–1656, jan 1977. doi: 10.1016/S0082-0784(77)80443-8.

[63] H. Kido and M. Nakahara. A Model of Turbulent Burning Velocity Taking the Preferential Diffusion Effect into Consideration. *JSME International Journal Series B*, 41(3):666–673, 1998. doi: 10.1299/jsmeb.41.666.

[64] S.-E. Kim and D. Choudhury. A Near-Wall Treatment Using Wall Functions Sensitized to Pressure Gradient. *ASME -PUBLICATIONS- FED*, 217:273–280, 1995.

[65] S. J. Klippenstein, L. B. Harding, P. Glarborg, and J. A. Miller. The role of NNH in NO formation and control. *Combustion and Flame*, 158(4): 774–789, apr 2011. doi: 10.1016/j.combustflame.2010.12.013.

[66] V. Kolár, P. Filip, and A. G. Curev. Similarity prediction of wall jets on bodies of revolution. *Acta Mechanica*, 76(3-4):253–263, mar 1989. doi: 10.1007/BF01253584.

[67] A. Konnov. On the relative importance of different routes forming NO in hydrogen flames. *Combustion and Flame*, 134(4):421–424, sep 2003. doi: 10.1016/S0010-2180(03)00135-4.

[68] A. Konnov, G. Colson, and J. De Ruyck. NO formation rates for hydrogen combustion in stirred reactors. *Fuel*, 80(1):49–65, jan 2001. doi: 10.1016/S0016-2361(00)00060-0.

[69] B. Launder and B. D. Spalding. *Lectures in Mathematical Models of Turbulence*. Academic Press Inc, London, England, 1972.

[70] G. A. Lavoie and A. F. Schlander. A Scaling Study of NO Formation in Turbulent Diffusion Flames of Hydrogen Burning in Air. *Combustion Science and Technology*, 8(5-6):215–224, dec 1973. doi: 10.1080/00102207308946645.

[71] C. Law. Dynamics of stretched flames. *Symposium (International) on Combustion*, 22(1):1381–1402, jan 1989. doi: 10.1016/S0082-0784(89)80149-3.

[72] M. T. Lewandowski and I. S. Ertesvåg. Analysis of the Eddy Dissipation Concept formulation for MILD combustion modelling. *Fuel*, 224:687–700, jul 2018. doi: 10.1016/j.fuel.2018.03.110.

[73] J. Li, Z. Zhao, A. Kazakov, and F. L. Dryer. An updated comprehensive kinetic model of hydrogen combustion. *International Journal of Chemical Kinetics*, 36(10):566–575, oct 2004. doi: 10.1002/kin.20026.

[74] T. Lieuwen, V. McDonell, E. Petersen, and D. Santavicca. Fuel Flexibility Influences on Premixed Combustor Blowout, Flashback, Autoignition, and Stability. *Journal of Engineering for Gas Turbines and Power*, 130(1):011506, 2008. doi: 10.1115/1.2771243.

[75] T. Lieuwen, V. McDonell, D. Santavicca, and T. Sattelmayer. Burner Development and Operability Issues Associated with Steady Flowing Syngas Fired Combustors. *Combustion Science and Technology*, 180(6):1169–1192, may 2008. doi: 10.1080/00102200801963375.

[76] Y.-C. Lin, S. Daniele, P. Jansohn, and K. Boulouchos. Turbulent Flame Speed as an Indicator for Flashback Propensity of Hydrogen-Rich Fuel Gases. *Journal of Engineering for Gas Turbines and Power*, 135(11):111503, sep 2013. doi: 10.1115/1.4025068.

[77] A. Lipatnikov and J. Chomiak. Turbulent flame speed and thickness: phenomenology, evaluation, and application in multi-dimensional simulations. *Progress in Energy and Combustion Science*, 28(1):1–74, jan 2002. doi: 10.1016/S0360-1285(01)00007-7.

[78] B. Magnussen. On the structure of turbulence and a generalized eddy dissipation concept for chemical reaction in turbulent flow. In *19th Aerospace Sciences Meeting*, pages 1–6, Reston, Virigina, jan 1981. American Institute of Aeronautics and Astronautics. doi: 10.2514/6.1981-42.

[79] B. Magnussen and B. Hjertager. On mathematical modeling of turbulent combustion with special emphasis on soot formation and combustion.

Symposium (International) on Combustion, 16(1):719–729, jan 1977. doi: 10.1016/S0082-0784(77)80366-4.

[80] C. Mayer, J. Sangl, T. Sattelmayer, T. Lachaux, and S. Bernero. Study on the Operational Window of a Swirl Stabilized Syngas Burner Under Atmospheric and High Pressure Conditions. *Journal of Engineering for Gas Turbines and Power*, 134(3):031506, 2012. doi: 10.1115/1.4004255.

[81] S. Meares and A. R. Masri. A modified piloted burner for stabilizing turbulent flames of inhomogeneous mixtures. *Combustion and Flame*, 161(2): 484–495, feb 2014. doi: 10.1016/j.combustflame.2013.09.016.

[82] N. Megalos, N. Smith, and D. Zhang. The potential for low NOx from a precessing jet burner of coal. *Combustion and Flame*, 124(1-2):50–64, jan 2001. doi: 10.1016/S0010-2180(00)00173-5.

[83] W. Meier, X. Duan, and P. Weigand. Investigations of swirl flames in a gas turbine model combustor. *Combustion and Flame*, 144(1-2):225–236, jan 2006. doi: 10.1016/j.combustflame.2005.07.009.

[84] F. R. Menter. Two-equation eddy-viscosity turbulence models for engineering applications. *AIAA Journal*, 32(8):1598–1605, aug 1994. doi: 10.2514/3.12149.

[85] F. R. Menter. Best Practice : Scale - Resolving Simulations in ANSYS CFD. Technical Report 2.00, 2015.

[86] F. R. Menter. Stress-Blended Eddy Simulation (SBES) - A new Paradigm in hybrid RANS-LES Modeling. In *6th Symposium on Hybrid RANS-LES Methods*, pages 1–17, Strasbourg, France, 2016.

[87] C. Meraner, T. Li, M. Ditaranto, and T. Løvås. Cold flow characteristics of a novel bluff body hydrogen burner. *International Journal of Hydrogen Energy*, 43(14):7155–7168, apr 2018. doi: 10.1016/j.ijhydene.2018.02.062.

[88] J. A. Miller and C. T. Bowman. Mechanism and modeling of nitrogen chemistry in combustion. *Progress in Energy and Combustion Science*, 15(4): 287–338, jan 1989. doi: 10.1016/0360-1285(89)90017-8.

[89] J. Morrison and D. Gregory-Smith. Calculation of an axisymmetric turbulent wall jet over a surface of convex curvature. *International Journal of Heat and Fluid Flow*, 5(3):139–148, sep 1984. doi: 10.1016/0142-727X(84)90071-7.

[90] F. Nicoud and F. Ducros. Subgrid-Scale Stress Modelling Based on the Square of the Velocity Gradient Tensor. *Flow, Turbulence and Combustion*, 62(3):183–200, 1999. doi: 10.1023/A:1009995426001.

[91] V. Nilsen and G. Kosály. Differential diffusion in turbulent reacting flows. *Combustion and Flame*, 117(3):493–513, may 1999. doi: 10.1016/S0010-2180(98)00113-8.

[92] M. Ó Conaire, H. J. Curran, J. M. Simmie, W. J. Pitz, and C. K. Westbrook. A comprehensive modeling study of hydrogen oxidation. *International Journal of Chemical Kinetics*, 36(11):603–622, nov 2004. doi: 10.1002/kin.20036.

[93] J. V. OIJEN and L. D. GOEY. Modelling of Premixed Laminar Flames using Flamelet-Generated Manifolds. *Combustion Science and Technology*, 161(1):113–137, dec 2000. doi: 10.1080/00102200008935814.

[94] B. A. Perry, M. E. Mueller, and A. R. Masri. A two mixture fraction flamelet model for large eddy simulation of turbulent flames with inhomogeneous inlets. *Proceedings of the Combustion Institute*, 36(2):1767–1775, 2017. doi: 10.1016/j.proci.2016.07.029.

[95] N. Peters. An Asymptotic Analysis of Nitric Oxide Formation in Turbulent Diffusion Flames. *Combustion Science and Technology*, 19(1-2):39–49, nov 1978. doi: 10.1080/00102207808946862.

[96] H. Pitsch. Unsteady flamelet modeling of differential diffusion in turbulent jet diffusion flames. *Combustion and Flame*, 123(3):358–374, nov 2000. doi: 10.1016/S0010-2180(00)00135-8.

[97] H. Pitsch. Improved pollutant predictions in large-eddy simulations of turbulent non-premixed combustion by considering scalar dissipation rate fluctuations. *Proceedings of the Combustion Institute*, 29(2):1971–1978, jan 2002. doi: 10.1016/S1540-7489(02)80240-1.

[98] H. Pitsch, M. Chen, and N. Peters. Unsteady flamelet modeling of turbulent hydrogen-air diffusion flames. *Symposium (International) on Combustion*, 27(1):1057–1064, jan 1998. doi: 10.1016/S0082-0784(98)80506-7.

[99] T. Poinsot and D. Veynante. *Theoretical and Numerical Combustion*. Toulouse, 2012. ISBN 978-2-7466-3990-4.

[100] S. B. Pope. Small scales, many species and the manifold challenges of turbulent combustion. *Proceedings of the Combustion Institute*, 34(1):1–31, jan 2013. doi: 10.1016/j.proci.2012.09.009.

[101] L. Rayleigh. *The Theory of Sound*. MacMillan, London, 1896.

[102] G. Richards, M. McMillian, R. Gemmen, W. Rogers, and S. Cully. Issues for low-emission, fuel-flexible power systems. *Progress in Energy and Combustion Science*, 27(2):141–169, jan 2001. doi: 10.1016/S0360-1285(00)00019-8.

[103] N. A. Røkke, J. E. Hustad, and O. K. Sønju. A study of partially premixed unconfined propane flames. *Combustion and Flame*, 97(1):88–106, apr 1994. doi: 10.1016/0010-2180(94)90118-X.

[104] M. Sadakata and Y. Hirose. Scaling law for pollutant emission from a combustion furnace. *Fuel*, 73(8):1338–1342, aug 1994. doi: 10.1016/0016-2361(94)90310-7.

[105] K. C. San, Y. Z. Huang, and S. C. Yen. Flame Patterns and Combustion Intensity Behind Rifled Bluff-Body Frustums. *Journal of Engineering for Gas Turbines and Power*, 135(12):121502, sep 2013. doi: 10.1115/1.4025262.

[106] R. Sankaran and H. G. Im. Effects of hydrogen addition on the Markstein length and flammability limit of streched methane/air premixed flames. *Combustion Science and Technology*, 178(9):1585–1611, sep 2006. doi: 10.1080/00102200500536217.

[107] Y. C. See and M. Ihme. Large eddy simulation of a partially-premixed gas turbine model combustor. *Proceedings of the Combustion Institute*, 35(2): 1225–1234, 2015. doi: 10.1016/j.proci.2014.08.006.

[108] F. Seffrin, F. Fuest, D. Geyer, and A. Dreizler. Flow field studies of a new series of turbulent premixed stratified flames. *Combustion and Flame*, 157 (2):384–396, feb 2010. doi: 10.1016/j.combustflame.2009.09.001.

[109] R. Sharma and S. Patankar. Numerical computations of wall-jet flows. *International Journal of Heat and Mass Transfer*, 25(11):1709–1718, nov 1982. doi: 10.1016/0017-9310(82)90150-8.

[110] R. N. Sharma. Experimental Investigation of Conical Wall Jets. *AIAA Journal*, 19(1):28–33, 1981. doi: 10.2514/3.7746.

[111] T.-H. Shih, W. W. Liou, A. Shabbir, Z. Yang, and J. Zhu. A new k-epsilon eddy viscosity model for high reynolds number turbulent flows. *Computers & Fluids*, 24(3):227–238, mar 1995. doi: 10.1016/0045-7930(94)00032-T.

[112] J. Smagorinsky. General Circulation Experiments with the Primitive Equations. *Monthly Weather Review*, 91(3):99–164, mar 1963. doi: 10.1175/1520-0493(1963)091<0099:GCEWTP>2.3.CO;2.

[113] J. P. Smart and W. L. D. Van Kamp. The Impact of Scaling Criteria on the Characteristics of Pulverised Coal Flames. *Developments in Chemical Engineering and Mineral Processing*, 7(3-4):301–331, 1999. doi: 10.1002/apj.5500070305.

[114] G. P. Smith, D. M. Golden, M. Frenklach, N. W. Moriarty, B. Eiteneer, M. Goldenberg, C. T. Bowman, R. K. Hanson, S. Song, W. C. J. Gardiner, V. V. Lissianski, and Z. Qin. GRI-Mech 3.0, 2018.

[115] N. Smith, R. Bilger, and J.-Y. Chen. Modelling of nonpremixed hydrogen jet flames using a conditional moment closure method. *Symposium (International) on Combustion*, 24(1):263–269, jan 1992. doi: 10.1016/S0082-0784(06)80035-4.

[116] D. Spalding. Mixing and chemical reaction in steady confined turbulent flames. *Symposium (International) on Combustion*, 13(1):649–657, jan 1971. doi: 10.1016/S0082-0784(71)80067-X.

[117] D. Spalding, H. Hottel, S. Bragg, A. Lefebvre, D. Shepherd, and A. Scurlock. The art of partial modeling. *Symposium (International) on Combustion*, 9(1):833–843, jan 1963. doi: 10.1016/S0082-0784(63)80090-9.

[118] Ø. Spangelo. *Teoretisk og eksperimentell undersøkelse av lav-NOx brennerkonsepter*. PhD thesis, NTNU, 2000.

[119] Ø. Spangelo, O. Sonju, T. Slungaard, and M. Ditaranto. US 20090220899 A1, 2009.

[120] R. L. Speth and A. F. Ghoniem. Using a strained flame model to collapse dynamic mode data in a swirl-stabilized syngas combustor. *Proceedings of the Combustion Institute*, 32(2):2993–3000, 2009. doi: 10.1016/j.proci.2008.05.072.

[121] J. Stefan. Sitzungsberichte Akademie der Wissenschaften in Wien II. Technical report, 1874.

[122] G. Szego, B. Dally, and G. Nathan. Scaling of NOx emissions from a laboratory-scale mild combustion furnace. *Combustion and Flame*, 154(1-2):281–295, jul 2008. doi: 10.1016/j.combustflame.2008.02.001.

[123] S. Taamallah, K. Vogiatzaki, F. Alzahrani, E. Mokheimer, M. Habib, and A. Ghoniem. Fuel flexibility, stability and emissions in premixed hydrogen-rich gas turbine combustion: Technology, fundamentals, and numerical simulations. *Applied Energy*, 154:1020–1047, sep 2015. doi: 10.1016/j.apenergy.2015.04.044.

[124] Y. Tong, M. Li, J. Klingmann, S. Chen, and Z. Li. Experimental Investigation on the Influences of Bluff-Body's Position on Diffusion Flame Structures. In *Volume 1: Boilers and Heat Recovery Steam Generator; Combustion Turbines; Energy Water Sustainability; Fuels, Combustion and Material Handling; Heat Exchangers, Condensers, Cooling Systems, and Balance-of-Plant*, page V001T04A009. ASME, jun 2017. ISBN 978-0-7918-5760-1. doi: 10.1115/POWER-ICOPE2017-3090.

[125] S. R. Turns. Understanding NOx formation in nonpremixed flames: experiments and modeling. *Prog. Energy Combust. Sci.*, 21:361–385, 1995.

[126] S. R. Turns. *Introduction to Combustion Concepts and Applications*. Mcgraw Hill Higher Education, New York, 3rd edition, 2011. ISBN 978-0071086875.

[127] S. R. Turns and F. H. Myhr. Oxides of nitrogen emissions from turbulent jet flames: Part IâĂŤFuel effects and flame radiation. *Combustion and Flame*, 87(3-4):319–335, dec 1991. doi: 10.1016/0010-2180(91)90116-S.

[128] S. R. Turns, F. H. Myhr, R. V. Bandaru, and E. R. Maund. Oxides of nitrogen emissions from turbulent jet flames: Part IIâĂŤFuel dilution and partial premixing effects. *Combustion and Flame*, 93(3):255–269, may 1993. doi: 10.1016/0010-2180(93)90107-E.

[129] D. Van Krevelen and H. Chermin. Generalized flame stability diagram for the prediction of interchangeability of gases. *Symposium (International) on Combustion*, 7(1):358–368, 1958. doi: 10.1016/S0082-0784(58)80066-1.

[130] J. A. Van Oijen, A. Donini, R. J. M. Bastiaans, J. H. M. Ten, T. Boonkkamp, and L. P. H. De Goey. State-of-the-art in premixed combustion modeling using flamelet generated manifolds. *Progress in Energy and Combustion Science*, 57:30–74, 2016. doi: 10.1016/j.pecs.2016.07.001.

[131] B. van Ruijven, D. P. van Vuuren, and B. de Vries. The potential role of hydrogen in energy systems with and without climate policy. *International Journal of Hydrogen Energy*, 32(12):1655–1672, aug 2007. doi: 10.1016/j.ijhydene.2006.08.036.

[132] A. Vranos, B. Knight, W. Proscia, L. Chiappetta, and M. Smooke. Nitric oxide formation and differential diffusion in a turbulent methane-hydrogen diffusion flame. *Symposium (International) on Combustion*, 24(1):377–384, jan 1992. doi: 10.1016/S0082-0784(06)80049-4.

[133] J. Warnatz, U. Maas, and R. W. Dibble. *Combustion*. Springer Berlin Heidelberg, 2006. ISBN 978-3-540-25992-3. doi: 10.1007/978-3-540-45363-5.

[134] R. Weber. Scaling characteristics of aerodynamics, heat transfer, and pollutant emissions in industrial flames. *Symposium (International) on Combustion*, 26(2):3343–3354, 1996. doi: 10.1016/S0082-0784(96)80182-2.

[135] R. Weber, J. F. Driscoll, W. J. Dahm, and R. T. Waibel. Scaling Characteristics of Aerodynamics and Low-NOx Properties of Industrial Natural Gas Burners. The SCALING 400 Study. Part I: Test Plan. Technical report, GRI Topoical Report 93/0227, Gas Research Institute, Chicago, 1993.

[136] P. Weigand, W. Meier, X. Duan, W. Stricker, and M. Aigner. Investigations of swirl flames in a gas turbine model combustor. *Combustion and Flame*, 144(1-2):205–224, jan 2006. doi: 10.1016/j.combustflame.2005.07.010.

[137] K. J. Whitty, H. R. Zhang, and E. G. Eddings. Emissions from Syngas Combustion. *Combustion Science and Technology*, 180(6):1117–1136, may 2008. doi: 10.1080/00102200801963326.

[138] A. Widenhorn, B. Noll, and M. Aigner. *High Performance Computing in Science and Engineering '09*. Springer Berlin Heidelberg, Berlin, Heidelberg, 2010. ISBN 978-3-642-04664-3. doi: 10.1007/978-3-642-04665-0.

[139] M. Wolfshtein. The velocity and temperature distribution in one-dimensional flow with turbulence augmentation and pressure gradient. *International Journal of Heat and Mass Transfer*, 12(3):301–318, mar 1969. doi: 10.1016/0017-9310(69)90012-X.

[140] M. S. Wu, S. Kwon, J. F. Driscoll, and G. M. Faeth. Turbulent Premixed Hydrogen/Air Flames at High Reynolds Numbers. *Combustion Science and Technology*, 73(1-3):327–350, sep 1990. doi: 10.1080/00102209008951655.

[141] R. Yadav, A. De, and S. Jain. A Hybrid Flamelet Generated Manifold Model for Modeling Partially Premixed Turbulent Combustion Flames. In *Volume 4B: Combustion, Fuels and Emissions*, page V04BT04A065. ASME, jun 2017. ISBN 978-0-7918-5085-5. doi: 10.1115/GT2017-65030.

[142] H. Yamashita, G. Kushida, and T. Takeno. A Numerical Study of the Transition of Jet Diffusion Flames. *Proceedings of the Royal Society A: Mathematical, Physical and Engineering Sciences*, 431(1882):27–34, nov 1996. doi: 10.1098/rspa.1990.0132.

[143] Y. B. Zeldovich. The oxidation of nitrogen in combustion and explosions. *Acta Physicochimica U.R.S.S.*, 21:577–628, 1946.

[144] M. Zellhuber, C. Meraner, R. Kulkarni, W. Polifke, and B. Schuermans. Large Eddy Simulation of Flame Response to Transverse Acoustic Excitation in a Model Reheat Combustor. *Journal of Engineering for Gas Turbines and Power*, 135(9):091508, aug 2013. doi: 10.1115/1.4024940.

[145] Q. Zhang, D. R. Noble, and T. Lieuwen. Characterization of Fuel Composition Effects in H2/CO/CH4 Mixtures Upon Lean Blowout. *Journal of Engineering for Gas Turbines and Power*, 129(3):688, 2007. doi: 10.1115/1.2718566.

[146] Q. Zhang, D. R. Noble, S. J. Shanbhogue, and T. Lieuwen. PIV Measurements in H2/CH4 Swirling Flames under near Blowoff Conditions. 2007.

[147] Y. Zhang, Z. Huang, L. Wei, J. Zhang, and C. K. Law. Experimental and modeling study on ignition delays of lean mixtures of methane, hydrogen, oxygen, and argon at elevated pressures. *Combustion and Flame*, 159(3): 918–931, mar 2012. doi: 10.1016/j.combustflame.2011.09.010.

[148] V. Zimont, W. Polifke, M. Bettelini, and W. Weisenstein. An Efficient Computational Model for Premixed Turbulent Combustion at High Reynolds Numbers Based on a Turbulent Flame Speed Closure. *Journal of Engineering for Gas Turbines and Power*, 120(3):526, 1998. doi: 10.1115/1.2818178.

[149] B. Zoller, J. Allegrini, U. Maas, and P. Jenny. PDF model for NO calculations with radiation and consistent NOâĂŞNO2 chemistry in non-premixed turbulent flames. *Combustion and Flame*, 158(8):1591–1601, aug 2011. doi: 10.1016/j.combustflame.2010.12.026.

Paper I

Cold flow characteristics of a novel bluff body hydrogen burner

Christoph Meraner, Tian Li, Mario Ditaranto, Terese Løvås

International Journal of Hydrogen Energy 2018;43:715568.

doi:10.1016/j.ijhydene.2018.02.062

INTERNATIONAL JOURNAL OF HYDROGEN ENERGY 43 (2018) 7155–7168

Available online at www.sciencedirect.com
ScienceDirect
journal homepage: www.elsevier.com/locate/he

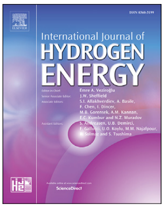

Cold flow characteristics of a novel bluff body hydrogen burner

Christoph Meraner [a,*], *Tian Li* [a], *Mario Ditaranto* [b], *Terese Løvås* [a]

[a] *Department of Energy and Process Engineering, Faculty of Engineering, NTNU, Norwegian University of Science and Technology, Trondheim, Norway*
[b] *SINTEF Energy Research, Trondheim, Norway*

ARTICLE INFO

Article history:
Received 10 November 2017
Received in revised form
23 January 2018
Accepted 12 February 2018
Available online 8 March 2018

Keywords:
Bluff body flow
Low NO_x burner
CFD simulations
Turbulence modelling
Stress-blended eddy simulation
Conical wall jet

ABSTRACT

The cold flow characteristics of a novel partial premixed bluff body (PPBB) low NO_x burner, capable of operating with hydrogen as well as methane-hydrogen blends, were investigated numerically. The PPBB burner features a frustum shaped conical bluff body generating a flame stabilizing recirculation zone. Fuel is partially premixed via jets in an accelerating cross-flow. Steady-state and transient non-reacting simulations using five different turbulence models, i.e. standard k-ε, realizable k-ε, shear stress transport (SST) k-ω, stress-blended eddy simulation (SBES) and large eddy simulation (LES), were conducted. The simulations were validated against particle image velocimetry (PIV) measurements of an unconfined non-reacting flow. All turbulent models were able to predict the recirculation zone length in good agreement with the experimental data. However, only scale resolving simulations could reproduce velocity magnitudes with sufficient accuracy. Time averaged and instantaneous results from the scale resolving simulation were analysed in order to investigate flow characteristics that are special about the PPBB burner design and of relevance for the combustion process. Two different burner configurations were studied and their effects on the flow field were examined. The recirculation zone volume as well as the entrainment into the wall jet around the bluff body were found to correlate with the elevation of the bluff body relative to the burner throat. Both of these parameters are expected to have a strong impact on the overall NO_x emission, since the near burner region is typically one of the main contributors to the NO_x formation.

Introduction

Combustion of hydrogen and hydrogen-rich synthetic gaseous fuels, such as syngas have received increased attention in the context of climate change and the urgent need for alternative fuels [1–3]. The use of syngas is particularly attractive when obtained by gasification of coal, waste or CO_2-neutral biomass feedstock. In case of steam gasification, it is possible to combine the process with a subsequent water-gas shift reaction, in which CO and H_2O are converted to H_2 and CO_2. The CO_2 can then be captured and stored. This combined process is referred to as pre-combustion carbon capture and storage (CCS). Benefits of pre-combustion CCS are the maximisation of the hydrogen level and the high relative concentration of the carbon species as CO_2 [4,5]. Although the combustion of hydrogen in air emits theoretically only water, the high reactivity and elevated combustion temperature

---

[*] *Corresponding author.*
E-mail address: christoph.meraner@ntnu.no (C. Meraner).

https://doi.org/10.1016/j.ijhydene.2018.02.062

generate harmful and regulated nitrogen oxides (NO_x), that to date, no commercial burner can mitigate easily. Hence, transitioning from natural gas to hydrogen and hydrogen-rich combustion comprises a trade-off between reduced CO_2 emissions and increased NO_x emissions. In order to mitigate this undesired effect, low NO_x combustion concepts need to be developed, while keeping the required fuel flexibility in mind.

Different techniques have been established in the industry to reduce NO_x emissions from combustion processes. They can be categorized into four groups: pre-treatment, combustion modification, process modification (such as the modification of a gas turbine cycle [7]) and post-treatment [8]. A key benefit of syngas is its wide flexibility in fuel sources [9]. However, this and in particular different processing techniques imply a significant variation in relative composition of syngas [10,11], which makes pre-treatment challenging. Most post-treatment methods on the other hand are relatively simple to implement, but they represent expensive add-on costs and are not benefiting the combustion process in any way [8]. The U.S. Environmental Protection Agency (EPA) provides an overview on the total effective NO_x reduction and the cost effectiveness of different control techniques [12]. The report concludes that low NO_x and ultra low NO_x burner on its own have the best cost effectiveness. While the lowest NO_x levels are achieved by a combination of low NO_x burners and selective catalytic reduction (SCR). Hence, there is a strong incentive to develop low NO_x burners for both standalone as well as combined applications.

Low NO_x burners can utilize different design features to minimize NO_x emissions. A discussion on several of these designs can for example be found in previous studies [1,10]. However, for the development of low NO_x burners that can cope with variable fuel compositions and potentially high hydrogen concentration special care needs to be taken, especially of combustion stability. Hydrogen has a unique impact on the behaviour of fuel mixtures due to its significantly different transport properties and flame speed compared to other gaseous fuels [13]. Several studies have investigated the non-linear dependence of flame properties (e.g. flashback and lean blowout) on the hydrogen concentration [14–16]. Due to the wider flammability limits, low levels of hydrogen can extend the lean stability limits of burners [17]. However, higher levels of hydrogen decrease the stability range, as a result of the increased probability of flashbacks [14].

One of the most common designs for low NO_x gas burners is the premixed swirl burner. However, such burners are particularly prone to flashbacks at elevated hydrogen concentrations [18]. This is attributed to the premixing as well as the potential for combustion induced vortex breakdown (CIVB), which is related to the interaction of heat release and swirling flows [10,19,20]. In order to avoid these issues associated with premixed swirl burners, Spangelo et al. [21] developed and patented a novel partially premixed bluff body burner (PPBB burner) that aims to ensure stable combustion with low NO_x emissions across a wide range of hydrogen concentrations. The PPBB burner combines advanced mixing techniques with burner generated internal flue gas recirculation (IFGR), which is sometimes referred to as furnace gas recirculation. A more detailed description of the PPBB burner design features is given in section the PPBB burner.

The PPBB burner has been investigated experimentally by Dutka et al. and has proven good emission performance at laboratory scale [22,23]. However, the scalability of the system is not yet well understood. For a successful scaling of the burner to larger dimensions and practical applications it is necessary to obtain a deeper understanding of the burner flow characteristics and their changes at different scales. The conducted experimental campaigns have been limited to the analysis of the flow field in a defined 2D observation window downstream of the bluff body as well as global emission measurements for NO_x, O_2, CO and CO_2. One of the main objectives for the present study is therefore to extend the investigated parameters by applying computational fluid dynamic (CFD) simulations, which allow to get a broader picture of the flow characteristics. In the context of scaling the main requirement for CFD simulations is to adequately represent qualitative trends depending on the burner scale. However, simulating the entire complexity of hydrogen combustion in a challenging geometry, including chemical reactions, different species properties, radiation, etc. involves the use of several submodels in addition to solving the equations describing the turbulent flow field. Hence, it is ambiguous to quantify uncertainties attributed to individual submodels. Thus the complexity of such a simulation needs to be increased gradually. The scope of the present study was therefore limited to the modelling of the non reacting air flow, which dominates the burner aerodynamics. This approach allows a clear distinction between aerodynamic and combustion driven effects and builds a solid foundation for future investigations with increased model complexity and focus on different burner scales.

By excluding any chemical reactions from the flow it was possible to validate turbulence models without the additional uncertainty that derives from the various submodels related to combustion. Different turbulence models were employed to identify the model requirements for an adequate description of the major burner characteristics. The applied turbulence models ranged from two equation RANS models, that model the whole turbulence spectrum, to LES simulations which resolve the large scales and model only the subgrid scales. A comprehensive comparison was made between well-known models such as the standard k-ε model and a novel stress-blended eddy simulation (SBES) model, which has been recently developed by the ANSYS® turbulence team [24,25]. The SBES model represents a compromise between RANS and LES models. It resolves large scale turbulence only away from walls, while modelling the entire turbulence spectrum close to walls. A more detailed descriptions of the underlying numerics of the SBES model is provided in section Numerical methods. All conducted numerical simulations were validated against the measurements obtained by Dutka et al. [26,27].

The PPBB burner

The PPBB burner is designed for furnaces and boilers, operating at low pressure. Its main components consist of a

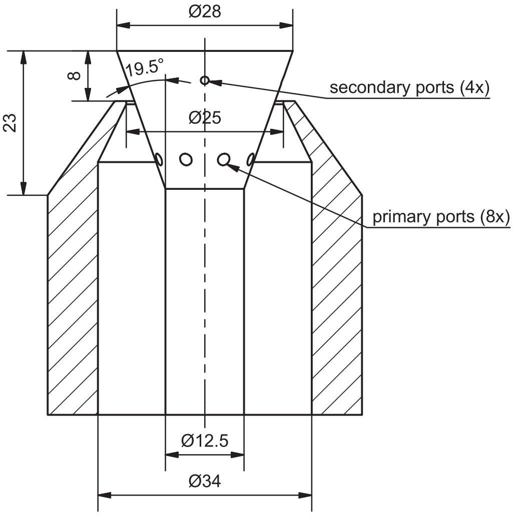

Fig. 1 – **Schematic of the PPBB burner (dimensions in mm).**

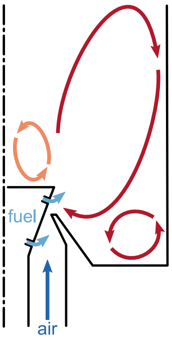

Fig. 2 – **Illustration of the PPBB burner flow pattern. Primary and secondary fuel ports are drawn in the same plane for illustration purpose.**

cylindrical lance, holding a conical frustum shaped bluff body mounted concentrically, within a cylindrical housing (see Fig. 1). The bluff buddy is partially retracted into the housing forming a converging segment in which the narrowest cross-section is referred to as burner throat. The bluff body holds eight primary fuel ports located upstream of the throat and four secondary fuel ports downstream of the throat. Note that the secondary fuel ports are offset from the primary fuel ports in tangential direction (i.e., they are located ”between” primary fuel ports). The laboratory scale burner operates at a nominal thermal load of 10 kW.

Fig. 2 illustrates the flow pattern generated by the PPBB burner. Air is provided through the annular duct formed by the lance and burner housing. The majority of fuel (70% of the total fuel mass flow) is provided through the primary fuel ports, located in the converging section of the burner, where it is mixed in the accelerating cross flow. This configuration allows for rapid mixing and avoids ignitable unburned mixture in low axial velocity regions, which potentially could lead to flashback in the core flow, a well known phenomena as described by Plee and Mellor [28]. Furthermore, the accelerating flow ensures thin boundary layers, preventing flame back propagation within the boundary layer itself. Flashback in the boundary layer has been extensively studied for conventional fuels such as pure methane [29–31] and more recently also for syngas with different hydrogen concentrations [32–34]. Lieuwen et al. [10] concludes: “Keeping the boundary layers as thin as possible is an essential design criterion for syngas burners [...]”.

The remaining 30% fuel mass flow is provided trough the secondary fuel ports downstream of the throat, which creates small regions of enriched mixture downstream of the bluff body trailing edge. Dutka et al. [26] investigated the effect of different secondary fuel fractions on flame stability and NO_x emissions. The study showed that the impact of secondary fuel on the burner performance is correlating strongly to the hydrogen concentration in the fuel as well as the lance height (i.e., elevation of the bluff body trailing edge in relation to the throat). The burner configurations assessed in the present study (i.e., 8 mm and 16 mm lance height) have been found to provide optimal emission performance for the PPBB burner operating with pure hydrogen and pure methane respectively [26].

Bluff body flame stabilization has been studied extensively, even though it is less common than swirl flame stabilization. Recent studies of conical bluff body stabilized flames have been conducted by Kariuki et al. [35,36] (unconfined), Andreini et al. [37] (confined) and Dawson et al. [38] (confined and unconfined). A unique feature of the PPBB burner is, however, the elevated position of the bluff body with regards to the burner throat (see Fig. 1). Since the bluff body is not fully immersed, it is possible to realize a minimum housing diameter that is smaller than the bluff body diameter itself. This leads to a blockage ratio larger than 100%, where the blockage ratio is defined as the ratio of bluff body cross section to minimum housing cross section. The PPBB can therefore by characterized by a conical wall jet flow around the bluff body. Only limited studies have investigated conical wall jets [39–41]. Research activities are mainly focusing on plane, radial or cylindrical wall jets. The latter two can be seen as limiting cases of a conical wall jet for a half-angle of 90° and 0° respectively. The plane wall jet is in turn the limiting case for a cylindrical wall jet with infinite large radius. Sharma [39] found that the spread angle as well as the shape of the velocity profiles are independent of the cone half-angle. The decrease of the maximal jet velocity in flow direction is on the other hand depending on the half-angle. The velocity decreases faster with an increased half-angle.

The elevated lance position is a crucial and unique feature of the PPBB burner for NO_x emission control and fuel flexibility. It allows entrainment of internal recirculated flue gas into the conical wall jet upstream of the flame anchor point (see Fig. 2). Recirculation of flue gas internally increases the overall efficiency compared to external flue gas recirculation. Understanding and controlling the amount of recirculated flue gas is therefore highly important.

Numerical methods

The PPBB burner was simulated using steady-state Reynolds averaged (RANS) as well as transient scale resolving simulations employing ANSYS® Academic Fluent, Release 18.1. All simulations were based on the assumption of incompressible flow. The density was calculated based on the incompressible ideal gas law based on the operational pressure (i.e., atmospheric pressure for the PPBB burner). The highest velocities in the PPBB burner (realized in the burner throat) are significant lower then the speed of sound in air (i.e., Ma ~ 0.15) which justifies this assumption. Gravitational forces were neglected.

The governing equations for the conservation of mass and momentum as well as the transport equations for the respective turbulence model were discretised based on the finite volume method. A second order upwind scheme [42] was used to discretise the convective terms of the RANS transport equations and a less dissipative bounded central difference scheme [43] was used for the scale resolving simulations. The diffusive terms were discretised with a second order central difference scheme. The transient simulations were realized by use of a bounded second order implicit scheme. The SIMPLEC algorithm [44] was applied for the pressure-velocity coupling in all steady state simulations while a fractional-step method (FSM) [45–48] in conjunction with a non-iterative time advancement (NITA) was used for all transient simulations. The transport equations were solved using a point implicit (Gauss-Seidel) linear equation solver in conjunction with an algebraic multigrid method [50]. ANSYS® Academic Fluent, Release 18.1. employs a co-located scheme (i.e., pressure and velocity are both stored at the cell centres) which requires a pressure interpolation scheme to retrieve the pressure at the cell faces. A second order central difference scheme was used for the pressure interpolation. Gradients and derivatives were evaluated employing a cell-based method (i.e., least squares cell based gradient evaluation), solving the coefficient matrix by use of the Gram-Schmidt process [51].

All transient simulations were conducted on the full domain as shown in Fig. 3. Different domain sizes were tested to ensure that the boundaries were located sufficiently far from the burner. A quarter of the domain was used for all RANS simulations, such that only two primary and one secondary fuel port were included in the domain. The RANS simulations were realised using periodic boundary conditions (see Fig. 3b). The applied boundary conditions are shown in Fig. 3. A constant velocity, normal to the boundary, of 4.0 m/s for the 8 mm lance height and 4.2 m/s for the 16 mm lance height configuration was imposed at the velocity inlet, corresponding to the experimental setup [26]. The turbulence kinetic energy at the velocity inlet was calculated based on the turbulence intensity which was assumed to be 5% and a hydraulic diameter of 4 mm (corresponding to the largest hole diameter in the perforated plate used to stabilize the flow, see Fig. 3.2 b in Ref. [52]) was used to estimate the corresponding turbulence dissipation rate. Atmospheric pressure was imposed at all open boundaries together with a turbulent intensity of 5% and a turbulent viscosity ratio of 10 which were used to calculate the corresponding turbulence kinetic energy and dissipation rate. Flow entering the domain at the pressure outlet or flow leaving the domain at the pressure inlet was defined as backflow. The direction of the backflow was set to be normal to the boundary for both of the pressure boundaries. A sensitivity study with varying turbulent boundary conditions showed negligible effect on the main flow features.

Five different turbulence modelling approaches, i.e. standard k-ε [53], realizable k-ε [54], SST k-ω [55], SBES [24,25] and LES with the WALE subgrid model [56], were investigated. All RANS models were applied in steady state as well as unsteady (URANS) mode. The LES simulations have been performed on the same numerical grid as the SBES simulations, hence under resolving the wall boundary layers. The SBES model represents a new paradigm of turbulence modelling. A further description of the model is therefore provided in the following paragraph. Descriptions of the other turbulence models can be found in the corresponding literature.

The SBES model is a RANS-LES hybrid model capable of switching rapidly from an underlying RANS model to an algebraic LES model. The SBES formulation is based on the shielded detached eddy simulation (SDES) model, which aims to prevent grid-induced separation (one of the main shortcomings of detached eddy simulation models) by introducing an asymptotic shielding function, f_s and an alternative grid scale. The strong shielding of f_s allows the SBES formulation to blend existing RANS and LES models on the stress-level:

$$\tau_{ij}^{SBES} = f_s \cdot \tau_{ij}^{RANS} + (1 - f_s) \cdot \tau_{ij}^{LES} \tag{1}$$

where τ_{ij}^{RANS} is the RANS part and τ_{ij}^{LES} the LES part of the modelled stress tensor. If both, the RANS and the LES model, are eddy-viscosity models the formulation simplifies to:

$$\nu_t^{SBES} = f_s \cdot \nu_t^{RANS} + (1 - f_s) \cdot \nu_t^{LES}. \tag{2}$$

The SBES formulation is in this sense not a new turbulence model, but rather a novel way to blend two existing models. This approach allows therefore to combine different RANS and LES models. The SBES model has, to the authors knowledge, not yet been employed for studying advanced burner configurations such as the PPBB burner. The SBES simulations of the PPBB burner were conducted by blending the SST-k-ω model in the RANS region with the WALE subgrid model in the LES region.

The PPBB burner represents a complex geometry due to the arrangement of its several fuel ports. It is challenging to represent such a geometry with a structured hexahedral mesh. Several alternative mesh topologies (i.e., tetrahedral, polyhedral, cut-cell and tetrahedral/hexahedral hybrid mesh) were tested in this study. Hybrid meshes utilize the flexibility of unstructured meshes in complex areas of the fluid domain while maintaining the higher accuracy of structured hexahedral meshes in simpler regions. However, they are not as easily generated as fully unstructured meshes and extra attention has to be given to the transition region between different mesh topologies (i.e., from tetrahedral/polyhedral to hexahedral cells). Hybrid meshes are therefore not ideal for the future up scaling of the PPBB burner, which will require the generation of multiple different meshes. Cut-cell meshes on the other hand can be generated using highly automated algorithms. They are characterized by predominantly high

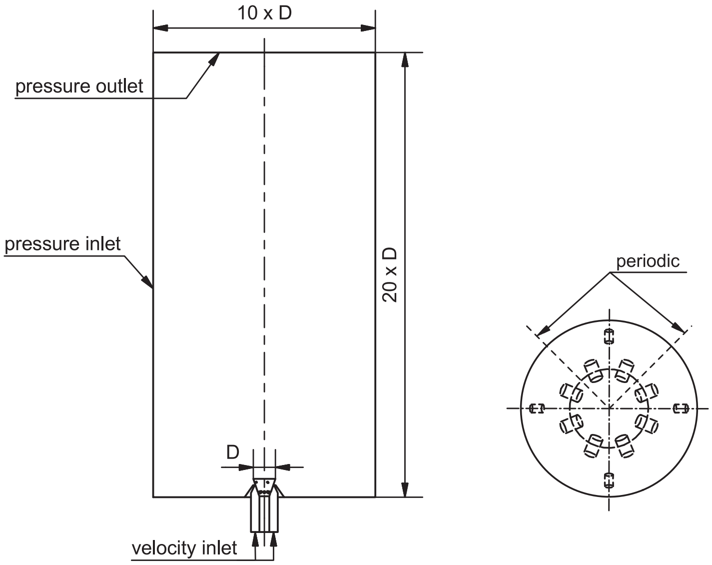

(a) Side view of the computational domain at 8 mm lance height.

(b) Top view of the burner lance indicating the location of the periodic boundaries (dashed lines).

Fig. 3 – Dimensions of the computational domain and boundary conditions. All unspecified boundaries are set to no-slip wall.

quality hexahedral cells. However, this comes at the cost of a few cells adjacent to the geometry with very high skewness. These low quality cells led to slow convergence of the PPBB burner simulations. Both tetrahedral and polyhedral meshes show a more uniformly distributed mesh quality and can easily adapt to complex geometry. Polyhedral meshes achieve the same accuracy as tetrahedral meshes at lower computational costs since they typically result in a significant lower total cell count than tetrahedral meshes. An unstructured polyhedral mesh with prism inflation layers at the walls was therefore found to be the most suited mesh topology for simulating the PPBB burner (see Fig. 4).

The mesh resolution was optimized for various flow regions by prescribing a size field (i.e., location specific maximum cell sizes). An example of such a size field can be seen in Fig. 5. A better representation of the transition between different cell size regions can be seen in Fig. 4. The growth rate in cell size was restricted to a maximum of 10% to ensure smooth transitions. However, initial scale resolving simulations indicated that the relatively narrow refinement shown in Fig. 5 had a noticeable effect on the flow field for the 8 mm lance height simulation. The refinement of the free shear layer and recirculation zone was therefore extended to a cylindrical region with a diameter of approximately two bluff body diameters and a height of 1.5 bluff body diameters for the scale resolving simulation of the 8 mm lance height. Mesh sensitivity simulations with different cell counts ranging from 2.9 M to 8.2 M cells were conducted. The final scale resolving simulations were realised with 4.0 M cells for the 16 mm configuration and 5.2 M cells for the 8 mm configuration. Boundary layer regions were resolved with values for the dimensionless wall distance (y^+) close to unity. The warped-face gradient correction was employed to improve gradient accuracy for non planar cell faces.

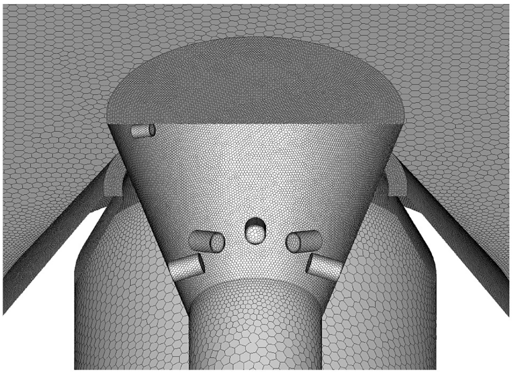

Fig. 4 – Half section view of the polyhedral surface mesh.

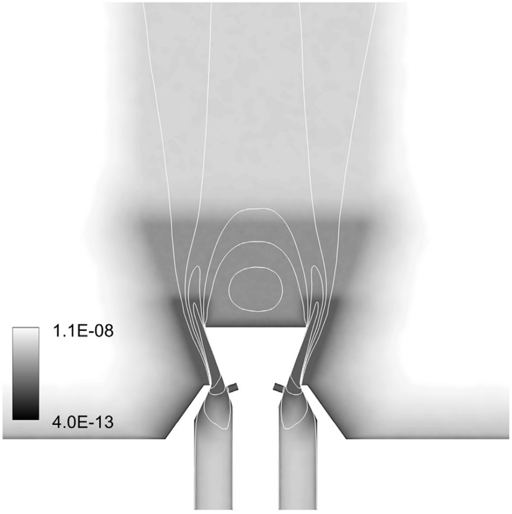

Fig. 5 – Cell volume with overlaid mean axial velocity isolines from the scale resolving 16 mm lance height simulation. Note an exponential colour scale is used for better readability.

Results

The results of the CFD based analysis are presented in three sections: Reynolds averaged simulations, scale resolving simulations and the effect of different lance configurations. The first two sections are dealing with the validation of the applied CFD models, while the last one focuses on the alteration of the PPBB burner operational mode and its effect on the flow field characteristics, especially in regions that have not been accessible to PIV measurements.

Reynolds averaged simulations

Axial velocity profiles along the burner centreline were obtained from RANS and URANS simulations using different turbulence models. A comparison of these profiles to PIV data acquired by Dutka et al. [26] is shown in Fig. 6a and Fig. 6b respectively. All RANS simulations were able to predict the recirculation zone length. However, none of the applied models were capable to capture the velocity magnitudes of the flow field with a reasonable accuracy. All models were showing the same trend of over predicting velocities, especially within the recirculation zone. The SST k-ω model deviates most from the experimental data as seen in Fig. 6a. However, it performed better than the k-ε models in capturing the velocity decay in the developed jet region downstream of the recirculation zone. Neither the standard, nor the realizable k-ε model predicted the velocity decay correctly. The standard k-ε model was the only model that captured the maximal axial velocity downstream of the recirculation zone.

All three turbulence models were tested in URANS mode. The flow variables were, depending on individual simulations, sampled over a time period of 1.5–2 s, after an initial build-up time of 0.2–0.5 s. The resulting time averaged axial velocity profiles along the burner centreline are shown in Fig. 6b. Switching to URANS mode did improve the performance of the SST k-ω model considerably. Both k-ε models performed comparable to the RANS simulations, with a slight improvement of the realizable k-ε model. The high dissipation of the standard k-ε model prohibited the development of unsteady flow structures.

The normalized recirculating mass flow rate is given in Table 1, along with the normalized dimensions of the recirculation zone. Typically the recirculating mass flow rate is normalized by the mass flow rate at the trailing edge of the bluff body as suggested by Taylor and Whitelaw [57]. Since this region was not captured by the PIV measurement, the inlet mass flow was used to normalize the recirculating mass flow rate. The recirculating mass flow rate measured by PIV was

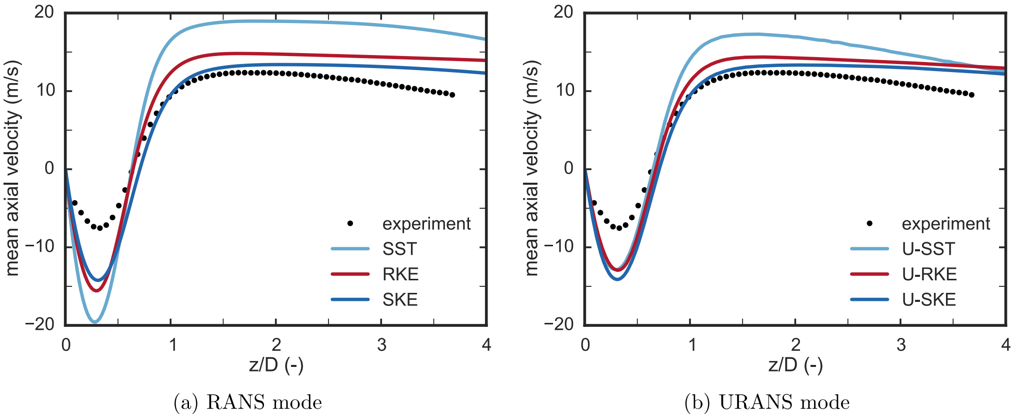

Fig. 6 – Mean axial velocity along the burner centreline for 8 mm lance height. Solid lines: standard k-ε (SKE), realizable k-ε (RKE) and SST k-ω (SST) simulations; dots: PIV measurement. Spacial coordinates are normalized by the bluff body diameter (D).

Table 1 – Recirculation zone length (*L*) and width (*W*) normalized by the bluff body diameter (*D*) and normalized recirculation mass flow rate $\left(\frac{\dot{m}_r}{\dot{m}}\right)$ predicted by the two equation turbulence models.

		$\frac{L}{D}$ (–)	$\frac{W}{D}$ (–)	$\frac{\dot{m}_r}{\dot{m}}$ (–)
Experiment		0.64	0.70	0.36
RANS	SST k-ω	0.63	0.75	1.26
	Realizable k-ε	0.64	0.75	1.15
	Standard k-ε	0.71	0.74	1.12
URANS	SST k-ω	0.65	0.80	0.82
	Realizable k-ε	0.67	0.80	1.08
	Standard k-ε	0.71	0.78	0.97

estimated based on the numerical integration of the axial velocity profile along the radius at the centre of the recirculation zone.[1] All applied turbulence models were able to reproduce the recirculation zone dimensions. However, they severely over predicted the recirculating mass flow rate. The SST k-ω model in URANS mode led to the best results, but still over predicted the recirculating mass flow rate by a factor of 2–3.

Scale resolving simulations

An accurate description of velocity magnitudes and hence residence time and recirculating mass flow rate in the recirculation zone is crucial for assessing combustion emissions. Scale resolved simulations were conducted, as the investigated RANS turbulence models performed poorly in this regard. The complex geometry of the PPBB burner, especially in hydrogen configuration (i.e., lance height of 8 mm) with large velocities in the narrow (1.32 mm) throat, is computational demanding for scale resolving simulations. The burner was therefore initially simulated in methane configuration (i.e., lance height of 16 mm). This configuration allowed a finer spatial and temporal resolution at lower numerical costs due to the wider throat opening and lower flow velocities. Moreover, the variation of the lance height made a qualitative assessment of its impact on the flow field accessible. The effect of varying the lance height on the flow field (i.e., change of air entrainment and recirculation zone length) is expected to be similar in the non-reacting and reacting flow configuration, even though absolute values will be different for these two scenarios. Experimental observations made by Dutka et al. [26] support this assumption.

Lance height 16 mm

Fig. 7a shows the comparison of the mean axial velocity measured experimentally (left) and the mean axial velocity simulated using the SBES turbulence model (right). The velocity field of the SBES simulations was in good agreement with the PIV measurements. The simulation displayed slightly lower velocities in the centre of the flow and higher velocities in the shear layer flow. Note that the velocity field measured by PIV appears distorted close to the boarders of the contour plot. This is attributed to the limited number neighbouring interrogation windows at the boarders. The symmetry axis of the measured flow field is furthermore tilted by approximately 4° (see Fig. 7b). This was likely related to the difficulty of achieving perfect symmetry in an experimental set-up. Asymmetry can be caused by uneven air supply or centring inaccuracies of the lance. Small deviations in the alignment of lance and housing axis have a strong influence on the symmetry of the throat width due to the relatively large distance between the lance mounting point and the throat. Besides, flow fields with recirculation are inherently hydrodynamically unstable.

Fig. 8 shows the instantaneous visualisation of the iso-surface of the Q-criterion (which defines turbulent eddies as regions where the irrotational straining is small compared to the vorticity [58]) coloured by the SBES blending function. It can bee seen that the SBES model was able to shift quickly to LES mode (blue) outside the wall boundaries while structures close to the wall are in RANS mode (red). The model resolved small three-dimensional turbulent structures, which are visible in the recirculation zone.

In Fig. 9 the velocity was corrected for the tilt of the flow field. The dots show the velocity along the symmetry axis of the flow, while the diamonds show the uncorrected velocity along the centreline of the burner. It is not possible to identify or correct for tilting of the flow field outside of the 2D plane covered by the PIV measurement. Hence, the observed tilt in the xz-plane is indicating the failure margin that can be expected for alignment deviations in the experimental set-up. However, the impact of it is less noticeable closer to the bluff body and can be neglected within the recirculation zone. The SBES and LES simulations, using the WALE subgrid model, showed almost identical results along the burner centreline (see Fig. 9). Both were in good agreement with the experimental data. The velocity magnitude were slightly under predicted by both modelling approaches. The difference between measured and simulated recirculating mass flow rate as well as recirculation zone length were below 10% for both simulations (see Table 2).

Lance height 8 mm

The measured flow field for 8 mm lance height did not display the same tilted symmetry axis as previous seen for the 16 mm lance height case (see Fig. 10b left), even though some asymmetry attributed to the experimental set up was still apparent. Comparing instantaneous flow fields from PIV and SBES simulations (see Fig. 10a) shows the higher resolution in the CFD simulation which allows to visualize smaller turbulent structures. The SBES simulation and the LES simulation, using the WALE subgrid model, produced very similar results. Fig. 11 shows a comparison between these two models and experimental data as well as data from the SST k-ω model in URANS mode. The scale resolving simulation were able to capture the recirculation zone length as well as the velocity decay in the developed jet region reasonable well. The velocity magnitude were over predicted by the scale resolving simulations and the shape of the recirculation zone appeared not as spherical as in the PIV measurements. This was also reflected in the recirculating mass flow rate, which was significantly over predicted by the scale resolving simulations (see Table 3).

---

[1] The centre of the recirculation zone was defined by the axial coordinate of the highest recirculation velocity on the burner centreline.

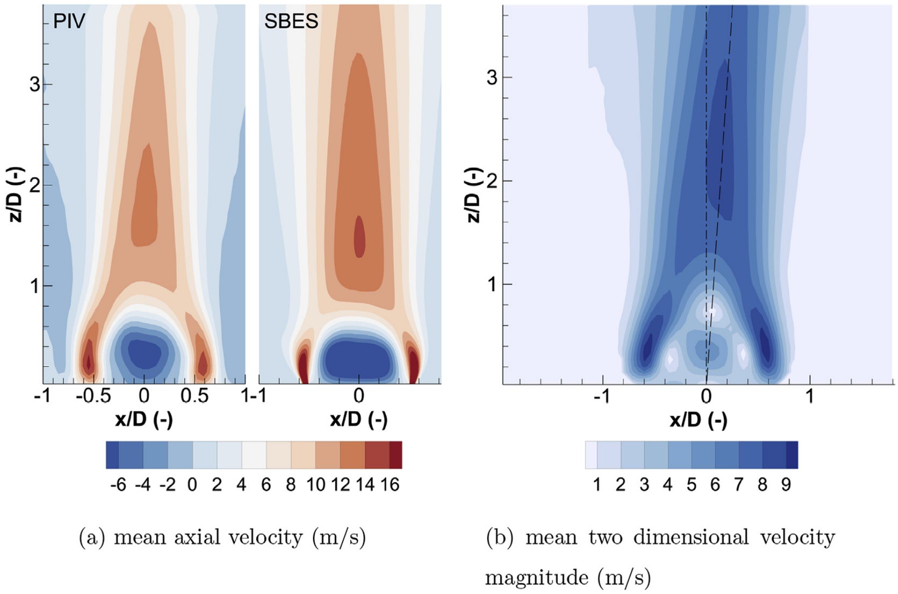

(a) mean axial velocity (m/s)

(b) mean two dimensional velocity magnitude (m/s)

Fig. 7 – a) Mean axial velocity from PIV measurement (left) and SBES simulation (right). b) Measured two dimensional mean velocity magnitude. The flow symmetry axis (dashed line) is tilted by ~4° from the burner centreline (dash doted).

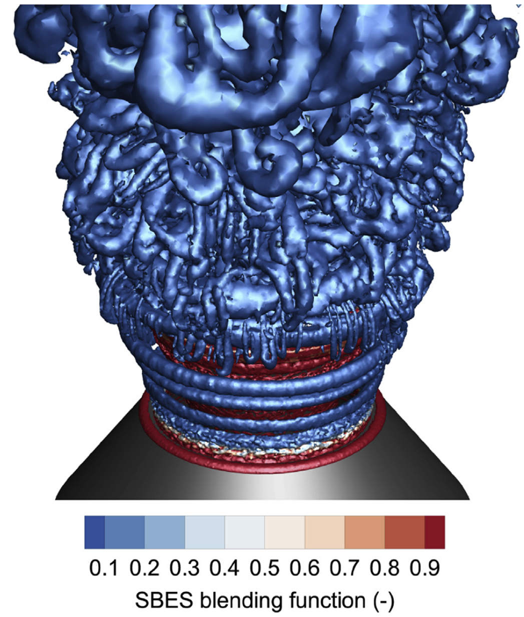

Fig. 8 – Q-criterion (10^4 s^{-2}) iso-surface coloured by the SBES blending function (where a value of 1 means RANS and a value of 0 means LES mode) from the 16 mm lance height simulation.

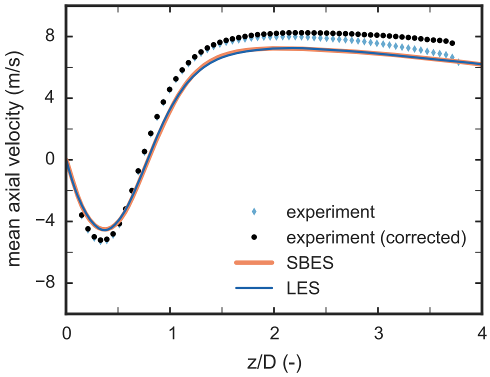

Fig. 9 – Mean axial velocity at 16 mm lance height. Bold red line: SBES simulation; blue line: LES simulation; diamonds: PIV measurement along burner centreline; dots: PIV measurement adjusted for ~4° tilt of the mean flow field (see Fig. 7b). (For interpretation of the references to color/colour in this figure legend, the reader is referred to the Web version of this article.)

Effect of different lance configurations

Varying the lance height to adapt the PPBB burner to different fuel compositions affects the opening of the throat, the length of the wall jet region and the relative position of the fuel ports to the housing which leads to a different momentum ratio of

Table 2 – Size of recirculation zone and recirculation mass flow rate for 16 mm lance height.

	$\frac{L}{D}$ (−)	$\frac{W}{D}$ (−)	$\frac{\dot{m}_r}{\dot{m}}$ (−)
PIV	0.73	0.71	0.26
SBES	0.79	0.81	0.28
LES	0.78	0.86	0.27

the jet in cross flow configuration of the fuel injection. Extending the lance height increases the length of the recirculation zone and decreases the recirculating mass flow rate. This effect was observed in both the experiments and scale resolving simulations. The smaller throat opening of the 8 mm configuration led to higher velocities in the free shear layer downstream of the bluff body even thought the air mass flow rate was slightly lower than that for the 16 mm configuration (see Fig. 12). The simulation of the 16 mm configuration under predicted the shear layer spread compared to the experimental data more than the simulation of the 8 mm configuration. However, the centre region of the flow was better reproduced in the 16 mm simulation.

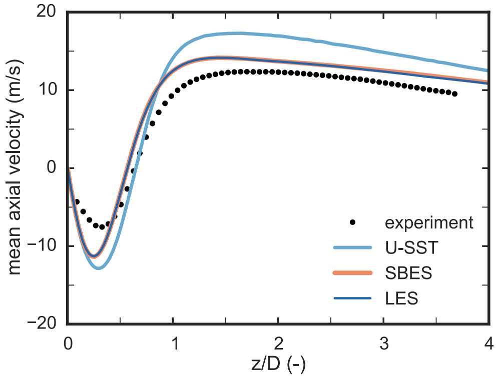

Fig. 11 – Mean axial velocity at 8 mm lance height. Light blue line: URANS SST k-ω simulation; bold red line: SBES simulation; thin dark blue line: LES simulation; dots: PIV measurement. (For interpretation of the references to color/colour in this figure legend, the reader is referred to the Web version of this article.)

Table 3 – Size of recirculation zone and recirculation mass flow rate for 8 mm lance height.

	$\frac{L}{D}$ (−)	$\frac{W}{D}$ (−)	$\frac{\dot{m}_r}{\dot{m}}$ (−)
PIV	0.64	0.70	0.36
SBES	0.57	0.80	1.56
LES	0.57	0.80	1.35

The region close to the bluff body wall was not accessible by the conducted PIV measurements. Time averaged data of the wall jet was therefore obtained from the LES simulations for 8 mm and 16 mm lance height to give new insight into the flow structure in this region. Fig. 13 shows a set of normalized velocity profiles close to the wall at various positions in flow direction between throat and bluff body trailing edge. The velocity is decomposed into a component parallel to the wall (u_w) and a component perpendicular to the wall (v_w). The velocity is normalized by the maximum velocity in flow direction (u_{max}) and the wall coordinate (y_w) is normalized by the wall jet half-width ($y_{1/2}$) which is the cross-stream distance corresponding to half of the maximum velocity. The coordinate in flow direction (x_w) is normalized by minimum throat width (δ_{throat}). The velocity in the throat ($x_w/\delta_{throat} = 0$) contains a noticeable velocity component towards the bluff body wall caused by the converging burner housing. This component decays in flow

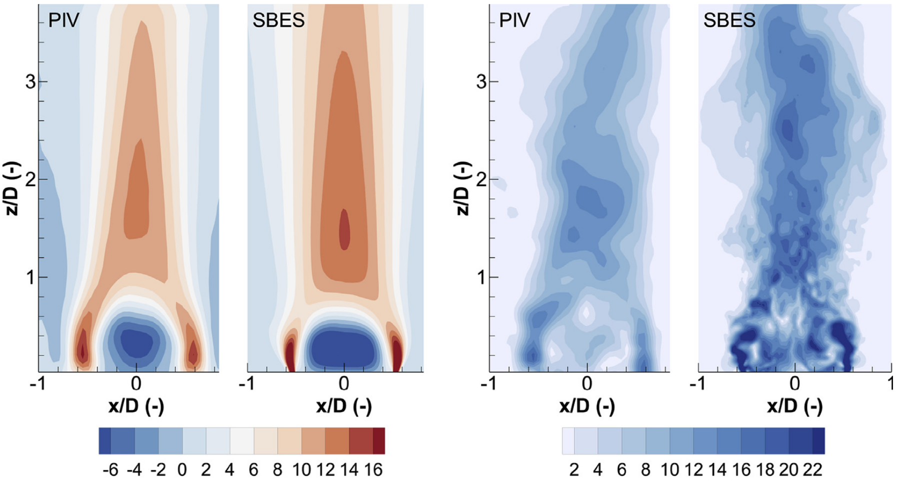

(a) mean axial velocity (m/s)

(b) instantaneous two dimensional velocity magnitude (m/s)

Fig. 10 – Comparison of mean and instantaneous velocity fields from PIV (left in the sub-figures) and SBES simulation (right in the sub-figures).

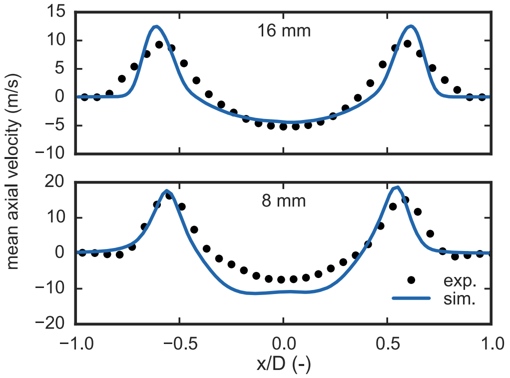

Fig. 12 – **Axial velocity profile along the burner x-axis obtained from PIV (dots) and LES simulations (solid line) at 0.3 bluff body diameters downstream of the bluff body trailing edge.**

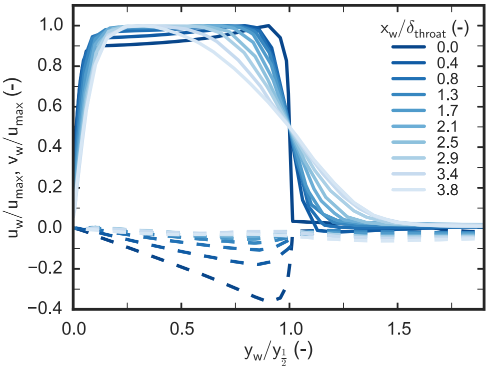

Fig. 13 – **Normalized velocity profiles in the wall jet region obtained from LES simulations of 16 mm lance height. (solid lines) velocity component parallel to wall, (dashed lines) velocity component perpendicular to the wall.**

direction. However, the velocity profiles do not reach self-similarity. A similar trend can be seen in Fig. 14a for the simulation of 8 mm lance height. However, at $x_w/\delta_{throat} = 3.1$ the profiles start to collapse in the outer layer as seen in Fig. 14b.

The wall jet velocity and width at the bluff body trailing edge are important as they affect the recirculation zone. Fig. 15 shows the decay of the maximum jet velocity and the jet spreading rate represented by the variation of the half-width $y_{1/2}$. Increasing the lance height increases the throat opening as well. The normalized length of the wall jet in flow direction is therefore shorter for the 16 mm configuration compared to the 8 mm configuration. The jet half-width decreases for both lance heights initially and starts to increase again at $x_w/\delta_{throat} = 3$. The decay of the maximum velocity in flow direction shows an opposite trend. The difference of the velocity profiles between the two burner configurations is, however, not found to be as significant as the difference in the spreading rate.

Discussion

The discussion is structured in three sections. Section turbulence model requirement and section near wall treatment discuss the requirements to the turbulence model. The latter one focuses on the two scale resolving turbulence models and their different near wall approaches only. Section PPBB burner flow characteristics discusses the effect of different lance heights on the flow field, focusing mainly on regions that are likely to have a strong impact on the NO_x formation in a reacting flow. The lance height is one of the main burner parameters and its variation will affect the non-reacting and reacting configuration in a similar matter [26], which allows to draw qualitative conclusions based on the simulation of the non-reacting flow configuration.

Turbulence model requirement

All conducted RANS and URANS simulations over predicted the velocity magnitude compared to the experimental data obtained from PIV measurements. The high velocities in both the bluff body wake and recirculation zone are a consequence of the over predicted velocity in the free shear layer shedding from the bluff body trailing edge. Free shear layer flows are dominated by different instability modes depending on the type of shear layer flow (i.e., mixing layers, jets and wakes) which is challenging to accurately predict with statistical averaged models using a single set of coefficients [59]. With values for the coefficients that are appropriate to boundary-layer flows these models typically predict two-dimensional flows, as for example a plane jet, quite accurately. For axisymmetric flows with recirculation, however, effects that are not existing in two dimensional flows (such as vortex stretching) occur and can lead to large errors [60,61].

This shortcoming of RANS turbulence models can be overcome by employing scale resolving simulations. Scale resolving simulations with an appropriate spatial and temporal resolution are able to describe the flow characteristics of the PPBB burner in good agreement with experimental data as it was seen in the simulation of the 16 mm lance height configuration. Furthermore it was shown that scale resolving simulation are superior to RANS/URANS simulations, even with a lower relative resolution as seen in the 8 mm lance height simulation. The difference in resolution between the 16 mm and the 8 mm simulation can be assessed by comparing the velocity profiles in Fig. 13 with the profiles given in Fig. 14. The lower resolution is furthermore leading to fluctuations of the normalized wall jet half-width shown in Fig. 15. This is, however, due to the way the half-width is obtained from a linear interpolation of the velocity profiles at the point $u_{max}/2$. Hence the resolution affects both the assessment of u_{max} as well as the linear interpolation, which magnifies the overall effect of different resolutions.

Near wall treatment

Typically it requires less effort to resolve the largest turbulence scales in free shear flows compared to wall boundary layers, where the turbulence length scale is very small

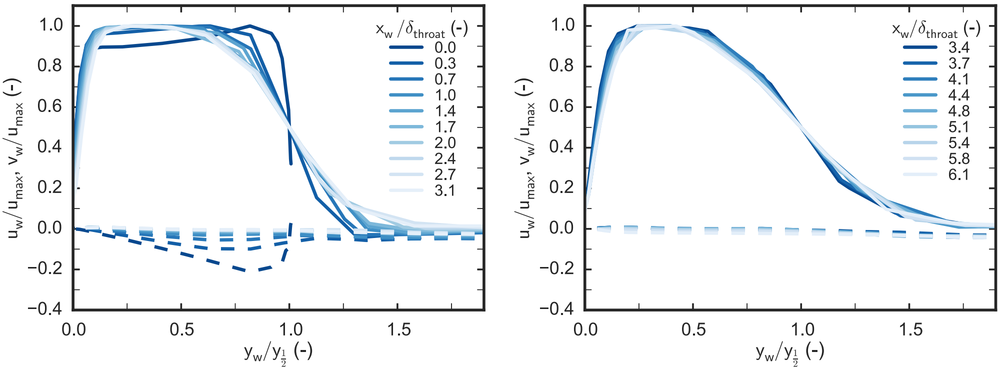

(a) upstream x_w/δ_{throat}=3.1 (b) downstream x_w/δ_{throat}=3.1

Fig. 14 – Normalized velocity profiles in the wall jet region obtained from LES simulations of 8 mm lance height. (solid lines) velocity component parallel to wall, (dashed lines) velocity component perpendicular to the wall.

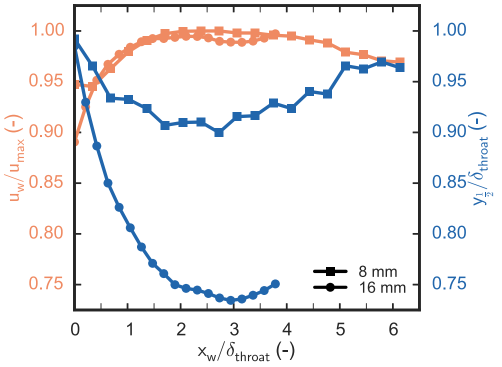

Fig. 15 – Decay of the maximum velocity (orange) and jet spreading rate (blue) for 8 mm lance height (squares) and 16 mm lance height (dots). (For interpretation of the references to color/colour in this figure legend, the reader is referred to the Web version of this article.)

compared to the boundary layer thickness. Applying LES models with under resolved wall boundary layers can, depending on the flow configuration, led to worse results than employing a suitable RANS model [24]. This motivated the development of hybrid models, such as the SBES model, where large eddies are only resolved in the free flow, while the wall boundary layer is covered by an URANS model. Hybrid models have been applied to a variety of flow problems and have been proven to outperform RANS models for many applications [62–64]. The results of the SBES simulations for both investigated lance heights confirm this general trend.

The applied LES grid resolution in the wall boundary layer was far from being sufficient to capture wall turbulence. However, LES and SBES simulation led to almost identical results. This indicates that the flow in the PPBB burner is dominated by the free shear layer flow and the flow in the recirculation zone, rather than the wall turbulence. The separation points in the flow field are clear defined by the sharp trailing edges of the bluff body and burner housing, which justifies the application of LES with under resolved wall boundary layers over a hybrid model with proper boundary layer treatment. Such a pragmatic approach has already been applied successfully by others [65]. The main advantage of hybrid models over LES is the lower computational cost due to a considerable coarser grid resolution close to walls. Running LES and hybrid simulations on the same numerical grid puts the hybrid model in the disadvantage of having to solve, typically two, additional transport equations for the turbulence quantities. Hence, in this specific case it can be beneficial to employee LES with an under resolved wall regions.

PPBB burner flow characteristics

Flow conditions in recirculation zones created by bluff bodies or swirling flow to stabilize turbulent flames (i.e., long enough residence times, high temperature and oxygen concentration) do also promote NO_x production. The recirculation zone has been identified as a major contributor to the overall NO_x formation in bluff body and swirl burners respectively [66,67]. The NO_x formation depends on the volume of the recirculation zone, the temperature and the concentration of oxygen and nitrogen, assuming that thermal NO_x is the main contributor to the overall NO_x emission. The volume of the recirculation zone scales typically proportional to cube of the burner diameter [67]. The PIV measurements and CFD simulations of the PPBB burner showed that a variation of the lance height affected the recirculation zone length (the recirculation zone length shortened when the lance height was decreased) while the width of the recirculation zone was less affected.

This indicates that the volume of the recirculation zone also correlates to the lance height, which is consequently affecting the NO_x formation in the near-burner region. The other important parameters for the NO_x formation in the near-burner region, temperature and concentrations, are depending on the dilution level [67]. Internal recirculated flue gas which is entrained into the wall jet region of the PPBB burner will therefore affect these two parameters and hence impact the NO_x formation. Quantifying this effect based on cold flow simulations is not possible. However, the axial velocity profiles along the x-coordinate at bluff body trailing edge elevation give an indication of the entrainment as function of the lance height. Numerical integration of the velocity profiles (see Figs. 13 and 14) showed that the wall jet in the 16 mm configuration entrains 26% less than the wall jet in the 8 mm configuration.

Conclusion

In the present work, non-reacting CFD simulations of the PPBB burner were conducted. Different turbulence models were investigated, ranging from steady state RANS to scale resolving simulations, in order to identify the numerical requirements for a reasonable accurate representation of the burners main flow characteristics. The results evidence the need of scale resolving simulations. RANS simulations over predicted velocity magnitude by a large margin and were hence not able to describe the flow field adequately.

Scale resolving simulations with two different turbulence models were carried out, the novel SBES model and LES simulations with the WALE subgrid model. It was found that the SBES model is able to predict the PPBB burner flow field in good agreement with experimental data. However, conducting LES simulations on the same numerical grid and hence under resolving the wall boundary layers led to almost identical results as the SBES model. For the specific case of the PPBB burner, it is therefore advantageous to use coarse LES simulations over SBES simulations in order to reduce the overall computational costs.

The dimensions of the recirculation zone downstream of the bluff body as well as the recirculating mass flow rate were quantified for two different lance heights. The results indicate that the recirculation zone volume and the recirculating mass flow rate scale proportional to the lance height. However, more burner configurations need to be studied in order to further specify the correlation between these parameters. In addition reacting flow simulations are required to quantify the affect on the NO_x emissions from the burner.

The conical wall jet configuration is a feature special to the PPBB burner and was analysed in detail. The velocity profiles in the wall jet region contain a velocity component perpendicular to the wall, which is unusual for wall jets investigated in the literature. This component decreases in flow direction and for a lance height of 8 mm a self similar flow field is starting to establish at $x_w/\delta_{throat} = 3$. The wall jet configuration allows entrainment of internally recirculated flue gas upstream of the bluff body trailing edge/flame anchor point. It was found that increasing the lance height from 8 mm to 16 mm results in a reduction of the wall jet entrainment by 26% (from 54% of the inlet mass flow to 39%) which will lead to less dilution and hence affect the overall NO_x formation. Further reacting flow simulations in a combustion chamber need to be conducted in order to quantify the degree of dilution due to the internal flue gas recirculation and the effect of a varying lance height on it.

Acknowledgement

This publication has been produced with support from the BIGCCS Centre, performed under the Norwegian research program Centres for Environment-friendly Energy Research (FME). The authors acknowledge the following partners for their contributions: Gassco, Shell, Statoil, TOTAL, ENGIE and the Research Council of Norway (193816/S60). The authors furthermore acknowledge Marcin Dutka for providing the experimental data and his assistance in interpreting it.

REFERENCES

[1] Whitty KJ, Zhang HR, Eddings EG. Emissions from syngas combustion. Combust Sci Technol 2008;180(6):1117–36. https://doi.org/10.1080/00102200801963326.

[2] van Ruijven B, van Vuuren DP, de Vries B. The potential role of hydrogen in energy systems with and without climate policy. Int J Hydrogen Energy 2007;32(12):1655–72. https://doi.org/10.1016/j.ijhydene.2006.08.036.

[3] Dunn S. Hydrogen futures: toward a sustainable energy system. Int J Hydrogen Energy 2002;27(3):235–64. https://doi.org/10.1016/S0360-3199(01)00131-8.

[4] Cormos C-C. Evaluation of power generation schemes based on hydrogen-fueled combined cycle with carbon capture and storage (CCS). Int J Hydrogen Energy 2011;36(5):3726–38. https://doi.org/10.1016/j.ijhydene.2010.12.042.

[5] Cormos C-C. Economic implications of pre- and post-combustion calcium looping configurations applied to gasification power plants. Int J Hydrogen Energy 2014;39(20):10507–16. https://doi.org/10.1016/j.ijhydene.2014.05.033.

[7] Ditaranto M, Li H, Løvås T. Concept of hydrogen fired gas turbine cycle with exhaust gas recirculation: assessment of combustion and emissions performance. Int J Greenh Gas Contr 2015;37:377–83. https://doi.org/10.1016/j.ijggc.2015.04.004.

[8] Baukal C, Schwartz RE. The john zink combustion handbook. 1st ed. CRC Press LLC; 2001.

[9] Giles DE, Som S, Aggarwal SK. NO_X emission characteristics of counterflow syngas diffusion flames with airstream dilution. Fuel 2006;85(12–13):1729–42. https://doi.org/10.1016/j.fuel.2006.01.027.

[10] Lieuwen T, McDonell V, Santavicca D, Sattelmayer T. Burner development and operability issues associated with steady flowing syngas fired combustors. Combust Sci Technol 2008;180(6):1169–92. https://doi.org/10.1080/00102200801963375.

[11] Samiran NA, Ng J-H, Mohd Jaafar MN, Valera-Medina A, Chong CT. H_2-rich syngas strategy to reduce NO_X and CO emissions and improve stability limits under premixed swirl combustion mode. Int J Hydrogen Energy 2016;41(42):19243–55. https://doi.org/10.1016/j.ijhydene.2016.08.095.

[12] U.S. Environmental Protection Agency. Alternative control techniques document NO_X emissions from process heaters

(revised), Tech. Rep. U.S. Environmental Protection Agency, Emission Standards Division; 1993.

[13] Lieuwen T, McDonell V, Petersen E, Santavicca D. Fuel flexibility influences on premixed combustor blowout, flashback, autoignition, and stability. J Eng Gas Turbines Power 2008;130(1):011506. https://doi.org/10.1115/1.2771243.

[14] Noble DR, Zhang Q, Shareef A, Tootle J, Meyers A, Lieuwen T. Syngas mixture composition effects upon flashback and blowout. In: Proceedings of ASME Turbo expo; 2006. p. 1–12. Barcelona, Spain.

[15] Zhang Q, Noble DR, Lieuwen T. Characterization of fuel composition effects in H_2/CO/CH4 mixtures upon lean blowout. J Eng Gas Turbines Power 2007;129(3):688. https://doi.org/10.1115/1.2718566.

[16] Zhang Q, Noble DR, Shanbhogue SJ, Lieuwen T. PIV measurements in H2/CH4 swirling flames under near blowoff conditions.

[17] Schefer RW. Hydrogen enrichment for improved lean stability. Int J Hydrogen Energy 2003;28:1131–41.

[18] Dam B, Corona G, Hayder M, Choudhuri A. Effects of syngas composition on combustion induced vortex breakdown (CIVB) flashback in a swirl stabilized combustor. Fuel 2011;90:3274–84. https://doi.org/10.1016/j.fuel.2011.06.024.

[19] Fritz J, Kröner M, Sattelmayer T. Flashback in a swirl burner with cylindrical premixing zone. J Eng Gas Turbines Power 2004;126(2):276. https://doi.org/10.1115/1.1473155.

[20] Kröner M, Fritz J, Sattelmayer T. Flashback limits for combustion induced vortex breakdown in a swirl burner. J Eng Gas Turbines Power 2003;125(3):693. https://doi.org/10.1115/1.1582498.

[21] Spangelo Ø, Sonju O, Slungaard T, Ditaranto M. US 20090220899 A1 (2009).

[22] Dutka M, Ditaranto M, Løvås T. Application of a central composite design for the study of NO_X emission performance of a low NO_X burner. Energies 2015;8(5):3606–27. https://doi.org/10.3390/en8053606.

[23] Dutka M, Ditaranto M, Løvås T. Emission characteristics of a novel low NO_x burner fueled by hydrogen-rich mixtures with methane. J Power Technol 2015;95(2):105–11.

[24] Menter FR. Best practice : scale - resolving simulations in ANSYS CFD. Tech Rep 2015;2.00.

[25] Menter FR. Stress-blended eddy simulation (SBES) - a new paradigm in hybrid RANS-LES modeling. In: 6th symposium on hybrid RANS-LES methods; 2016. p. 1–17. Strasbourg, France.

[26] Dutka M, Ditaranto M, Løvås T. NO_X emissions and turbulent flow field in a partially premixed bluff body burner with CH4 and H_2 fuels. Int J Hydrogen Energy 2016;41(28):12397–410. https://doi.org/10.1016/j.ijhydene.2016.05.154.

[27] Dutka M, Ditaranto M, Løvås T. Investigations of air flow behavior past a conical bluff body using particle imaging velocimetry. Exp Fluid 2015;56(11):199. https://doi.org/10.1007/s00348-015-2068-6.

[28] Plee S, Mellor A. Review of flashback reported in prevaporizing/premixing combustors. Combust Flame 1978;32:193–203. https://doi.org/10.1016/0010-2180(78)90093-7.

[29] Putnam AA, Jensen RA. Application of dimensionless numbers to flash-back and other combustion phenomena. Symp Combust Flame Explos Phenom 1948;3(1):89–98. https://doi.org/10.1016/S1062-2896(49)80011-0.

[30] Wohl K. Quenching, flash-back, blow-off-theory and experiment. Symp (Int) Combust 1953;4(1):68–89. https://doi.org/10.1016/S0082-0784(53)80011-1.

[31] Lewis B, Von Elbe G. Combustion, flames, and explosions of gases. Academic Press; 1987.

[32] Davu D, Franco R, Choudhuri A, Lewis R. Investigation on flashback propensity of syngas premixed flames. In: 41st AIAA/ASME/SAE/ASEE joint propulsion conference & exhibit. Reston, Virigina: American Institute of Aeronautics and Astronautics; 2005. https://doi.org/10.2514/6.2005-3585.

[33] Mayer C, Sangl J, Sattelmayer T, Lachaux T, Bernero S. Study on the operational window of a swirl stabilized syngas burner under atmospheric and high pressure conditions. J Eng Gas Turbines Power 2012;134(3):031506. https://doi.org/10.1115/1.4004255.

[34] Lin Y-C, Daniele S, Jansohn P, Boulouchos K. Turbulent flame speed as an indicator for flashback propensity of hydrogen-rich fuel gases. J Eng Gas Turbines Power 2013;135(11):111503. https://doi.org/10.1115/1.4025068.

[35] Kariuki J, Dowlut A, Yuan R, Balachandran R, Mastorakos E. Heat release imaging in turbulent premixed methane-air flames close to blow-off. Proc Combust Inst 2015;35:1443–50. https://doi.org/10.1016/j.proci.2014.05.144.

[36] Kariuki J, Dawson JR, Mastorakos E. Measurements in turbulent premixed bluff body flames close to blow-off. Combust Flame 2012;159(8):2589–607. https://doi.org/10.1016/j.combustflame.2012.01.005.

[37] Andreini A, Bianchini C, Innocenti A. Large eddy simulation of a bluff body stabilized lean premixed flame. J Combust 2014;2014:1–18. https://doi.org/10.1155/2014/710254.

[38] Dawson J, Gordon R, Kariuki J, Mastorakos E, Masri A, Juddoo M. Visualization of blow-off events in bluff-body stabilized turbulent premixed flames. Proc Combust Inst 2011;33(1):1559–66. https://doi.org/10.1016/j.proci.2010.05.044.

[39] Sharma RN. Experimental investigation of conical wall jets. AIAA J 1981;19(1):28–33. https://doi.org/10.2514/3.7746.

[40] Sharma R, Patankar S. Numerical computations of wall-jet flows. Int J Heat Mass Tran 1982;25(11):1709–18. https://doi.org/10.1016/0017-9310(82)90150-8.

[41] Kolár V, Filip P, Curev AG. Similarity prediction of wall jets on bodies of revolution. Acta Mech 1989;76(3–4):253–63. https://doi.org/10.1007/BF01253584.

[42] Barth T, Jespersen D. The design and application of upwind schemes on unstructured meshes. In: 27th aerospace sciences meeting. Reston, Virigina: American Institute of Aeronautics and Astronautics; 1989. https://doi.org/10.2514/6.1989-366.

[43] Leonard B. The ULTIMATE conservative difference scheme applied to unsteady one-dimensional advection. Comput Meth Appl Mech Eng 1991;88(1):17–74. https://doi.org/10.1016/0045-7825(91)90232-U.

[44] Van Doormaal JP, Raithby GD. Enhancements of the SIMPLE method for predicting incompressible fluid flows. Numer Heat Tran 1984;7(2):147–63. https://doi.org/10.1080/01495728408961817.

[45] Armfield S, Street R. The fractional-step method for the Navier–Stokes equations on staggered grids: the accuracy of three variations. J Comput Phys 1999;153(2):660–5. https://doi.org/10.1006/jcph.1999.6275.

[46] Dukowicz JK, Dvinsky AS. Approximate factorization as a high order splitting for the implicit incompressible flow equations. J Comput Phys 1992;102(2):336–47. https://doi.org/10.1016/0021-9991(92)90376-A.

[47] Bell JB, Colella P, Glaz HM. A second-order projection method for the incompressible Navier-Stokes equations. J Comput Phys 1989;85(2):257–83. https://doi.org/10.1016/0021-9991(89)90151-4.

[48] Perot J. An analysis of the fractional step method. J Comput Phys 1993;108(1):51–8. https://doi.org/10.1006/jcph.1993.1162.

[50] Hutchinson BR, Raithby GD. A multigrid method based on the additive correction strategy. Numer Heat Tran 1986;9(5):511–37. https://doi.org/10.1080/10407788608913491.

[51] Anderson W, Bonhaus DL. An implicit upwind algorithm for computing turbulent flows on unstructured grids. Comput

Fluids 1994;23(1):1–21. https://doi.org/10.1016/0045-7930(94)90023-X.

[52] Dutka M. Emissions of nitrogen oxides from partially premixed flames stabilized on a conical bluff body. Ph.D. thesis. NTNU; 2015.

[53] Launder B, Spalding BD. Lectures in mathematical models of turbulence. London, England: Academic Press Inc; 1972.

[54] Shih T-H, Liou WW, Shabbir A, Yang Z, Zhu J. A new k- eddy viscosity model for high Reynolds number turbulent flows. Compurers Fluids 1995;24(3):227–38. https://doi.org/10.1016/0045-7930(94)00032-T.

[55] Menter FR. Two-equation eddy-viscosity turbulence models for engineering applications. AIAA J 1994;32(8):1598–605. https://doi.org/10.2514/3.12149.

[56] Nicoud F, Ducros F. Subgrid-scale stress modelling based on the square of the velocity gradient tensor. Flow Turbul Combust 1999;62(3):183–200. https://doi.org/10.1023/A:1009995426001.

[57] Taylor AMKP, Whitelaw JH. Velocity characteristics in the turbulent near wakes of confined axisymmetric bluff bodies. J Fluid Mech 2017;139:391–416. https://doi.org/10.1017/S0022112084000410.

[58] Hunt JCR, Wray AA, Moin P. Eddies, streams, and convergence zones in turbulent flows. In: Center for turbulence research CTR-S88; 1988. p. 193–208.

[59] Yoder DA, Debonis JR, Georgiadis NJ. Modeling of turbulent free shear flows. Fluid Dynam Conf Exhib;43. https://doi.org/10.2514/6.2013-2721.

[60] Pope SB, Whitelaw JH. The calculation of near-wake flows. J Fluid Mech 1976;73(01):9. https://doi.org/10.1017/S0022112076001213.

[61] Pope SB. An explanation of the turbulent round-jet/plane-jet anomaly. AIAA J 1978;16(3):279–81. https://doi.org/10.2514/3.7521.

[62] Menter FR, Kuntz M, Langtry R. Ten years of industrial experience with the SST turbulence model. In: Proceedings of the 4th international symposium on turbulence, heat and mass transfer, vol. 4. Begell House Inc; 2003. p. 625–32.

[63] Widenhorn A, Noll B, Aigner M. Numerical study of a non-reacting turbulent flow in a gas-turbine model combustor. In: 47th AIAA aerospace sciences meeting including the new horizons forum and aerospace exposition. Reston, Virigina: American Institute of Aeronautics and Astronautics; 2009. https://doi.org/10.2514/6.2009-647.

[64] Menter FR, Egorov Y. The scale-adaptive simulation method for unsteady turbulent flow predictions. Part 1: theory and model description. Flow Turbul Combust 2010;85(1):113–38. https://doi.org/10.1007/s10494-010-9264-5.

[65] Farcy B, Vervisch L, Domingo P. Large eddy simulation of selective non-catalytic reduction (SNCR): a downsizing procedure for simulating nitric-oxide reduction units. Chem Eng Sci 2015;139:285–303. https://doi.org/10.1016/j.ces.2015.10.002.

[66] Dally B, Masri A, Barlow R, Fiechtner G, Fletcher D. Measurements of no in turbulent non-premixed flames stabilized on a bluff body. Symp (Int) Combust 1996;26(2):2191–7. https://doi.org/10.1016/S0082-0784(96)80045-2.

[67] Hsieh T-C, Dahm WJ, Driscoll JF. Scaling laws for NO_X emission performance of burners and furnaces from 30 kW to 12 MW. Combust Flame 1998;114(1–2):54–80. https://doi.org/10.1016/S0010-2180(97)00289-7.

Paper II

Combustion and NO x Emission Characteristics of a Bluff Body Hydrogen Burner

Christoph Meraner, Tian Li, Mario Ditaranto, Terese Løvås

Energy & Fuels 2019;33:4598-4610.

doi:10.1021/acs.energyfuels.9b00313

energy&fuels

Article

Cite This: Energy Fuels 2019, 33, 4598−4610

pubs.acs.org/EF

Combustion and NO_x Emission Characteristics of a Bluff Body Hydrogen Burner

Christoph Meraner,*[†] Tian Li,[†] Mario Ditaranto,[‡] and Terese Løvås[†]

[†]Department of Energy and Process Engineering, Faculty of Engineering, NTNU − Norwegian University of Science and Technology, Trondheim, Norway

[‡]SINTEF Energy Research, Trondheim, Norway

ABSTRACT: Nitric oxide (NO_x) emissions from a partial premixed bluff body (PPBB) hydrogen burner under varying operational conditions have been investigated numerically. The PPBB burner employs a conical bluff body to stabilize the flame, and its design allows for the dilution of the fuel−air mixture by internally recirculated flue gas. The degree of premixing can be adjusted via primary and secondary fuel ports that are controlled independently. Steady-state computational fluid dynamic (CFD) simulations were conducted for 12 different combinations of secondary fuel fractions and thermal loads to investigate the complex flow structure in the burner and the source of NO_x formation. All simulations were validated against experimental data and underpredicted NO_x emissions by 7% on average. A detailed analysis of the combustion characteristics was conducted and showed that primary fuel is burned in a multiregime mode at a wide range of mixture fractions/equivalence ratios, while secondary fuel is burned closer to stoichiometry. Utilizing a secondary fuel fraction of 30% (i.e., the base operational condition) leads to a fuel-rich mixture within the inner recirculation zone compared to a fuel-lean mixture when the burner is operated without secondary fuel. The concave mean curvature of the stoichiometric isosurface between primary and secondary fuel leads furthermore to a local peak of the NO_x formation rate when the burner operates at its base conditions. The analysis of the mass flow rates in the inner and outer recirculation zones showed that increasing the thermal load reduces the amount of internally recirculated flue gas. The conducted simulations indicate that these effects contribute to an increase in NO_x emissions with increasing thermal load and with increasing secondary fuel fraction.

1. INTRODUCTION

Nitric oxide (NO_x) emissions from combustion and industrial processes at high temperatures continue even after decades of research to be an environmental challenge. NO_x is not only a critical air pollutant by itself but also contributes to the formation of tropospheric ozone (i.e., ozone in the air that we breathe), smog, and acid rains.[1,2] Hence, there is an obvious need to keep NO_x emissions as low as reasonably practicable, which has led to the development of a variety of different low NO_x and ultralow NO_x burners. However, low NO_x combustion technologies for burners always result in a trade-off between the requirements of fuel burn out, static and dynamic stability, and NO_x formation. Thermal NO_x can for example be greatly reduced by lowering the flame temperature, which in turn may lead to incomplete combustion and emission of unburned hydrocarbons and CO. NO_x emissions on the other hand can be negatively affected by technologies that address primarily other challenging aspects of combustion such as flame stability or emissions of other pollutants. An example for this is utilizing hydrogen as fuel in precombustion carbon capture and storage (CCS) that was developed to reduce CO_2 emissions to the atmosphere but leads to challenges regarding NO_x and the risk of flashbacks. Precombustion CCS utilizes a water−gas shift reaction, in either gasification of solid fuels or steam methane reforming, to convert CO and H_2O to H_2 and CO_2. The latter can then be captured and stored prior to the combustion of the remaining syngas. Some of the benefits of precombustion CCS are the lack of use of potentially harmful amines and that nearly carbon free syngas can be produced.[3,4] However, the elevated combustion temperature of hydrogen-rich fuels increases the generation of thermal NO_x, which correlates exponentially to the combustion temperature.[5] The significantly different transport properties and flame speed of hydrogen compared to other gaseous fuels[6] can furthermore increase the potential for flame flashbacks in the burner.[7] Syngas combustion, especially in the context of precombustion, imposes therefore special requirements regarding NO_x emissions and flame stability to the burner design.

The partially premixed bluff body (PPBB) burner investigated in the present study was originally designed by Spangelo et al.[8] for the combustion of propane and natural gas. However, its design features allow for a wide fuel flexibility and make it therefore also an ideal candidate for the combustion of hydrogen and hydrogen-rich fuels. The burner is intended for the use in boilers and furnaces that typically operate at pressures close to atmospheric pressure and with approximately 3% excess air. This sets the boundaries for applicable NO_x reducing measures and prohibits for example the combustion at overall ultralean conditions. The PPBB burner employs a frustum-shaped conical bluff body (see Figure 1) that can be adjusted in axial direction, which allows the optimization of the burner for the operation with varying fuel compositions.[9] The primary and secondary fuel ports are

Received: January 29, 2019
Revised: April 5, 2019
Published: April 17, 2019

DOI: 10.1021/acs.energyfuels.9b00313
Energy Fuels 2019, 33, 4598−4610

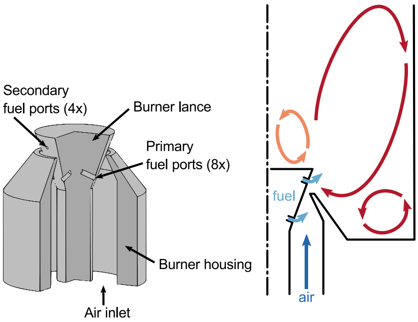

Figure 1. Three-dimensional rendering of the PPBB burner and flow field illustration based on Meraner et al.[15] The fuel ports are, for simplicity, drawn in the same plane.

controlled independently from each other in order to control the amount of premixing and hence further increase the fuel flexibility. The design of the secondary fuel ports is also intended to increase flame stability by enriching the recirculation zone. Flame stabilization through a bluff body has the benefit of avoiding flashbacks from a combustion induced vortex breakdown (CIVB), which is a common challenge for swirl stabilized burners.[10,11] Flashbacks can also occur as an upstream propagating premixed flame within a boundary layer.[12−14] The boundary layers need therefore to be kept as thin as possible to avoid these types of flashbacks.[10] The PPBB burner achieves this by premixing the majority of fuel in the converging burner section where the accelerating mean flow leads to a decreasing boundary layer thickness. One of the unique features of the PPBB burner is its elevated lance position. Because of this lance design, internal recirculated flue gas is entrained in the conical wall jet which is formed between the burner throat and the flame anchor point (see Figure 1). The burner dimensions and a more in-depth description of its features can be found in previous work.[15] The performance of the PPBB burner, with regard to NO_x emissions, has been investigated experimental by Dutka et al.[9,16] The available data from the experimental campaigns are, however, limited to global measurements of NO_x at the chamber outlet. Particle image velocimetry (PIV) has been applied to analyze the flow field downstream of the bluff body.[17] The PIV measurements have, however, only been performed for an unconfined burner configuration due to limited optical access into the combustion chamber. The cold flow characteristics of the unconfined burner configuration have also been investigated numerically by means of Reynolds averaged (RANS) and scale resolving simulations.[15] However, so far no detailed analysis of the reacting flow has been published, neither for the unconfined nor the confined configuration. The present work aims to fill this gap and, for the first time, to allow a detailed analysis of the fluid- and thermodynamics of the PPBB burner when operated with hydrogen. The scope of the present work focuses on the overall NO_x trends rather than aiming for quantitative accuracy, given the limited available experimental data. In this context, it is furthermore desired to develop a numerical model that can be run at reasonable costs and thus can be employed in future studies to investigate the PPBB burner at larger scales.

The paper structure follows the scope, namely, first to develop and validate a CFD model of the PPBB burner and second to investigate the combustion characteristics of the burner. Specific considerations regarding uncertainties are given in addition to the model description. The model is then used to investigate the combustion regimes in which the burner operates and to analyze parameters that affect NO_x formation in the burner.

2. NUMERICAL METHODS

The numerical simulation of the PPBB burner incorporates several challenging aspects that need to be addressed. One of them is the mixing mode in which the burner operates. Primary fuel and combustion air are only partially premixed, and the mixture fraction varies along the burner circumferences. Adding secondary fuel to the system is supposed to generate local fuel-rich areas that increase the flame stability while still allowing the burner to be operated globally at fuel-lean conditions. The PPBB burner can therefore not be categorized by a pure premixed or diffusive combustion regime. Research and model development have historically often been focused on one of these two regimes at a time only. Although the understanding as well as modeling capability of homogeneous partially premixed flames has improved significantly over the past decade, inhomogeneous partially premixed and stratified flames, such as the PPBB burner, are still not fully explored.[18,19]

When selecting a combustion model, one can generally choose from three different categories. These are flamelet-like models that are based on a geometrical analysis of the flame structure, PDF-like models that are based on one-point statistics, and models that are based on the analysis of turbulent mixing.[20] PDF-like models have been successfully employed for the accurately description of several laboratory jet flames.[21,22] However, they are typically computationally the most expensive models. Flamelet-like models on the other hand are in general relatively inexpensive to use and can achieve high accuracy when they are applied within their limitations.[23] However, they are based on the strong assumptions that turbulent combustion lies close to a very low-dimensional manifold. Furthermore, they aim to parametrize the complex nature of turbulence-chemistry interaction by only a few variables.[19] These assumptions are not true when molecular diffusion leads to departures from the manifold (e.g., due to the preferential diffusion of H_2 and H) and/or if the involved chemical reactions have significantly different time scales compared to the combustion chemistry (e.g., NO_x chemistry). Another disadvantage of flamelet-like models is the increased memory demand associated with them. Flamelet-like models represent a trade-off between computational costs in terms of CPU hours and memory demand. The computation time can be significantly reduced by these models, particularly for larger reaction mechanisms. However, the necessary look-up tables can become very large, especially when additional dimensions are added to account for nonadiabatic effects, NO_x, etc. The present work employs an unstructured polyhedral mesh for the CFD simulations of the PPBB burner, which requires more memory compared to other mesh types such as cut-cell or hex meshes. A further increase in memory demand by the combustion model is, therefore, not desired. The most prominent examples for the third category (i.e., models based on turbulent mixing) are the eddy-breakup (EBU) model[24] and the eddy-dissipation concept (EDC).[25,26] These models invoke more modeling assumptions than the previous mentioned models and are consequently regarded as less accurate. However, they still present certain advantages. The EDC model is considerable less computationally expensive than the transported PDF models. At the same time it allows the computation of detailed chemical kinetics, which makes the model not as strictly confined to certain combustion regimes as flamelet-like models. Furthermore, it allows NO_x kinetics to be included directly in the reaction mechanism if desired. The EDC model in a RANS context in combination with detailed chemistry is therefore regarded as a well balanced model setup for the PPBB burner, particularly given the limited experimental data available for the burner.

2.1. Numerics and Boundary Conditions.

Incompressible steady-state RANS simulations, using the ANSYS Academic Fluent,

DOI: 10.1021/acs.energyfuels.9b00313
Energy Fuels 2019, 33, 4598−4610

Release 18.2 framework, were conducted to model the PPBB burner. A second order upwind scheme,[27] based on the finite volume method, was employed to discretize all governing transport equations. The system of equations was solved with a point implicit (Gauss-Seidel) solver in conjunction with an algebraic multigrid method.[28] The employed colocated scheme requires a pressure interpolation at the cell faces which was done with a second order central difference scheme. A cell-based least-square method was used for the calculation of gradients and derivatives.[29] Furthermore, the warped-face gradient correction was applied to improve the accuracy of the gradient calculation on the polyhedral mesh. The pressure-implicit with splitting of operators (PISO) solver was applied for the pressure−velocity coupling in conjunction with skewness and neighbor correction as well as skewness−neighbor coupling in order to improve convergence on an unstructured polyhedral mesh.[30,31]

Only one-fourth of the burner was simulated, utilizing periodicity to decrease the numerical cost (see Figure 2). The burner configuration comprises a 600 mm long combustion chamber with an inner diameter of 105 mm (see Figure 2). Dutka et al.[9] measured NO_x with an additional duct on top of the combustion chamber. The duct was not included in the CFD simulations based on the findings from a preceding simulation, which indicated that the NO_x concentration reaches its equilibrium toward the outlet of the combustion chamber. However, the outlet was extended by 50 mm to prevent the boundary from affecting the data collection at an axial position of 585 mm. The edges of the combustion chamber were modeled with a 10 mm radius to ease convergence. It was assumed that this will not affect the flow characteristics of the burner due to the distance to the flame.

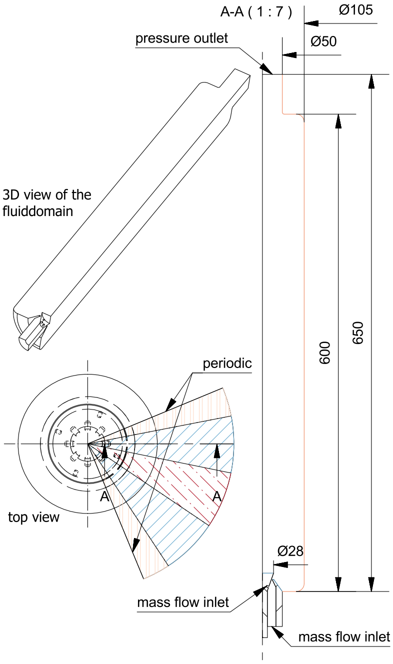

Figure 2. Dimensions (mm) of the fluid domain and boundary conditions. All unspecified boundaries were modeled as no-slip wall. Orange and blue lines in the side view indicate that a constant wall temperature was set equal to T_{chamber} and T_{burner} respectively. The domain was for postprocessing purposes subdivided into five different sectors that are marked by color-coded patterns in the top view. Note that the grid is not affected by these divisions.

All inlets were defined as mass flow inlets with a turbulent intensity of 5% and a turbulent viscosity ratio of 10. The inlet temperature was set to 293 K. Constant atmospheric pressure was imposed at the chamber outlet. All walls were modeled as no-slip walls. A constant temperature was specified at the chamber walls (i.e., all walls marked orange in Figure 2) and the burner walls that are exposed to the combustion chamber environment (i.e., all walls marked blue in Figure 2) (see Table 1). All other walls were modeled adiabatic. The chamber temperature, T_{chamber} listed in Table 1 was based on the averaged chamber temperature measured in the experimental campaign.[9] The burner temperature, T_{burner} was set to 850 K for the base case (i.e., 10 kW thermal input, Q, and 30% secondary fuel fraction) and scaled proportional to T_{chamber} for other operational conditions. A discussion on the uncertainty related to this assumption is presented in section 2.4. A uniform emissivity of 0.5 was applied to the walls.

Table 1. Boundary Conditions[a]

Q (kW)	$\dot{m}^{s}_{\text{fuel}}/\dot{m}^{p}_{\text{fuel}}$ (%)	$\dot{m}_{\text{air}}$ (kg/s)	$\dot{m}_{\text{fuel}}$ (kg/s)	T_{chamber} (K)	T_{burner} (K)
10	0	8.267×10^{-4}	2.083×10^{-5}	1316	860
10	10	8.267×10^{-4}	2.083×10^{-5}	1311	857
10	20	8.267×10^{-4}	2.083×10^{-5}	1306	854
10	30	8.267×10^{-4}	2.083×10^{-5}	1300	850
15	0	1.240×10^{-3}	3.125×10^{-5}	1437	940
15	30	1.240×10^{-3}	3.125×10^{-5}	1438	940
20	0	1.653×10^{-3}	4.167×10^{-5}	1501	982
20	30	1.653×10^{-3}	4.167×10^{-5}	1510	987
25	0	2.067×10^{-3}	5.208×10^{-5}	1553	1015
25	10	2.067×10^{-3}	5.208×10^{-5}	1552	1015
25	20	2.067×10^{-3}	5.208×10^{-5}	1555	1017
25	30	2.067×10^{-3}	5.208×10^{-5}	1563	1019

[a] The mass flow rates for air $\dot{m}_{air}$, primary fuel $\dot{m}^{p}_{\text{fuel}}$ and secondary fuel $\dot{m}^{s}_{\text{fuel}}$ listed in the table are for the quarter domain (i.e., 25% of the experimental mass flow rates).

2.2. Grid Study. The PPBB burner poses a challenging geometry for a numerical analysis, due to the arrangement of its several fuel ports and large ratio between throat diameter and chamber dimensions. Different meshing strategies have been employed and discussed in previous work.[15] It has been concluded that an unstructured polyhedral mesh (see Figure 3) represents a suitable strategy for the PPBB burner simulations.

One benefit of unstructured meshes is the capability of local mesh refinements without affecting the far field mesh size. Four refinement regions were defined for the simulations of the PPBB burner. The refinements include the area of interest (i.e., the recirculation zone downstream of the bluff body), the premixing region in the converging section of the burner upstream of the throat, and two levels of refinements in the shear-layer/flame anchor point at the trailing edge of the bluff body. A disadvantage of unstructured meshes is the overall larger cell count compared to structured meshes. A grid independency study was conducted spanning a total cell count from 2.2 million cells to 4.8 million cells (see Figure 4). The 2.7 million and the 2.2 million mesh are based on the same cell size distribution, however, the 2.7 million mesh includes a grid refinement toward the bluff body walls. The grid independency study was conducted for a thermal load of 10 kW and a secondary fuel ratio of 30%, which are the base operation conditions of the burner when fuelled with pure hydrogen. Increasing the thermal input leads to higher Reynolds numbers and is therefore more demanding in terms of spacial grid resolution, especially for the flow in boundary layers. Utilizing wall functions, however, reduces the grid sensitivity. It is therefore not expected that the conclusions, in terms of NO_x trends, for the larger thermal input would be drastically affected by a grid refinement. All

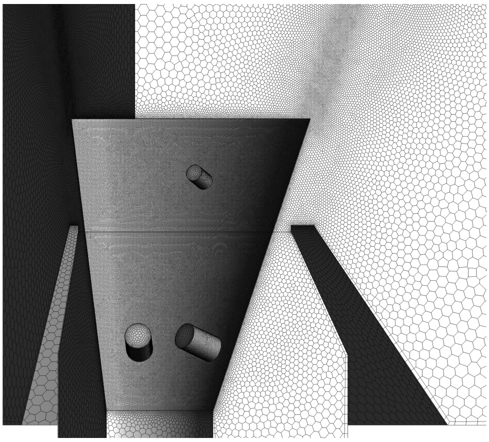

Figure 3. Close-up view of the polyhedral surface mesh for the 3.5 M cell mesh.

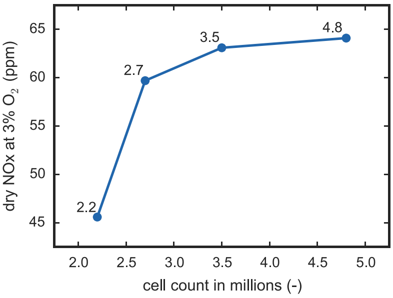

Figure 4. NO_x sensitivity to spacial resolution.

simulations for the independency study were conducted with a chamber temperature of 1300 K and a burner temperature of 700 K. Thermal radiation was neglected for the grid independency study to reduce computational costs. This is not expected to affect the grid independency significantly. All further simulations were conducted on the 3.5 million mesh based on the outcome of the grid independency study.

2.3. Submodels.

The inherently complex nature of turbulent combustion requires the application of a large set of submodels in order to be able to simulate it numerically. This section addresses the submodels that were employed for the simulation of the PPBB burner. An overview of these submodels is given in Table 2.

The flow field downstream of the burner behaves, after a transition region, similar to a round jet. The flow downstream of the burner throat next to the bluff body is on the other hand similar to a planar wall-jet (especially for larger bluff body diameters). This configuration makes the burner sensitive to the known round-jet anomaly (i.e., the poor performance of the standard k−ϵ models for the prediction of the spreading rate of axisymmetric jets, while performing reasonable well for planar jets). Therefore, the realizable k−ϵ model[32] was employed for the PPBB burner simulations, which is in this regard considered superior to the standard and RNG k-ϵ models. A two-layer based, nonequilibrium wall function[33] was applied in the near wall region. The nonequilibrium wall function can partly account for the effect of pressure gradients involving separation and reattachment and is expected to perform better than standard wall function, particularly with regard to the prediction of wall shear (skin-friction coefficient) and heat transfer (Nusselt or Stanton number). This is of special importance for the PPBB burner simulations that have shown to be sensitive to the heat transfer to the bluff body as well as to the heat transfer to the combustion chamber walls.

Table 2. Summary of the Employed Submodels

phenomenon	model
turbulence	realizable k−ϵ[32]
wall treatment	nonequilibrium wall function[35,37]
turbulence-chemistry interaction	eddy-dissipation concept[25,26]
combustion kinetics	Li et al.[34]
NO_x kinetics	extended Zeldovich[5]
radiation	discrete ordinates
absorption	weighted sum of gray gases
viscosity and thermal conductivity	kinetic theory
diffusive flux	dilute approximation
binary mass diffusion coefficients	modified Chapman−Enskog[36]

The eddy-dissipation concept (EDC)[25,26] was employed to model turbulence-chemistry interaction. The EDC model assumes that all chemical reactions happen at the smallest turbulent scales which are described as fine structures by Magnussen et al.[25] The fine structures were modeled as a perfectly stirred reactor. The combustion kinetics were described using the well-known mechanism by Li et al.[34] containing 9 species and 19 reversible reactions. Thermal NO formation was modeled by the extended Zeldovich mechanism[5] in a finite rate postprocessing approach, assuming that the combustion kinetics and NO kinetics can be decoupled from each other and that the effect of NO formation on the combustion process itself can be neglected. The concentrations of O and OH were modeled as steady state, based on this assumption. The mean reaction rates were obtained by integration of a presumed joint-variable Beta PDF for temperature and O_2. The variance for the presumed PDF was modeled using an algebraic approximation of its transport equation.[35]

The discrete ordinates (DO) radiation model was employed to describe thermal radiation by solving the radiative transfer equation for a finite number of discrete solid angles. The absorption coefficient for the mixture was calculated with the weighted sum of gray gases model (WSGGM), while the scattering coefficient was set to zero. Including thermal radiation in the CFD model showed a decrease of the global NO_x emissions by 6% at base case conditions. The viscosity and thermal conductivity were calculated employing kinetic theory (i.e., Lennard−Jones potential). The diffusive mass flux was calculated based on the dilute approximation (i.e., Fick's law) for turbulent flows, which is written as

$$\vec{J}_i = -\left(\rho D_{i,m} + \frac{\mu_t}{Sc_t}\right)\nabla Y_i \tag{1}$$

where Y_i is the mass fraction and $D_{i,m}$ is the mass diffusion coefficient for species i in the mixture m, Sc_t is the turbulent Schmidt number with a constant value of 0.7, ρ is the mixture density and μ_t is the turbulent viscosity. The diffusion coefficients in the mixture $D_{i,m}$ are obtained from the binary mass diffusion coefficient $\mathcal{D}_{ij}$ of species i in species j

$$D_{i,m} = \frac{1 - X_i}{\sum_{j,j\neq i}(X_i/\mathcal{D}_{ij})} \tag{2}$$

where X_i is the volume fraction of species i. The binary mass diffusion coefficients $\mathcal{D}_{ij}$ are computed with a modified Chapman−Enskog formula[36]

$$\mathcal{D}_{ij} = 0.00188\frac{\left[T^3\left(\frac{1}{M_{w,i}} + \frac{1}{M_{w,j}}\right)\right]^{1/2}}{p_{\mathrm{abs}}\sigma_{ij}^2\Omega_{\mathrm{D}}} \tag{3}$$

2.4. Uncertainties and Sensitivities.

By their nature, all models inhere uncertainties. The impact of model uncertainties on the results depends, however, on the sensitivity of the results to the specific model. The uncertainties associated with models that have the strongest impact on the simulation outcome will be the limiting factor of the overall accuracy that can be achieved by the simulation. NO_x is a minor species, in low NO_x environments, and is highly temperature dependent. The quantitative prediction of NO_x emissions requires therefore high accuracy of all submodels that affect the temperature. The model input for the simulation of the PPBB burner includes the thermal boundary conditions of the combustion chamber and the burner itself. The experimental data available for the chamber boundary conditions, which are important for the flame shape and temperature,[38] are limited to three unshielded thermocouples at different axial positions along the chamber wall and are therefore associated with a high uncertainty. The bluff body surface temperature was not monitored during the experimental campaign, but it has an important impact on the flame structure downstream of the bluff body, as shown in studies by Euler et al.[39] and Michaels and Ghoniem.[40] A set of simulations with different burner temperatures, with and without the inclusion of thermal radiation, were performed in order to assess the sensitivity of the global NO_x emissions to the burner temperature. The simulations were mainly focused on a temperature range of 700−900 K, as no distinct glowing of the bluff body was observed during the experiments. In addition, one simulation with T_{burner} = 1300 K was performed to establish an upper limit. The sensitivity simulations showed a linear dependency of the global NO_x emissions on the thermal boundary conditions of the bluff body.

The treatment of molecular diffusivity is of special importance for the combustion of hydrogen due to the preferential diffusion of H_2 and H. Three different approaches were investigated for the PPBB burner simulations. The most detailed description applied was the full multicomponent diffusivity including thermal diffusivity (i.e., Soret effect). Here, the diffusive mass flux was calculated by solving Maxwell−Stefan equation[41] for an ideal gas, assuming the external force is the same on all species and that pressure diffusion is negligible. The full multicomponent approach was also investigated neglecting thermal diffusion. The third approach was to calculate the diffusive mass flux based on the diluted approximation for turbulent flows as described in the previous subsection. The difference in overall NO_x emissions between these three approaches is with less than 1 ppm negligible. This indicates the dominance of the turbulent transport, which is determined by the turbulent Schmidt number. On the basis of these findings, all further simulations were conducted using the diluted approximation (see section 2.3).

The design of the laboratory scale PPBB burner leads to regions with a low Reynolds number, as for example in the bottom area of the chamber where hot products are recirculated at low velocities. These areas are sensitive to the type of employed near wall treatment due to their low Reynolds number. Sensitivity simulations with the standard, the scalable, and the nonequilibrium wall function formulation for ANSYS Academic Fluent, Release 18.2 were conducted.[35,37] The formation of secondary vortex structures was suppressed in the simulations with the standard and with the scalable wall function, and the flow was forced to follow the chamber wall, which led to the formation of a single outer recirculation vortex. Only the nonequilibrium formulation allowed for flow separation at the walls and the natural formation of secondary vortex structures and was therefore employed in all further simulations.

3. RESULTS

The results of the numerical simulations are presented in two subsections: The first subsection, *Model Validation*, presents the validation of the CFD simulations against experimental data. The second subsection, *Combustion Regime and Flame Characteristics*, provides a more thorough analysis of the PPBB burner, mainly operating at its base configuration.

3.1. Model Validation.

The NO_x emission from the burner were monitored at 585 mm axial position and compared to the corresponding experimental measurements from Dutka et al.[9] Both data sets were normalized to 3% oxygen under dry conditions. Figure 5 shows the deviation between simulations and experiments. The 12 investigated operational conditions are gathered into two data point clusters. The majority of the experimental data lies between 80 and 95 ppm, while three experiments achieved low NO_x emissions in the range of 65−70 ppm. The deviation between simulation and experiment for the low NO_x conditions is scattered in the range of −5% to +10%. A more consistent deviation of about −10% can be seen under higher NO_x conditions, with the exception of cases without any secondary fuel. These show the highest deviation which lies in the range of −12% to −18%. It should also be noted that all low NO_x emissions were achieved by cases with a nominal thermal heat load of 10 kW.

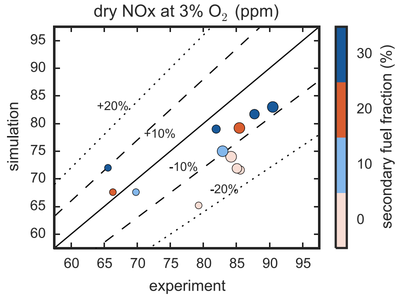

Figure 5. Predicted versus measured dry NO_x at 3% O_2. The marker size is proportional to the thermal power. The marker color represents the secondary fuel fraction. The dashed lines indicate ±10% deviation and the dotted lines indicate ±20% deviation.

Figure 6 and Figure 7 show how well NO_x trends are captured by the CFD model in addition to the overall accuracy that was shown in Figure 5. The experimental data show a higher dependency of NO_x emissions on the thermal input when the burner operates with secondary fuel compared to the operation without any secondary fuel. The NO_x trend without secondary fuel is well captured by the CFD model, but the

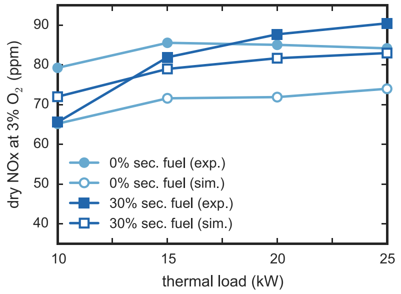

Figure 6. Dry NO_x at 3% O_2 as function of the thermal load for a constant secondary fuel fraction of 0% and 30% respectively. Filled markers are used for experimental data. Empty markers are used for data obtained from CFD.

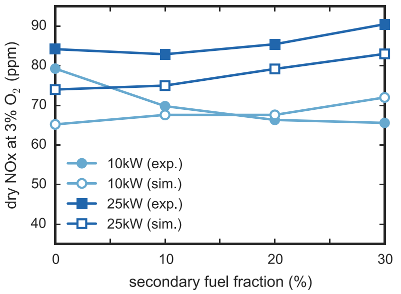

Figure 7. Dry NO_x at 3% O_2 over secondary fuel fraction for a constant thermal load of 10 kW and 25 kW respectively. Filled markers are used for experimental data. Empty markers are used for data obtained from CFD.

emissions are generally underpredicted by about 15%. The overall trend of the 30% secondary fuel configuration is captured by the simulation. However, the slope of the curve is underpredicted, which leads to a larger variance of the deviation compared to the configuration without secondary fuel. This can also be seen in Figure 5 in the form of a linear trend for the 30% secondary fuel data points.

Figure 7 shows the NO_x dependency on the secondary fuel fraction for two different thermal loads. The NO_x trend is well captured for a thermal load of 25 kW, but consistently underpredicted by around 9%, which can also be seen in Figure 5. The CFD model, however, fails to capture the trend for a lower heat load of 10 kW and predicts an increase of NO_x with increasing secondary fuel fraction. The trend predicted in the CFD model corresponds to what has been observed in the experiment for methane. The experiments with hydrogen, however, showed a decrease of NO_x with an increasing secondary fuel fraction, which was not explained in the original study. It appears that the effect of secondary fuel is the most challenging aspect to be captured by the model. The following section will therefore focus on simulations of the burner at the base thermal load (i.e., 10 kW) with two different secondary fuel fractions.

3.2. Combustion Regime and Flame Characteristics.

A classical approach to get a first view of the combustion regimes are the development of combustion/regime diagrams. Such diagrams are historically based on the interaction of homogeneous and isotropic frozen (i.e., unaffected by heat release) turbulence with a premixed flame. Hence, one needs to keep their limitations in mind when they are utilized in the context of a technical flame. Figure 8 shows a modified turbulent combustion diagram based on Peters.[42] Typically a burner is represented by a single marker within the diagram. However, the combustion in a partially premixed burner will likely cross different regions in the regime diagram. The PPBB burner is therefore represented through a scatter plot, where each data point represents the conditions in one CFD cell on a predefined clipped isosurface, which provides a more refined picture. The data shown in Figure 8 represent the burner operating at its base conditions.

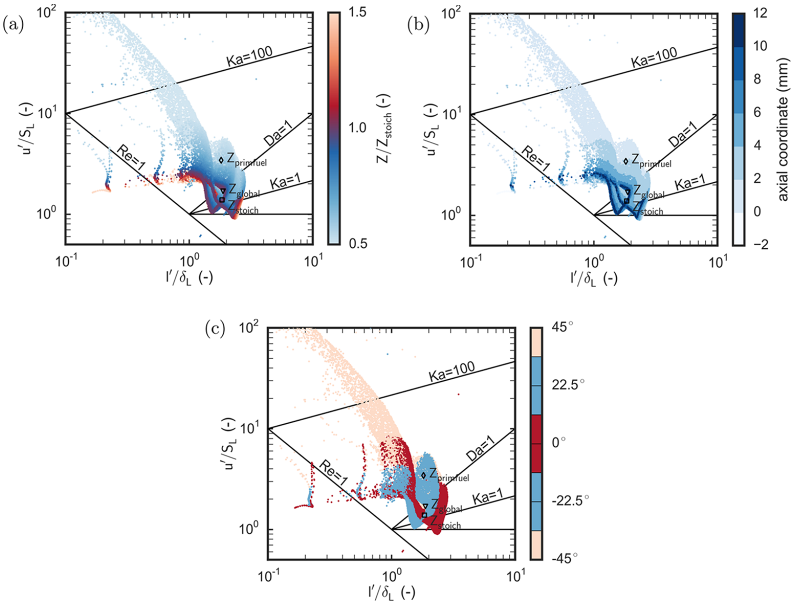

Figure 8. Modified turbulent combustion diagram by Peters[42] including scatter plots for the PPBB burner operating at base conditions. Three markers are added to each subfigure to indicate the location of the PPBB burner within the regime diagram on a global basis. Triangle: based on the global equivalence ratio, square: based on a stoichiometric equivalence ratio, diamond: based on the equivalence ratio considering only primary fuel. (a) Scatterplot colored by the mixture fraction, Z, normalized by the stoichiometric mixture fraction, Z_{stoich}. (b) Scatter plot colored by the axial coordinate. (c) Scatter plot colored by the angular coordinate. The secondary fuel port is located at 0°, the primary fuel ports are located at +22.5° and −22.5° respectively.

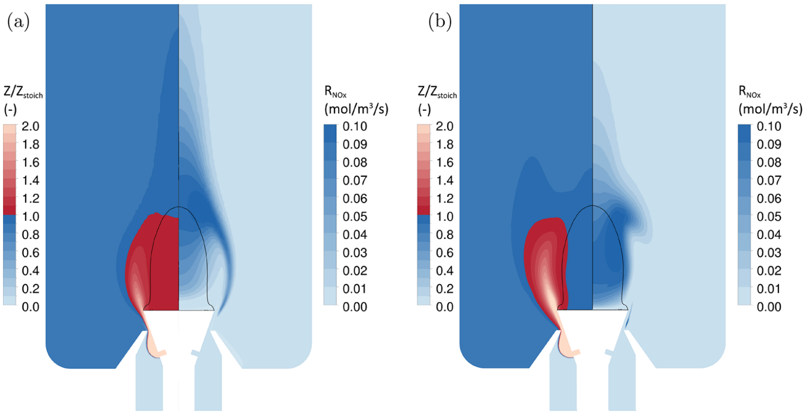

Figure 9. Normalized mixture fraction Z/Z_{stoich} (left) and NO_x formation rate (right) from the base case simulation. The black isoline (zero axial velocity) indicates the inner recirculation zone. (a) 10 kW thermal load, 30% secondary fuel. (b) 10 kW thermal load, no secondary fuel.

In order to obtain data that are suitable for the regime diagram, an isosurface needs to be defined that is close to the flame, so that the mixture composition is representative for the combustion. However, the location of the isosurface needs to be far enough from the flame, so that the turbulence is not yet affected too heavily by the heat release. An isovalue of 5% of the maximum heat release rate was chosen for this. The isosurface was furthermore clipped using a normalized progress variable (i.e., $(Y_{HO_2} + Y_{H_2O})/(Y_{HO_2} + Y_{H_2O})^{eq}$) of 0.5 as an upper limit to ensure that the data are collected in the region of the leading flame front (i.e., on the reactants side of the flame). The intermediate species HO_2 was included in the progress variable definition to capture the onset of the combustion reactions. However, for the sole purpose of distinguishing between product and reactant side of the flame, it would be sufficient to base the progress variable on the H_2O mass fraction only. The data points for the scatter plots are sorted by their distance to the stoichiometric mixture fraction. Hence, data points closer to the stoichiometric mixture fraction overlay points that are further away from stoichiometry, independent of which side (i.e., fuel lean or rich) they are located.

In addition to the scatter data, three global representations of the PPBB burner combustion regimes are provided in Figure 8. The turbulent length scale, l', and the turbulent velocity scale, u', for these were based on the area weighted average conditions in the burner throat. The laminar flame speed, S_L, and laminar flame thickness, δ_L, were calculated in the open-source software Cantera[43] based on the global equivalence ratio of the burner (triangle), a stoichiometric equivalence ratio (square), and an equivalence ratio based on the primary fuel only (diamond). The calculation based on the global equivalence ratio corresponds to a typical representation of a fully premixed burner. Stoichiometric conditions on the other hand can be seen as the representation of a diffusion flame. Because of the location of the fuel ports, it is likely that more of the primary fuel is premixed compared to the secondary fuel. Hence, the PPBB burner can, in a simplified way, be represented by two markers in the regime diagram: one representing the secondary fuel burning in a diffusive mode close to a unity Karlovitz number and the second one representing the primary fuel burning in a premixed mode at higher Karlovitz numbers. The primary fuel is consequently burned at leaner conditions compared to the global equivalence ratio.

The scatter plot in Figure 8a is colored by the normalized mixture fraction, which has a value that becomes smaller than one under fuel-lean conditions (colored blue) and larger than one in the fuel-rich conditions (colored red). The luminosity/saturation indicates the distance to the stoichiometric mixture fraction. It can be seen that the PPBB burner operates in a multiregime mode due to its partially premixed nature. A cluster of data points is located around the global regime indicators (i.e., Z_{stoich}, Z_{global}, and $Z_{primfuel}$) in the thin reaction zone region (i.e., $1 < K_a < 100$) and crossing into the corrugated flamelet region (i.e., $K_a < 1$ and $u'/S_L > 1$). Two “flares” can be noticed in the figure. One of it shows increasing Karlovitz numbers and crosses into the broken reaction zone region (i.e., $K_a > 100$). This is due to the very lean mixture that is located in between primary fuel ports (see Figure 8c), which leads to thicker flames and lower flame speeds. The second “flare” shows a decreasing Reynolds number and crosses into the laminar combustion region. This indicates that the heat release starts to affect the turbulence leading to a laminarization of the flow. Figure 8b shows the scatter data colored by the axial position. The trailing edge of the bluff body is located at an axial position of 0 mm. Fuel entering via the primary fuel ports is embedded in a premixed mixture when it reaches the burner throat, where hot recirculated flue gas is entrained into the wall-jet surrounding the bluff body. Hence, combustion occurs in large parts at lean mixture fractions within 2−4 bluff body diameters, D, downstream of the burner trailing edge (see Figure 8a,b). The scatter plot is at these elevations spread out across multiple regimes due to a relatively large variation in mixture fraction. The mixture fraction variation decreases further downstream, and a double v-shaped distribution is visible, which is characterized by a rich and stoichiometric mixture (see Figure 8a). Figure 8c shows the angular distribution within the regime diagram. The color coding corresponds to the sectors marked in Figure 2. Fuel burning in the secondary fuel sector (dark red) is mainly burned at rich and stoichiometric equivalence ratios. Fuel in the primary fuel sector (blue) shows a larger scatter where rich

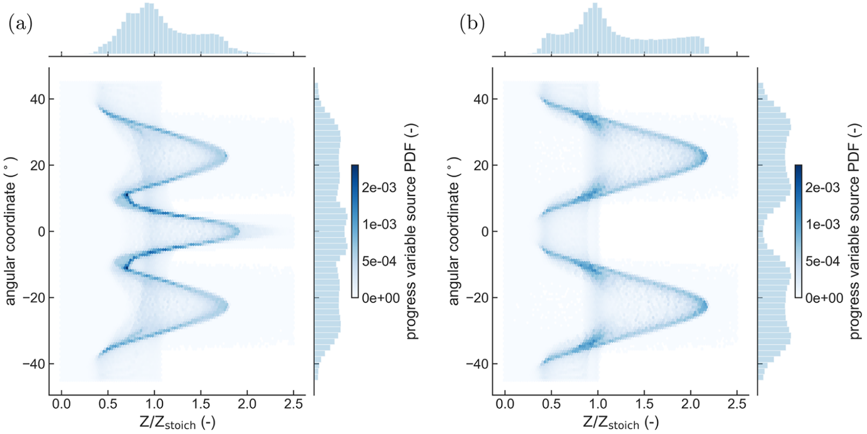

Figure 10. Hexbin plot of the progress variable source term (i.e., $R_{HO_2} + R_{H_2O}$) probability density distribution integrated along the axial and the radial directions, plotted in a two-dimensional space formed by the mixture fraction, normalized by the stoichiometric mixture fraction and the angular coordinate. The marginal plots show the probability density function of the progress variable source term along the corresponding axes. (a) 10 kW thermal load, 30% secondary fuel. (b) 10 kW thermal load, 30% secondary fuel.

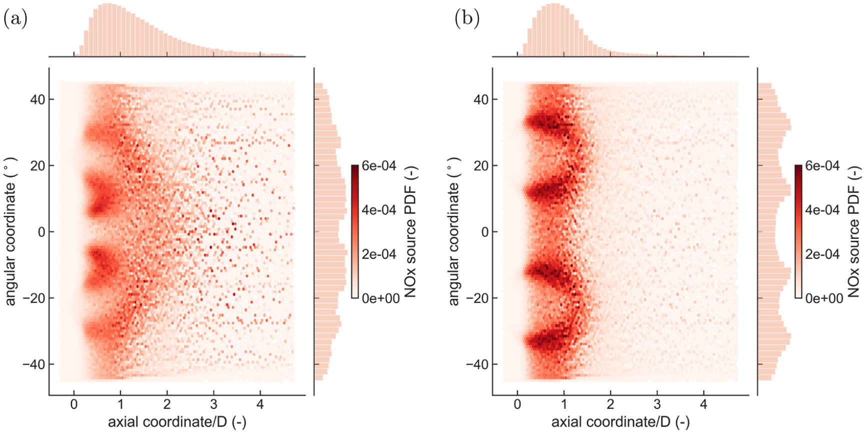

Figure 11. Hexbin plot of the NO_x source probability density distribution integrated along the radial direction. The marginal plots show the probability density function of the NO_x source term along the corresponding axes. (a) 10 kW thermal load, 30% secondary fuel. (b) 10 kW thermal load, no secondary fuel.

and stoichiometric regions show a similar pattern as the secondary fuel but at slightly lower length scale ratios. Lean mixtures burn at higher velocity ratios.

Figure 9 shows the normalized mixture fraction distribution side by side with the NO_x formation rate in a plane cutting through two primary fuel ports for two different cases. Note the NO_x contours are mirrored with respect to the burner axis to allow a direct comparison with the mixture fraction contours within the same subfigure. The inner recirculation zone is indicated by an isoline of zero axial velocity and is characterized by a fuel-rich mixture for the base configuration (see Figure 9a) and a fuel-lean mixture for the operation without secondary fuel (see Figure 9b). Secondary fuel is less premixed compared to the primary fuel and enriches therefore the inner recirculation zone and the intermediate postflame region. The NO_x formation rate correlates with the mixture fraction and reaches high values close to stoichiometry.

This relationship is further investigated in Figure 10 and Figure 11. Figure 10 shows the distribution of the probability density for the progress variable source term. The data are shown in a hexbin plot, which allows the numerical integration of the progress variable source in radial and axial directions. Figure 10 shows thus the angular positions at which reactants are converted to products and at which mixture fraction this happens. The marginal plots show the PDF distribution along the corresponding axes. Figure 10a represents the PPBB burner operating at base conditions, while Figure 10b shows the burner operating without secondary fuel. At base condition, 70% of the fuel mass flow is provided via the primary fuel ports. The remaining 30% are introduced through the secondary fuel ports. The mass flow rate in a single primary fuel port is, however, only 17% larger than the flow rate in a secondary fuel port, since there are twice as many primary fuel ports than secondary fuel ports. This leads to a more uniform fuel distribution along the burner circumference under base conditions compared to the operation without secondary fuel (see *y*-marginal plots in Figure 10). However, since the secondary fuel ports are only located in between every other pair of primary fuel ports there is still a significant drop in fuel concentration noticeable where there is no secondary fuel port in between primary fuel ports. The fuel port location of ±22.5° for the primary and 0° for the secondary fuel is under both operational conditions recognizable by peaks in the mixture fraction (i.e., combustion at the fuel-richest compositions). Fuel is consumed at different mixture fractions, ranging from 0.4 to 1.8 and from 0.4 to 2.2 for the base conditions and for the operation without secondary fuel respectively. The marginal plots show in both cases a peak around stoichiometry. However, the peak is narrower for the operation without secondary fuel, ranging from a normalized mixture fraction of 0.8−1.2, compared to the base conditions where a major part of the combustion occurs at normalized mixture fractions between 0.6 and 1.2. Hence, more fuel is consumed at a normalized mixture fraction of 0.6−0.8 when secondary fuel is added.

Figure 11 shows the probability density distribution of the NO_x production rate integrated in the axial direction. The production rate reaches high values in the mixing layers of the fuel jets for both investigated simulations. Almost all NO_x is formed within/next to the inner recirculation zone, at an axial coordinate less than the recirculation zone length of 1.72 D, when the PPBB burner is operated without secondary fuel (see Figure 11b). The marginal plot for the base case simulation on the other hand shows a distribution that falls off more slowly toward higher axial coordinates compared to the case without secondary fuel. This observation corresponds to what was seen in Figure 9 as well. In both cases an elevated NO_x formation rate can be observed in the range of 0.2−1.0 burner diameters downstream of the bluff body independent of the angular position. Supplying fuel to both the primary and secondary fuel ports leads to a more uniform distribution of the NO_x source along the burner circumference.

Figure 12 shows the NO_x formation rate as a contour on the stoichiometric mixture fraction isosurface for the burner operating under base conditions, which gives a better spatial perception of the burner characteristics compared to Figure 11. The NO_x formation in the PPBB burner is dominated by thermal NO_x, as the burner is operated with pure hydrogen at atmospheric pressures. Investigating the stoichiometric isosurface provides, therefore, also an insight into the peak NO_x formation rate, which generally reaches the highest values close to stoichiometric conditions. "Hot spots" of high NO_x formation can be seen in the concave region of the isosurface in between primary and secondary fuel ports.

An important factor affecting NO_x formation is not only the ratio between the reactants (i.e., equivalence ratio) but also the amount of dilution by products. The flow field formed by the PPBB burner contains two characteristic recirculation zones as illustrated in Figure 1. The inner recirculation zone is formed immediately downstream of the bluff body and stabilizes the flame in the turbulent flow field by transporting hot products and radicals upstream toward the flame anchor point at the bluff body trailing edge. The outer recirculation zone is several times larger than the inner recirculation zone and is formed between the burner and the chamber wall. The outer recirculation zone transports flue gas upstream of the bluff body trailing edge where it can be entrained into the wall jet flow which leads to dilution of the partially premixed fuel−air mixture. The amount of recirculation in these two zones is therefore important for both the flame stability as well as the emission characteristics of the burner. Figure 13 shows the recirculated mass flow rates normalized by the total mass flow rate for different operational conditions as a function of the thermal load. The inner recirculation mass flow rate was obtained by numerical integration of the mass flow rate within the recirculation zone (i.e., negative axial velocity) at an axial position of 0.75 D downstream of the bluff body trailing edge. The mass flow rate in the outer recirculation zone was obtained by numerical integration of the mass flow rate which is transported upstream of the bluff body trailing edge. It can be seen that the normalized recirculated mass flow rate increases in the inner recirculation zone and decreases in the

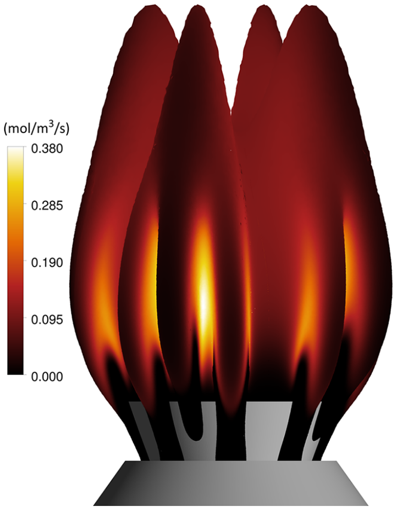

Figure 12. Isosurface of the stoichiometric mixture fraction colored by the NO_x formation rate for the simulation of the PPBB burner operating at base conditions.

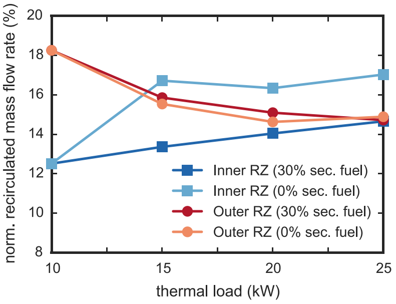

Figure 13. Recirculated mass flow rates normalized by the total mass flow rate in the inner (blue squares) and outer (red circles) recirculation zones with 30% (dark lines) and without (light lines) secondary fuel for different thermal loads.

outer recirculation zone with increasing heat load. The amount of secondary fuel has a stronger impact on the inner recirculation zone compared to the outer recirculation zone, where the effect of the secondary fuel is negligible compared to the effect of the thermal load.

4. DISCUSSION

The discussion is divided into two subsections, following the same structure as the Results section. The first subsection, *Discussion of the Model Performance*, addresses the performance of the CFD model in terms of the quantitative and qualitative accuracy of its global NO_x predictions. The second subsection, *Discussion of the Burner Characteristics*, deals with the combustion qualities of the burner and aims at the understanding of the processes that govern NO_x formation.

4.1. Discussion of the Model Performance.

The boundary conditions of the PPBB burner, especially the thermal boundary conditions, are subject to large uncertainties due to limited experimental data as discussed in section 2.4. The global NO_x emissions have furthermore been shown to dependent linearly on the bluff body surface temperature for the investigated temperature range. This diminishes the importance of the absolute deviation between simulation and experiment. All simulations with a thermal input equal to 25 kW would coincide, within a negligible margin, with the experiments if the base case boundary conditions would have been adjusted accordingly. The same is true for simulations without secondary fuel. However, adjusting the unknown temperature boundary conditions will not improve the scatter that can be seen for the 10 kW simulations and the simulations with 30% secondary fuel in Figure 5.

The conducted simulations have indicated that capturing the effect of a varying thermal load on the NO_x emissions is less demanding for the numerical model than the effect of a varying secondary fuel fraction. Global properties, such as the flame surface to flame volume ratio, heat losses to the chamber walls, as well as the recirculated mass flow rates in the outer recirculation zone (see Figure 13) were affected by an increasing thermal input. However, they remained mostly close to constant for varying secondary fuel fractions at a given thermal input. Hence, secondary fuel appears to have a more localized (i.e., mainly affecting the inner recirculation zone) and mixing related effect on the combustion which is more demanding for the applied turbulence and combustion models. Especially the inverted trend for the 10 kW simulations shows the challenging physics of hydrogen combustion. Even though the employed CFD model takes binary mass diffusion via a modified Chapman−Enskog formulation into account, the turbulent mixing is still based on a constant turbulent Schmidt number. The fine scale quantities of the EDC model are furthermore only related to turbulence properties and hence do not account for variable Schmidt or Lewis numbers either. This may impact the simulation results, even more so at the base thermal load, as the turbulent levels are lower under these conditions compared to a thermal load of 25 kW, which makes the mixing and combustion processes more sensitive to variable Schmidt and Lewis numbers. Gabriel et al.[44] has for example shown that the fuel Lewis number can, under certain conditions, compensate for the decreased flame temperature that can be achieved by dilution. Dilution by internally recirculated flue gas is one of the mechanisms that are employed in the PPBB burner to mitigate NO_x emissions.

Generally better results, in terms of NO_x trends, were achieved for the 25 kW simulations compared to the 10 kW simulations. The flow rates at 10 kW load led to low Reynolds numbers in wide areas of the combustion chamber which can be more challenging for the $k-\epsilon$ model, the EDC model as well as the employed wall functions. The lower velocities furthermore caused the flame to stabilize further upstream, toward high strain regions where quenching could be expected. This was especially the case for simulations without secondary fuel and is a limitation inherent to the EDC model, which tends to overpredict reaction rates under this circumstances. The EDC model proposed by Magnussen[25] and Gran and Magnussen[45] contains the quantity χ which denotes the fraction of the fine structure that reacts. This quantity was proposed to model the probability of finding the reactants together, to model the degree of preheating by products, and to limit the reactions due to the lack of reactants. Hence, the overall reaction rate in a CFD cell is reduced for $\chi < 1$. However, the fraction of reacting fine structure is not implemented in ANSYS Academic Fluent, Release 18.2 based on the assumption of $\chi = 1$. The actual distribution of χ for the base case simulation was therefore calculated as a postprocessing quantity and has been shown to be generally smaller than unity. The assumption of $\chi = 1$ is therefore likely contributing to the flame stabilization relatively far upstream of the PPBB burner. However, in order to conclude definitively on this, one would need to calculate the fraction of reacting fine structure in conjunction with the solution of the other EDC quantities. The impact of the assumption of $\chi = 1$ on the NO_x formation requires therefore further investigation.

4.2. Discussion of the Burner Characteristics.

The regime diagram shown in the results (i.e., Figure 8) demonstrates the different nature of secondary and primary fuel, where one burns closely to stoichiometry while the other is consumed at a wider and generally leaner range of mixture fractions. This difference is related to the location of the fuel ports. The secondary fuel ports are closer to the trailing edge of the burner/flame anchor point than the primary fuel ports. The mixing time for secondary fuel is accordingly shorter than for primary fuel, which leads to an enriched inner recirculation zone. Another factor is their relation to the burner throat. Figure 9 shows how primary fuel is premixed in the cross-flow in the converging section upstream of the burner throat. The mixture is then further downstream accumulated within the wall jet that is formed due to the narrow throat. Secondary fuel on the other hand has the potential to penetrate the wall jet to some degree, since the fuel ports are located outside of the burner housing. This leads to secondary fuel being transported partially past the inner recirculation zone; enriching the immediate post flame.

Figure 9 shows a correlation between mixture fraction and NO_x formation rate. This correlation is related to the dominance of thermal NO_x which is highly temperature dependent and therefore also affected by changes in the mixture fraction. Another important NO_x route for hydrogen combustion is the N_2O-intermediate mechanism, which is less temperature sensitive. However, this mechanism is strongly pressure dependent due to the involved three-body reaction and therefore of less relevance for the PPBB burner which operates at atmospheric pressure. NO_x formation via the prompt and the NNH mechanism are not relevant for the PPBB burner when operated with pure hydrogen due to the lack of carbon in the mixture. Considering that the adiabatic

DOI: 10.1021/acs.energyfuels.9b00313
Energy Fuels 2019, 33, 4598−4610

flame temperature reaches its maximum close to stoichiometry and falls of to both the fuel-lean and -rich sides, one can expect that operational conditions which lead to a wider spread in the mixture fraction will consequently also lead to lower NO_x formation. The variance in mixture fraction can be seen in the x-marginal plot of Figure 10, which shows the PDF of the progress variable source term in the normalized mixture fraction space. The lean limit of the PDF is the same for both simulations. However, the rich limit is higher when the PPBB burner is operated without secondary fuel. Note that the primary fuel has a higher momentum when there is no secondary fuel since more fuel needs to pass through the primary fuel ports. The PDF of the progress variable source term reaches overall the highest values at a normalized mixture fraction ranging from 0.7 to 1.1 in between 4° and 13° absolute angular position, which is adjacent to the secondary fuel stream. This corresponds to the concave region of the stoichiometric isosurface which is formed by the primary and secondary fuel streams (see Figure 12). At this location the stoichiometric isosurface is close to the inner recirculation zone which leads to the entrainment of hot recirculated products into the air−fuel stream. This causes locally higher temperatures and radical concentration compared to the convex area of the isosurface where colder flue gas from the outer recirculation zone is entrained and leads in combination with the stoichiometric mixture to an increase in NO_x formation rate. The peaks in NO_x production can also be seen in Figure 11, which in addition provides insight into the PDF of the NO_x formation along the angular and axial coordinates.

Employing the secondary fuel ports not only affects the inner recirculation zone in terms of mixture fraction (i.e., transition from fuel lean to fuel rich) but consequently also alters the recirculated mass flow rate within the recirculation zone (see Figure 13). Secondary fuel furthermore enters the chamber with a negative axial velocity component, while the mass flow rate in the throat is decreased as less fuel is provided by the primary fuel ports. Overall this leads to a decrease in the recirculated mass flow rate when secondary fuel is used. The outer recirculation zone contains on the other hand flue gas with a composition close to the global mixture fraction and is hence less affected by a change in the secondary fuel fraction. Increasing the thermal load affects both recirculation zones. The normalized recirculated mass flow rate in the outer recirculation zone decreases with increasing heat load. This is expected to also reduce the effect of dilution on the NO_x formation (i.e., NO_x emissions are expected to increase), which corresponds to the trend that was observed in both the experiments and simulations.

5. CONCLUSION

Twelve CFD simulations of the PPBB burner were conducted covering different operational conditions with regard to thermal load and secondary fuel fraction. All simulations were compared to experimental data obtained by Dutka et al.[9] The deviation between predicted and measured NO_x emissions was within +10% and −18%. The CFD simulations underpredicted the NO_x emissions on average by 7%. For the base case configuration of 10 kW thermal load and 30% secondary fuel fraction a set of additional simulations was performed to investigate the sensitivity of the NO_x emissions to the thermal boundary conditions. The CFD model was able to capture the dependence of the NO_x emission on the thermal load. The impact of secondary fuel on the emissions was, however, only captured for a thermal load of 25 kW.

A detailed analysis of the combustion characteristics was conducted showing that especially primary fuel is burned in a premixed and nonpremixed mode. Multiple combustion regimes exist in both modes, however, the premixed mixing mode leads to a larger regime variation which was shown in a CFD based combustion diagram. Varying combustion regimes and mixing modes are not untypical for partially premixed systems. However, the variation is likely stronger in the investigated bluff body burner compared to typical swirl burners. The stronger angular mass transport in a swirl burner will smooth gradients caused by the arrangement of the fuel ports.

Employing secondary fuel leads to a more uniform distribution of the fuel along the burner circumference. However, secondary fuel is less premixed than primary fuel due to the shorter distance of the secondary fuel ports to the flame anchor point. Hence, the study has proven that secondary fuel can be utilized to enrich the inner recirculation zone with the intention of increased flame stability. The fuel-rich conditions in the inner recirculation zone, when 30% secondary fuel is provided, shift the NO_x formation further downstream toward the immediate postflame region and lead to a lower NO_x formation rate within the recirculation zone itself. Employing secondary fuel leads furthermore to a decrease of the normalized recirculated mass flow rate in the inner recirculation zone. The effect on the outer recirculation zone is minor. The normalized recirculated mass flow rate in the inner recirculation zone decreases also when the thermal load is decreased, while the normalized recirculated mass flow rate in the outer recirculation zone increases in this case. This affects consequently the amount of dilution by the recirculated flue gas.

The NO_x formation in the PPBB burner is dominated by thermal NO_x, as the burner is operated with pure hydrogen at atmospheric pressures. The formation rate of thermal NO_x is generally highest close to stoichiometric conditions. The highest NO_x formation rate, for the operation of the PPBB burner at base conditions, is located in the concave region of the stoichiometric isosurface which is formed by the mean curvature of the isosurface in between primary and secondary fuel ports. The elevated temperature and radical concentration in this region, caused by the mixing with hot products from the inner recirculation zone, in conjunction with a mixture fraction around stoichiometry promote the formation of thermal NO_x. In contrary to the PPBB burner, these NO_x peaks are not expected for fully premixed burners or burners with a strong angular momentum, such as swirl burners, which have a more uniform mixture profile in the angular direction. This finding raises the question if a different fuel port distribution and/or fuel port count could lead to a reduction of the NO_x formation. The effect of different fuel port configurations should, therefore, be investigated further.

■ AUTHOR INFORMATION

Corresponding Author

*E-mail: christoph.meraner@ntnu.no.

ORCID

Christoph Meraner: 0000-0002-3445-8074
Tian Li: 0000-0002-4248-8396

Notes

The authors declare no competing financial interest.

■ ACKNOWLEDGMENTS

This publication has been produced with support from the BIGCCS Centre, performed under the Norwegian Research Program Centres for Environment-Friendly Energy Research (FME). The authors acknowledge the following partners for their contributions: Gassco, Shell, Statoil, TOTAL, ENGIE, and the Research Council of Norway (193816/S60). The CFD simulations were performed on resources provided by UNINETT Sigma2 - the National Infrastructure for High Performance Computing and Data Storage in Norway.

■ REFERENCES

(1) Glarborg, P.; Miller, J. A.; Ruscic, B.; Klippenstein, S. J. Modeling nitrogen chemistry in combustion. *Prog. Energy Combust. Sci.* **2018**, *67*, 31−68.

(2) *Nitrogen Oxides (NOx), Why and How They Are Controlled*; Environmental Protection Agency, 1999.

(3) Cormos, C.-C. Economic implications of pre- and post-combustion calcium looping configurations applied to gasification power plants. *Int. J. Hydrogen Energy* **2014**, *39*, 10507−10516.

(4) Cormos, C.-C. Evaluation of power generation schemes based on hydrogen-fueled com- bined cycle with carbon capture and storage (CCS). *Int. J. Hydrogen Energy* **2011**, *36*, 3726−3738.

(5) Zeldovich, Y. B. The oxidation of nitrogen in combustion and explosions. *Acta Physicochimica U.R.S.S.* **1946**, *21*, 577−628.

(6) Lieuwen, T.; McDonell, V.; Petersen, E.; Santavicca, D. Fuel Flexibility Influences on Premixed Combustor Blowout, Flashback, Autoignition, and Stability. *J. Eng. Gas Turbines Power* **2008**, *130*, No. 011506.

(7) Noble, D. R.; Zhang, Q.; Shareef, A.; Tootle, J.; Meyers, A.; Lieuwen, T. Syngas Mixture Composition Effects upon Flashback and Blowout. In *Proceedings of ASME Turbo Expo*; Barcelona, Spain, 2006; The American Society of Mechanical Engineers, 2006; pp 1−12.

(8) Spangelo, Ø.; Sonju, O.; Slungaard, T.; Ditaranto, M. U.S. 20090220899 A1, 2009.

(9) Dutka, M.; Ditaranto, M.; Løvås, T. NOx emissions and turbulent flow field in a partially premixed bluff body burner with CH4 and H2 fuels. *Int. J. Hydrogen Energy* **2016**, *41*, 12397−12410.

(10) Lieuwen, T.; McDonell, V.; Santavicca, D.; Sattelmayer, T. Burner Development and Operability Issues Associated with Steady Flowing Syngas Fired Combustors. *Combust. Sci. Technol.* **2008**, *180*, 1169−1192.

(11) Dam, B.; Corona, G.; Hayder, M.; Choudhuri, A. Effects of syngas composition on combustion induced vortex breakdown (CIVB) flashback in a swirl stabilized combustor. *Fuel* **2011**, *90*, 3274−3284.

(12) Wohl, K. Quenching, flash-back, blow-off-theory and experiment. *Symp. (Int.) Combust., [Proc.]* **1953**, *4*, 68−89.

(13) Davu, D.; Franco, R.; Choudhuri, A.; Lewis, R. Investigation on Flashback Propensity of Syngas Premixed Flames. In *41st AIAA/ASME/SAE/ASEE Joint Propulsion Conference & Exhibit*; AIAA: Reston, Virigina, 2005; pp 1−11.

(14) Lewis, B.; Von Elbe, G. *Combustion, Flames, and Explosions of Gases*; Academic Press, 1987.

(15) Meraner, C.; Li, T.; Ditaranto, M.; Løvås, T. Cold flow characteristics of a novel bluff body hydrogen burner. *Int. J. Hydrogen Energy* **2018**, *43*, 7155−7168.

(16) Dutka, M.; Ditaranto, M.; Løvås, T. Emission characteristics of a novel low NO_x burner fueled by hydrogen-rich mixtures with methane. *J. Power Technol.* **2015**, *95*, 105−111.

(17) Dutka, M.; Ditaranto, M.; Løvås, T. Investigations of air flow behavior past a conical bluff body using particle imaging velocimetry. *Exp. Fluids* **2015**, *56*, 199.

(18) Meares, S.; Masri, A. R. A modified piloted burner for stabilizing turbulent flames of inhomogeneous mixtures. *Combust. Flame* **2014**, *161*, 484−495.

(19) Pope, S. B. Small scales, many species and the manifold challenges of turbulent combustion. *Proc. Combust. Inst.* **2013**, *34*, 1−31.

(20) Veynante, D.; Vervisch, L. Turbulent combustion modeling. *Prog. Energy Combust. Sci.* **2002**, *28*, 193−266.

(21) Haworth, D. Progress in probability density function methods for turbulent reacting flows. *Prog. Energy Combust. Sci.* **2010**, *36*, 168−259.

(22) Echekki, T., Mastorakos, E., Eds. *Turbulent Combustion Modeling*; Fluid Mechanics and Its Applications; Springer Netherlands: Dordrecht, 2011; Vol. *95*.

(23) Fiorina, B.; et al. Challenging modeling strategies for LES of non-adiabatic turbulent stratified combustion. *Combust. Flame* **2015**, *162*, 4264−4282.

(24) Spalding, D. Mixing and chemical reaction in steady confined turbulent flames. *Symp. (Int.) Combust., [Proc.]* **1971**, *13*, 649−657.

(25) Magnussen, B. On the structure of turbulence and a generalized eddy dissipation concept for chemical reaction in turbulent flow. In *19th Aerospace Sciences Meeting*; AIAA: Reston, Virginia, 1981; pp 1−6.

(26) Magnussen, B.; Hjertager, B. On mathematical modeling of turbulent combustion with special emphasis on soot formation and combustion. *Symp. (Int.) Combust., [Proc.]* **1977**, *16*, 719−729.

(27) Barth, T.; Jespersen, D. The design and application of upwind schemes on unstructured meshes. In *27th Aerospace Sciences Meeting*; AIAA: Reston, Virginia, 1989; pp 1−12.

(28) Hutchinson, B. R.; Raithby, G. D. A multigrid method based on the additive correction strategy. *Numerical Heat Transfer* **1986**, *9*, 511−537.

(29) Anderson, W.; Bonhaus, D. L. An implicit upwind algorithm for computing turbulent flows on unstructured grids. *Comput. Fluids* **1994**, *23*, 1−21.

(30) Issa, R. Solution of the implicitly discretised fluid flow equations by operator-splitting. *J. Comput. Phys.* **1986**, *62*, 40−65.

(31) Ferziger, J. H.; Peric, M.; *Computational Methods for Fluid Dynamics*; Springer: Berlin, Heidelberg, 2002.

(32) Shih, T.-H.; Liou, W. W.; Shabbir, A.; Yang, Z.; Zhu, J. A new k-epsilon eddy viscosity model for high reynolds number turbulent flows. *Comput. Fluids* **1995**, *24*, 227−238.

(33) Kim, S.-E.; Choudhury, D. A Near-Wall Treatment Using Wall Functions Sensitized to Pressure Gradient. *ASME Publications-FED* **1995**, *217*, 273−280.

(34) Li, J.; Zhao, Z.; Kazakov, A.; Dryer, F. L. An updated comprehensive kinetic model of hydrogen combustion. *Int. J. Chem. Kinet.* **2004**, *36*, 566−575.

(35) *Documentation, Theory Guide*; ANSYS Inc., 2017; pp 1−850.

(36) McGee, H. A., Jr. *Molecular Engineering*, 1st ed.; McGraw-Hill: New York, 1991; p 480.

(37) Argyropoulos, C.; Markatos, N. Recent advances on the numerical modelling of turbulent flows. *Applied Mathematical Modelling* **2015**, *39*, 693−732.

(38) Guiberti, T.; Durox, D.; Scouflaire, P.; Schuller, T. Impact of heat loss and hydrogen enrichment on the shape of confined swirling flames. *Proc. Combust. Inst.* **2015**, *35*, 1385−1392.

(39) Euler, M.; Zhou, R.; Hochgreb, S.; Dreizler, A. Temperature measurements of the bluff body surface of a Swirl Burner using phosphor thermometry. *Combust. Flame* **2014**, *161*, 2842−2848.

(40) Michaels, D.; Ghoniem, A. F. Impact of the bluff-body material on the flame leading edge structure and flame−flow interaction of premixed CH_4/air flames. *Combust. Flame* **2016**, *172*, 62−78.

(41) Merk, H. J. The macroscopic equations for simultaneous heat and mass transfer in isotropic, continuous and closed systems. *Appl. Sci. Res.* **1959**, *8*, 73−99.

(42) Peters, N. The turbulent burning velocity for large-scale and small-scale turbulence. *J. Fluid Mech.* **1999**, *384*, 107.

(43) Goodwin, D. G.; Speth, R. L.; Moffat, H. K.; Weber, B. W. *Cantera: An Object-Oriented Software Toolkit for Chemical Kinetics, Thermodynamics, and Transport Processes*, Version 2.4.0; 2018 https://cantera.org/.

(44) Gabriel, R.; Navedo, J. E.; Chen, R.-H. Effects of fuel Lewis number on nitric oxide emission of diluted H_2 turbulent jet diffusion flames. *Combust. Flame* **2000**, *121*, 525−534.

(45) Gran, I. R.; Magnussen, B. F. A numerical study of a bluff-body stabilized diffusion flame. Part 2. Influence of combustion modeling and finite-rate chemistry. *Combust. Sci. Technol.* **1996**, *119*, 191−217.

Paper III

Effects of scaling laws on the combustion and NO_x characteristics of hydrogen burners

Christoph Meraner, Tian Li, Mario Ditaranto, Terese Løvås

Submitted to Combustion and Flame

Effects of scaling laws on the combustion and NO_x characteristics of hydrogen burners

Christoph Meraner[a,*], Tian Li[a], Mario Ditaranto[b], Terese Løvås[a]

[a] *Department of Energy and Process Engineering, Faculty of Engineering, NTNU Norwegian University of Science and Technology, Trondheim, Norway*
[b] *SINTEF Energy Research, Trondheim, Norway*

Abstract

The effect of constant velocity and constant residence time scaling on the local nitric oxide (NO_x) emissions and flame characteristics of complex partial premixed hydrogen burners were investigated numerically and theoretically. A previously developed and validated computational fluid dynamic (CFD) model was employed to conduct in total 11 simulations at various burner scales ranging from 10 kW to 500 kW. The flame characteristics were investigated by means of a novel CFD based regime diagram and compared to Damköhler and Karlovitz numbers obtained from scaling theory. The flame is at laboratory scale mainly characterized by the thin reaction zone regime. Employing constant velocity scaling was predicted to overall decrease the Karlovitz number, which causes the combustion to appear partially in the corrugated flamelet regime and at scales exceeding 250 kW also in the wrinkled flamelet regime. Constant residence time scaling on the other hand preserves the overall Damköhler number. However, a significant part of the flame, mainly close to stoichiometry, appears to follow a constant Karlovitz number. Both investigated scaling principles lead to an increase of the overall NO_x emissions, with constant velocity scaling resulting in the highest emissions. This is mainly attributed to the larger volumes and longer residence times of the flame and immediate post flame region compared to constant residence time scaling. The total NO_x formation in the

---

[*] Corresponding author
Email address: `christoph.meraner@ntnu.no` (Christoph Meraner)

inner recirculation zone, on the other hand, is lower for constant velocity scaling and is found to be dominated by the local oxygen atom (O) and hydroxyl (OH) concentration. Constant velocity scaling causes a breakup of the inner recirculation zone at the 500 kW scale, which leads to a fundamentally different flow field and causes the flame to impinge onto the combustion chamber wall, whereas constant residence time scaling preserves the inner recirculation zone at all investigated scales. The breakup of the recirculation zone is attributed to the different effect of the scaling principles on the velocity to length scale ratio and momentum of the annular jet flow.

Keywords: scaling, NO_x emission, hydrogen, partially premixed burner, combustion regime diagram

Nomenclature

Symbols

A, A', B_1, B_2, C, C'	markers
D	diameter (m)
K	proportionality constant (-)
k	turbulent kinetic energy (m^2 s^{-2})
L_{IRZ}	inner recirculation zone length(m)
l	length scale (m)
l'	turbulent length scale (m)
Q	thermal input (W)
S_L	laminar flame speed (m s^{-1})

U	velocity (m s^{-1})
u	cartesian velocity component (m s^{-1})
u'	turbulent velocity scale (m s^{-1})
Y	mass fraction (-)
y	spacial coordinate (m)

Greek

β	scaling factor (-)
δ_L	laminar flame thickness (m)
ϵ	dissipation rate (m^2 s^3)
η_k	Kolmogorov length scale (m)
ν	kinematic viscosity (m^2 s^{-1})
ρ	density (kg m^{-3})
τ_c	chemical time scale (s)
τ_k	Kolmogorov time scale (s)
τ_T	turbulent time scale (s)

Dimensionless groups

Da	Damköhler number
Ka	Karlovitz number

Re	Reynolds number

Subscript

0	burner characteristic
ax	axial direction
rt	constant residence time
v	constant velocity

Superscript

*	scaled
eq	chemical equilibrium

Abbreviations

CFD	computational fluid dynamic
EDC	eddy dissipation concept
FL	flame
IPF	immediate post flame
IRZ	inner recirculation zone
MILD	moderate or intense low-oxygen dilution
$\mathrm{NO_x}$	nitric oxide
ORZ	outer recirculation zone

PDF	probability density function
PF	post flame
PPBB	partially premixed bluff body
RANS	Reynolds averaged Navier-Stokes
WJ	wall jet

1. Introduction

Increasingly stringent regulations on emissions from stationary power and heat production has motivated the development of various low emission technologies, including carbon capture and storage units, flexi-fuel units enabling the use of non-carbon containing fuels such as hydrogen and recently ammonia [1], and various low and ultra low $\mathrm{NO_x}$ burners over the last decades. For the latter, dry low emission (DLE) combustion has traditionally been the most common used technology to reduce $\mathrm{NO_x}$ emissions [2]. DLE combustion is dependent on highly controlled mixing of air and fuel to achieve lean premixed combustion, thereby reducing the flame temperature and hence reducing $\mathrm{NO_x}$ formation. The staged fuel gas injection environmental (EV) burner from Alstom [3] is one example of DLE burners. Due to the reduced temperatures, special considerations have to be made, to ensure an environment that at the same time does not promote unacceptable levels of unburnt hydrocarbons and carbon monoxide (CO), as well as combustion instabilities. When considering high hydrogen content fuels, other issues come into play. Higher burning velocities and temperatures need to be carefully controlled by design optimization to avoid flashbacks. As a result, burners with complex flow regimes have been proposed. This involves for example swirl burners [4], flamesheet burners [5], micro-mixing burners [6] and recently partially premixed bluff body burners [7, 8]. Common for these burners are highly optimized flows and complex designs in order to obtain optimum low emission, yet efficient operation.

The high cost associated with the development process of such complex burners motivates experiments and numerical simulations at laboratory scale. This requires scaling of the burner geometry by employing scaling laws that preserve the burner characteristics at different burner sizes. However, the large number of scaling parameters found through similarity theory, many of them mutually incompatible, makes a complete scaling practically impossible. Scaling problems are therefore treated by the use of partial scaling, which has been reviewed in detail by Spalding et al. [9] and Beér [10]. Thus a variety of different scaling laws can be found in literature, the majority of which have been developed for "simple" axisymmetric, turbulent, jet flames, which provide a well-defined flow field [11].

The first studies concerning the scalability of NO_x emissions aimed to develop scaling laws based on equilibrium conditions for temperature and oxygen atom (O) concentration such as the study by Lavoie and Schlander [12] and the asymptotic analysis by Peters [13]. However, flame stretch can lead to a significant departure from equilibrium conditions, as has been shown by Drake and Blint [14] in laminar opposed-flow diffusive flames. Barlow and Carter [15, 16] performed simultaneous, time-resolved measurements of major species, mixture fraction, temperature, hydroxyl (OH) and nitric oxide (NO) concentrations in non-premixed turbulent hydrogen jet flames, which provided further insight into the relation between non-equilibrium conditions and NO formation. Various scaling models have, therefore, been proposed that consider non-equilibrium conditions. One of the first studies that showed improved model accuracy by including non-equilibrium O-atom concentrations related to the fine scale turbulent fluctuations, is the work by Kent and Bilger [17]. Chen and Kollmann [18] employed a probability density function approach to investigate the effects of non-equilibrium chemistry and radiative heat losses on thermal NO formation. Their study confirmed the finding of Chen and Driscoll [19] that NO_x emissions are characterized by a negative one-half power dependency on the flame Damköhler number. The same dependency was found by Smith et al. [20], in addition to an increased model accuracy, by employing a conditional moment closure approach. Szego et al. [21] suggested that, under certain conditions, all parameters affecting global

NO_x emissions can be characterized by a global residence time and furnace temperature as proposed by Turns et al. [22, 23], following the hypothesis that a majority of the NO_x emissions are formed in large and nearly homogeneous eddies [24].

The scaling law proposed by Røkke et al. [25] is one of few studies regarding NO_x emissions from partially premixed flames and was re-evaluated by Santos and Costa [26] for turbulent diffusion flames. Weber [27] concluded the effect of flue gas entrainment, from internal and external flue gas recirculation, and the radiation heat loss in the post flame need to be included in order to make the correlation by Røkke et al. [25] applicable to industrial burners. A recent study by Joo et al. [28] employed an artificial neural network to develop a predictive model for NO_x emissions from partially premixed flames. However, the model accuracy of this novel approach could not yet match the accuracy of established empirical models.

Although the above presented models provide a valuable and fundamental understanding of NO_x formation in turbulent flames, their application for the scaling of complex systems, such as the previously discussed burners, is limited [27, 29]. Typically only two scaling laws are considered for industrial burners; namely constant velocity (i.e., $U_0 = const.$) and constant residence time scaling (i.e., $D_0/U_0 = const.$) [30]. Both approaches are based on the basic global equation for the thermal input:

$$Q = K\rho_0 U_0 D_0^2, \tag{1}$$

where K is a proportionality constant, ρ_0 the inlet fluid density, D_0 the characteristic burner length scale and U_0 the characteristic burner velocity. They, furthermore, demand geometrical similarity, hence all dimensions can be derived from the scaled characteristic burner length scale, D_0^*, and assume that the Reynolds and Froude number are sufficiently large, so that the burner flow is turbulent and momentum controlled at all relevant scales.

An important work regarding constant velocity scaling was conducted in the SCALING 400 project [31] which led to an extensive data set for the NO_x emission performance of swirl burners in the range of 30 kW to 12 MW thermal input. The project was later extended to constant residence time scaling by means of numerical simulations [32]. Weber and Breussin [33], and Bollettini et al. [32] concluded that none of the two approaches is superior over the other, while Megalos et al. [34] found constant velocity scaling more suitable for pulverized coal flames. Ballester et al. [35] proposed a scaling law in-between constant velocity and constant residence time scaling, relating the thermal load to the burner diameter to the power of 2.3–2.6, and presented good results for the scaling of a natural gas swirl burner from 0.3 MW to 13.8 MW. Smart and Van Kamp [36] on the other hand found that neither constant velocity nor constant residence time scaling where able to preserve flame structures and thermochemical fields adequately in a pulverised coal burner, when scaled from 2.5 MW to 12 MW. Furthermore, their study indicated the existence of a minimum scale which is still representative for a full-scale burner and showed that both scaling laws lead to a weakening of the inner recirculation zone.

Constant residence time scaling is often studied, but rarely employed for industrial applications as it leads to high velocities that scale proportional to a cube-root law and, hence, lead to excessive pressure drops. Other approaches, such as the scaling law more recently proposed by Cole et al.[37], which also considers the scaling effect on acoustic frequencies and scales the velocity proportional to a square-root law, suffer from the same issue. Kumar et al. [38] aims to solve this problem by prescribing an upper limit for the air injection velocity while still following the constant residence time scaling for the characteristic burner length scale. However, this approach violates the fundamental idea of constant residence time scaling, as the ratio D_0/U_0 is not constant. Furthermore, the generalizability of such an approach, developed for moderate or intense low-oxygen dilution (MILD) combustion, is limited.

Only a limited number of studies regarding the scalability of complex burners is found in the literature and the majority of these studies are focusing on global aspects of the burner characteristics, such as the total NO_x and CO emissions, flame length or coal-burnout. Few studies investigate scaling effects in different burner regions specifically and treat these regions individually [29, 39]. It is however expected that scaling of modern burners, following the constant velocity or the constant residence time approach, will exhibit local scaling effects due to the complex nature of the burner designs, which is not adequately represented by a single length and velocity scale [29]. The objective of the present work is to develop a deeper understanding of the scaling effects on the flame structure in different regions of complex modern burners. The study case presented is a partially premixed bluff body (PPBB) burner which consists of inner and outer recirculation zones, stagnation point, staged fuel injection and varying degree of partial premixing. The impact of different scaling laws on the combustion regimes and $\mathrm{NO_x}$ emissions performance of this complex burner are investigated with hydrogen as fuel. The scope comprises furthermore the identification of potentially critical thermal loads that may limit the scalability of the burner, which have for example been found for the scaling of pulverized coal [33] and natural gas burners [32].

The scaling effects are investigated based on a set of 11 computational fluid dynamic (CFD) simulations at different scales up to a thermal load of 500 kW. The paper presents first the impact of the scaling approaches on the combustion characteristics in general. This is done by means of combustion regime diagrams combined with hexagon binning and the analysis of the progress variable source term distribution. In addition to the CFD based results theoretical considerations are presented. Finally the work focuses on $\mathrm{NO_x}$ emissions and scrutinizes the contribution of different flow regions to the $\mathrm{NO_x}$ formation.

2. Methodology

2.1. Scaling

In what follows is the examination of the effect of constant velocity and constant residence time scaling on macro- and micro-mixing in terms of Damköhler and Karlovitz number, following the considerations made by Farcy et al. [40]. Given geometric similarity, all burner length scales, l, are increased by a factor, $\beta > 1$, when the burner is scaled up from laboratory scale to larger thermal loads:

$$l^* = \beta l, \tag{2}$$

where the star superscript represents scaled properties. For the following considerations it is furthermore assumed that the turbulent intensity stays unchanged for both scaling approaches.

2.1.1. Constant velocity scaling

By keeping the characteristic velocity, U_0, constant and considering equation (1) the scaled burner diameter, for constant velocity scaling, can be derived from the following relation:

$$\frac{D^*_{0,v}}{D_0} \propto \left(\frac{Q^*_v}{Q}\right)^{1/2}, \tag{3}$$

which leads to a scaling factor of:

$$\beta_v = \left(\frac{Q^*_v}{Q}\right)^{1/2}. \tag{4}$$

Since the velocity scale is unchanged, $u^*_v = u$, and all length scales are scaled up, $l^*_v = \beta_v l$, we obtain:

$$k_v^{*1/2} \approx {l'_v}^* \left|\frac{\partial u^*_v}{\partial y^*_v}\right| = \beta_v l' \left|\frac{1}{\beta_v}\frac{\partial u}{\partial y}\right| = k^{1/2}, \tag{5}$$

where k is the turbulent kinetic energy. Furthermore we see that the turbulent Reynolds number, Re_T, scales with the factor β_v:

$$Re^*_{T,v} = \frac{k_v^{*1/2} {l'_v}^*}{\nu} = \frac{k^{1/2}\beta_v l'}{\nu} = \beta_v Re_T, \tag{6}$$

the Kolmogorov scale, η_k, scales with the factor $\beta_v^{1/4}$:

$$\eta^*_{k,v} \approx \frac{{l'_v}^*}{{Re^*_{T,v}}^{3/4}} = \frac{\beta_v l'}{(\beta_v Re_T)^{3/4}} = \beta_{rt}^{1/4}\eta_k, \tag{7}$$

and the dissipation rate, ϵ, scales with the factor β_v^{-1}:

$$\epsilon^*_v \approx \frac{\nu^3}{{\eta^*_{k,v}}^4} = \frac{\nu^3}{{(\beta_v^{1/4}\eta_k)}^4} = \frac{1}{\beta_v}\epsilon. \tag{8}$$

As a result, the turbulent time scale, τ_T, scales with the factor β_v:

$$\tau^*_{T,v} = \frac{k^*_v}{\epsilon^*_v} = \frac{k}{\beta_v^{-1}\epsilon} = \beta_v \tau_T, \tag{9}$$

and the Kolmogorov time scale, τ_k, with the factor $\beta_v^{1/2}$:

$$\tau^*_{k,v} = \left(\frac{\nu}{\epsilon^*_v}\right)^{1/2} = \left(\frac{\nu}{\beta_v^{-1}\epsilon}\right)^{1/2} = \beta_v^{1/2}\tau_k. \tag{10}$$

The scaling relation for the Damköhler number is thus:

$$Da^*_v = \frac{\tau^*_{T,v}}{\tau^*_{c,v}} = \frac{\beta_v \tau_T}{\tau_c} = \beta_v Da, \tag{11}$$

and for the Karlovitz number:

$$Ka^*_v = \frac{\tau^*_{c,v}}{\tau^*_{k,v}} = \frac{\tau_c}{\beta_v^{1/2}\tau_k} = \frac{1}{\beta_v^{1/2}} Ka. \tag{12}$$

Substituting β_v with equation (4) leads to:

$$Da^*_v = \left(\frac{Q^*_v}{Q}\right)^{1/2} Da, \tag{13}$$

and

$$Ka^*_v = \left(\frac{Q^*_v}{Q}\right)^{-1/4} Ka. \tag{14}$$

2.1.2. Constant residence time scaling

The objective of constant residence time scaling is to preserve the convective timescale, which represents the residence time for simple flames, by maintaining the ratio D_0/U_0 constant and hence preserving in theory the macro-mixing characteristics of a burner [27, 30]. Obeying this requirement gives together with the basic equation (1), the relationship:

$$\frac{D^*_{0,rt}}{D_0} \propto \left(\frac{Q^*_{rt}}{Q}\right)^{1/3}, \tag{15}$$

and the scaling factor for constant residence time scaling:

$$\beta_{rt} = \left(\frac{Q^*_{rt}}{Q}\right)^{1/3}. \tag{16}$$

Additionally to the length scales also the velocity needs to be scaled up, $u^*_{rt} = \beta_{rt} u$, in order to preserve the residence time, which leads to:

$${k^*_{rt}}^{1/2} \approx {l'_{rt}}^* \left|\frac{\partial u^*_{rt}}{\partial y^*_{rt}}\right| = \beta_{rt} l' \left|\frac{\beta_{rt}}{\beta_{rt}}\frac{\partial u}{\partial y}\right| = \beta_{rt} k^{1/2}, \tag{17}$$

or equivalently

$$k^*_{rt} = \beta^2_{rt} k. \tag{18}$$

Here the turbulent Reynolds number, Re_T, scales with the factor β^2_{rt}:

$$Re^*_{T,rt} = \frac{{k^*_{rt}}^{1/2} {l'_{rt}}^*}{\nu} = \frac{\beta_{rt} k^{1/2} \beta_{rt} l'}{\nu} = \beta^2_{rt} Re_T, \tag{19}$$

the Kolmogorov scale, η_k, scales with the factor $\beta^{-1/2}_{rt}$:

$$\eta^*_{k,rt} \approx \frac{{l'_{rt}}^*}{{Re^*_{T,rt}}^{3/4}} = \frac{\beta_{rt} l'}{(\beta^2_{rt} Re_T)^{3/4}} = \frac{1}{\beta^{1/2}_{rt}} \eta_k, \tag{20}$$

and the dissipation rate, ϵ, scales with the factor β^2_{rt}:

$$\epsilon^*_{rt} \approx \frac{\nu^3}{{\eta^*_{k,rt}}^4} = \frac{\nu^3}{\left(\beta^{-1/2}_{rt} \eta_k\right)^4} = \beta^2_{rt} \epsilon. \tag{21}$$

This leads to a constant turbulent time scale, τ_T:

$$\tau^*_{T,rt} = \frac{k^*_{rt}}{\epsilon^*_{rt}} = \frac{\beta^2_{rt}}{\beta^2_{rt}} \frac{k}{\epsilon} = \tau_T, \tag{22}$$

and a scaled Kolmogorov time, τ_k, by the factor β^{-1}_{rt}:

$$\tau^*_{k,rt} = \left(\frac{\nu}{\epsilon^*_{rt}}\right)^{1/2} = \left(\frac{\nu}{\beta^2_{rt} \epsilon}\right)^{1/2} = \frac{1}{\beta_{rt}} \tau_k. \tag{23}$$

The Damköhler number, Da, representing macro-mixing is thus constant for a fixed chemical time scale, $\tau^*_{c,rt} = \tau_c$:

$$Da^*_{rt} = \frac{\tau^*_{T,rt}}{\tau^*_{c,rt}} = \frac{\tau_T}{\tau_c} = Da. \tag{24}$$

The Karlovitz number, Ka, that represents micro-mixing on the other hand scales with factor β_{rt}:

$$Ka^*_{rt} = \frac{\tau^*_{c,rt}}{\tau^*_{k,rt}} = \frac{\tau_c}{\beta^{-1}_{rt}\tau_k} = \beta_{rt} Ka, \tag{25}$$

which together with equation (16) leads to:

$$Ka^*_{rt} = \left(\frac{Q^*_{rt}}{Q}\right)^{1/3} Ka. \tag{26}$$

Equation (13) and (14) together with equation (24) and (26) show the inherent problem of scaling turbulent flames, namely that the non-linear character of turbulence makes it impossible to preserve both macro- and micro-mixing, even when the majority of other non-dimensional groups are neglected. Hence, one needs to decide which mixing mechanism is given the higher priority by choosing an appropriate scaling law. The present work discusses the effect of this on the combustion characteristics of of complex low emission burners, here represented by the PPBB burner.

2.2. Burner design

The present work is based on the scaling of the PPBB burner, developed by Spangelo et al. [41]. This burner is intended for the use in boilers and furnaces that typically operate at pressures close to atmospheric and with approximately 3% excess air. An illustration of the burner can be seen in figure 1. The PPBB burner employs a frustum shaped conical bluff body to stabilise the flame and allows for the dilution of the fuel-air mixture by internally recirculated flue gas. Fuel is partially premixed via jets in an accelerating cross-flow. The degree of premixing can be adjusted via eight primary and four secondary fuel ports. The primary fuel ports are located upstream of the burner throat in a converging burner section formed by the burner housing. The secondary fuel ports are located downstream of the burner throat. Primary and secondary fuel ports are, in angular direction,

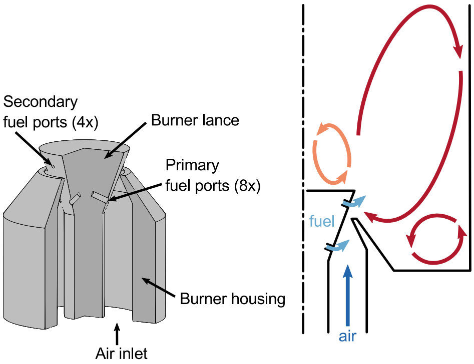

Figure 1: 3D rendering of the PPBB burner and illustration of the flow pattern. Primary and secondary fuel ports are drawn in the same plane for illustration purpose.

offset to each other such that the secondary fuel ports are located in between every other pair of primary fuel ports. The burner was in recent years investigated experimentally by Dutka et al. [7, 42–44] and numerically by Meraner et al. [45, 46] for the combustion of hydrogen and hydrogen enriched fuels. Further details on the burners operational characteristics can be found therein.

2.3. Numerical methods

The numerical model that was employed for the simulations of the PPBB burner has been developed and validated against experimental data in previous work [45, 46]. A detailed description as well as a discussion on modelling uncertainties can be found in the corresponding publications. Hence, only a short summary is given here. The model was developed with the simulation of larger scales in mind. Reducing computational costs have therefore been given a high priority, which resulted in a model based on steady state, incompressible, Reynolds averaged (RANS) governing equations. Steady state RANS simulations are order of magnitudes less computationally expensive than for example large eddy simulations. This is not only due to the lower special resolution needed for RANS simulations, but also due to the possibility to apply the steady state assumption and to utilize the periodicity of the burner (i.e., reduce the simulation to one quarter of the domain). The computational costs are further reduced by invoking non-equilibrium wall functions and by employing a post processing approach for the NO_x calculation, i.e. the NO_x calculation is decoupled from the combustion kinetics and based on a "frozen" combustion simulation. The eddy-dissipation concept (EDC) [47, 48] in combination with a detailed combustion mechanism for the hydrogen oxidation by Li et al. [49], containing 9 species and 19 reversible reactions, was used to model the turbulent combustion process. The discrete ordinates radiation model was employed to account for thermal radiation. The diffusive mass flux was calculated based on the dilute approximation (i.e., Fick's law) for turbulent flows. A grid independency study, comprising meshes ranging from 3.5 M to 14.4 M cells, was conducted for the burner at 100 kW and 500 kW scales assuming that it is valid for the intermediate scales with lower Reynolds numbers as well.

The only deviation from the original model setup presented by Meraner et al. [46] are the thermal boundary conditions for the lateral surfaces of the bluff body. These were originally modelled adiabatic. The present study has, however, shown that this unrealistic assumption leads, at certain scales, to a flame flashback within the boundary layer. The lateral bluff body walls have therefore been modelled with a constant temperature of 293 K, corresponding the air inlet temperature. A sensitivity analysis has shown that this change does not affect the global NO_x emissions.

3. Results and discussion

This section scrutinizes initially the impact of the two applied scaling laws on the burner characteristics, when the burner is scaled from laboratory scale to 50 kW and 250 kW respectively. This is followed by an analysis of NO_x emissions at different scales and parameters that are relevant for the NO_x formation. Finally the simulation of the PPBB burner with a thermal input of 500 kW, scaled using the constant velocity scaling approach, is analysed since it reveals a special case of a fundamentally different flow structure compared to all other cases.

3.1. Combustion regime and flame characteristics

Combustion regime diagrams provide a convenient tool for the visualization of flame characteristics, although one needs to keep their limitations in mind when they are utilized in the context of complex burners. Regime diagrams have historically been developed based on the interaction of homogeneous and isotropic frozen (i.e., unaffected by heat release) turbulence with a premixed flame. In order to utilize them for the partially premixed burners, special considerations need to be made. Meraner et al.[46] proposes to extract data from CFD simulations on a predefined iso-surface that is close enough to the flame, so that the mixture composition is representative for the combustion, but at a distance where the turbulence is not yet heavily affected by the heat release. This is achieved by defining an iso-surface of 5% of the maximum heat release rate, which is then clipped using a normalized progress variable (i.e., $(Y_{HO_2} + Y_{H_2O})/(Y_{HO_2} + Y_{H_2O})^{eq}$) of 0.5 as an upper limit to ensure that the data is collected on the reactants side of the flame. The data obtained on this surface is then used to categorize the flame by means of regime diagrams. Utilizing such scatter data provides a more refined insight into the burner characteristics compared to the traditional approach of describing the entire burner by a single point in the regime diagram, especially for combustion in burners which likely occurs in a multi regime mode. Representing the burner by a scatter plot furthermore allows the visualization of dependencies between local conditions, such as the equivalence ratio, and the combustion regimes. However, the overlapping of data points in densely populated scatter plots can make it difficult to identify the most representative regimes. Alternatively, hexagon binning [50], a form of bivariate histogram, can be utilized to assign a more accurate weight to different combustion regimes. This approach is employed in Figure 2 which shows the modified turbulent combustion diagram based on Peters [51] for five different CFD simulations. Here, each visible bin contains at least one data point and the colour assigned to it indicates the volume fraction that is represented by the bin. The volume calculations are based on the volume of the cells that are intersected by the predefined iso-surface. The top left subfigure shows the regime diagram for the laboratory scale burner at 10 kW. Towards the right the thermal input is increased to first 50 kW and then to 250 kW, where the top row shows constant velocity scaling and the bottom row shows constant residence time scaling. The global representation of the burner is marked by a single circular marker. The turbulent length scale, l', and the turbulent velocity scale, u', for this point are based on the area weighted average conditions in the burner throat. The laminar flame speed, S_L, and laminar flame thickness, δ_L, were calculated in the open-source software Cantera [52] based on the global equivalence ratio of the burner. In addition the effect of scaling on the flame characteristics in a global context, based on equation (13) and (14) for constant velocity scaling and equation (24) and (26) for constant residence time scaling, is outlined by a red and orange line respectively. At laboratory scale most of the flame falls into the thin reaction zone (i.e., $1 < Ka < 100$) and the corrugated flamelet (i.e., $Ka < 1$ and $u'/S_L > 1$) regimes. From previous work [46] we know that the two distinct regions seen at laboratory scale in figure 2 between $Da = 1$ and $Ka = 1$, with a volume fraction exceeding 2%, are attributed to the primary and secondary fuel streams at a equivalence ratios close to stoichiometry. The primary fuel stream is characterized by lower length scale ratios compared to the secondary fuel stream. Fuel lean flame regions fall mainly within $Ka <= 100$ and $Da <= 1$ where the Karlovitz number increases with decreasing equivalence ratio due to the decreasing flame speed.

Employing constant velocity scaling leads to decreasing Karlovitz and increasing Damköhler numbers respectively. Both the global representation of the burner as well as the peak values of the hexbin plot follow the line for the theoretical scaling. At larger scales, parts of the flame cross into the wrinkled flame regime (i.e., $u'/S_L < 1$). It can furthermore be seen that the regions assigned to the primary and secondary fuel ports are less distinct from each other with increasing thermal input and collapse to the same location at the 250 kW scale. The same is true for constant residence time scaling, where they collapse as well at 250 kW. However, the overall trend for constant residence time scaling is different. The global representation of the burner and the overall distribution shown in the hexbin plot follow the theoretical scaling with a constant Damköhler number relatively close. The peak values in the hexbin plot, however, appear to lie on an iso-line for the Karlovitz number close to unity. Further insight into the combustion characteristics can be gained by looking at figure 2 and

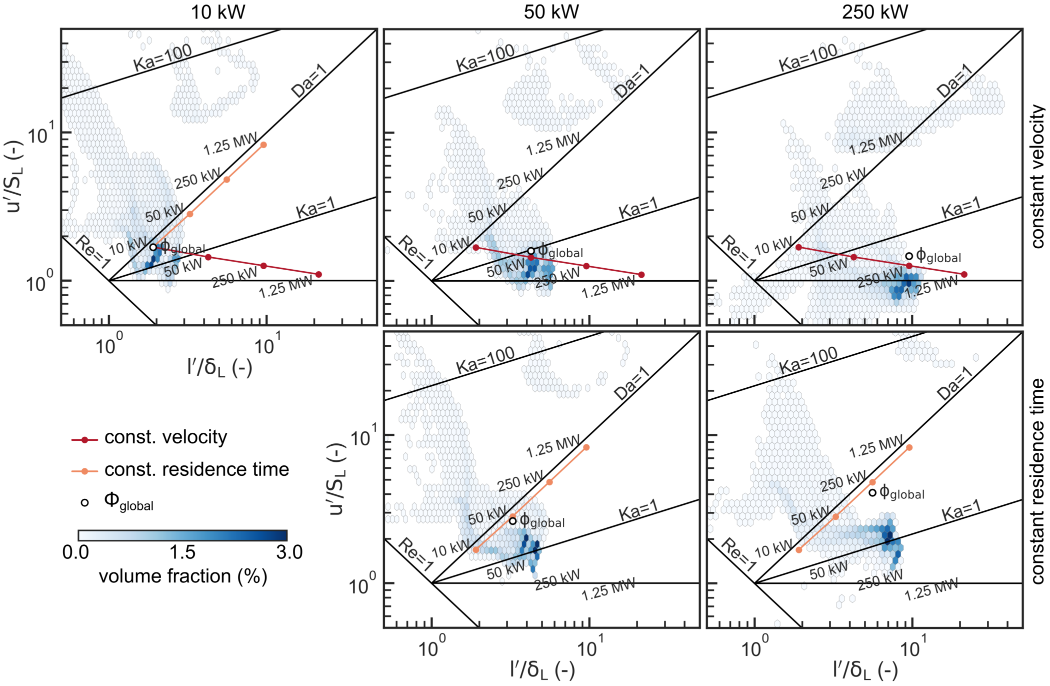

Figure 2: Modified turbulent combustion diagram based on Peters [51]. The hexbin distribution is obtained from CFD simulations and coloured by the volume fraction that is represented by each bin (i.e., the volume associated to one single bin normalized by the total volume represented in the hexbin plot). The red and orange lines show the theoretical scaling for the global burner representation. The single circular marker shows the global representation of the burner within the regime diagram.

figure 3 together. The latter shows the scatter data of the 250 kW configuration coloured by the local equivalence ratio, which has a value smaller than one under fuel lean conditions (coloured blue) and larger than one under fuel rich conditions (coloured red). Stoichiometric conditions are identified by the purple colour. The data points for the scatter plots are sorted by their distance to the stoichiometric mixture fraction. Hence, data points closer to the stoichiometric mixture overlay points that are further away from stoichiometry, independent on which side (i.e., fuel lean or rich) they are located. Figure 3a shows the regime diagram for constant velocity scaling, while figure 3b shows the same diagram for constant residence time scaling. Constant velocity scaling leads to the formation of two data point clusters. The majority of the flame is represented by Damköhler numbers larger than one. The second cluster is mainly located between $Da <= 1$ and $Ka <= 100$ and is characterised by an equivalence ratio in the range of 0.5. From the analysis of the angular coordinate, not shown here, it is known that data points in the second cluster are located in between fuel ports, which is the reason for the lean mixture. Furthermore, they have a significantly higher temperature associated to them, reaching up to 1400 K compared to the primary cluster, where the majority lies below 800 K. For both scaling approaches, a "flare" of lean data points can be seen that is leading towards larger Karlovitz numbers, due to the reduced flame speed at lean mixture fractions. Constant residence time scaling preserves the two distinct bands with a stoichiometric equivalence ratio, which have been identified by Meraner et al. [46] for the base case. Constant velocity scaling, on the other hand, shows a wider scatter of the stoichiometric mixture in the regime diagram and less distinct bands. Generally a stronger separation of lean, rich and stoichiometric mixtures within the regime diagram can be seen for constant residence time scaling, where rich equivalence ratios show the largest and stoichiometric equivalence ratio the least variation. An important parameter for the flame speed and thickness is the dilution by entrained combustion products, which cannot be identified based on the equivalence ratio only. However, mixtures close to the global and stoichiometric equivalence ratio respectively are expected to show less variation in the amount of entrained products, while mixture that are further away are expected to show more variation, which translates in a wider spread in flame speed and thickness.

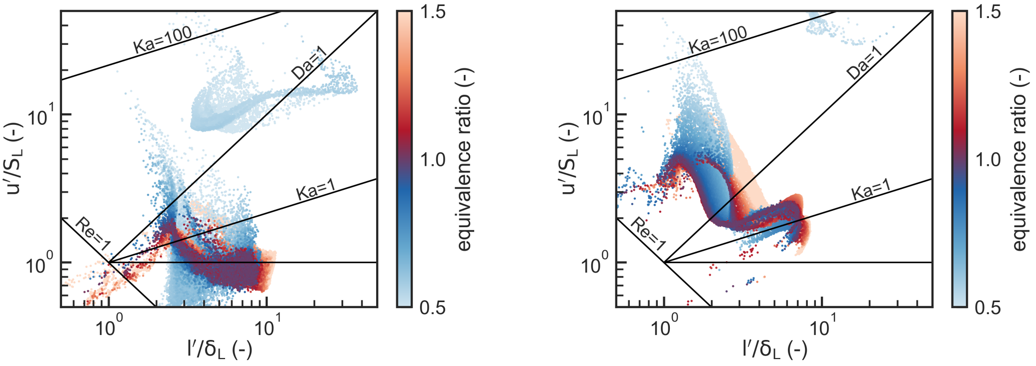

(a) constant velocity scaling

(b) constant residence time scaling

Figure 3: Modified turbulent combustion diagram based on Peters [51] containing the scatter plot for the burner at the 250 kW scale based in the two different scaling laws. The scatter plot is coloured by the local equivalence ratio. Data points closed to stoichiometric conditions overlap data points that are further away.

Figure 2 and figure 3 are per definition restricted to the flame leading edge. Figure 4, on the other hand, provides an overview on the combustion process in the whole domain by integrating the progress variable source term (i.e., $\mathrm{R}_{\mathrm{HO}_2} + \mathrm{R}_{\mathrm{H}_2\mathrm{O}}$) along the axial and radial coordinates. This allows the visualization of its probability density distribution in a two dimensional space, defined by the angular coordinate and the local equivalence ratio. In addition, marginal plots showing the probability density along the corresponding axes are provided. Figure 4 shows results from the same simulations as figure 2. The fuel port location of $+/-22.5°$ for the primary and 0° for the secondary fuel is for all cases recognizable by peaks in the equivalence ratio, defined by the location of the maximum progress variable. These peaks have values relatively close to each other for the base case at 10 kW, reaching an equivalence ratio of 1.8 (marked as B_1) in the primary fuel stream and 2.0 (marked as B_2) in the secondary fuel stream. The difference between the peak equivalence ratios in the two different fuel streams increases when constant velocity scaling is employed and is more than twice as big for the 250 kW case compared to the base case. Furthermore, both values, B_1 and B_2, are at richer equivalence ratios. This trend is opposite for constant residence time scaling where both peaks are at lower equivalence ratios and slightly closer in value to each other, when comparing the 250 kW and 10 kW simulations. However, while the peaks can be relatively clearly defined for the base case and constant velocity scaling, they are not as distinct for the constant residence time scaling, where a slower fall off can be seen.

The leanest mixtures are located in between every other pair of primary fuel ports, where no secondary fuel port is present and reaches similar equivalence ratios of 0.4–0.5 for all simulations. A difference between constant velocity and constant residence time scaling can, however, be seen in between primary and secondary fuel ports marked as point A and C respectively. Constant velocity scaling leads here (see A), with increasing thermal input, to an increase of the local progress variable source term. This can also be seen in the form of a second peak in the marginal plot marked as A', which does not appear when constant residence time scaling is employed. The local progress variable source term decreases on the other hand for constant residence time scaling, which can be seen in point C and C' respectively. Note that point C' is marked in the y-marginal plot, as it cannot be seen in equivalence ratio space, due to the peak around stoichiometry. The probability density distribution of the progress variable source term reaches for all cases its maximum around stoichiometry. However, this peak is more significant for larger thermal input and constant residence time scaling, which can be seen in location D. This indicates, in combination with the "discontinuity" discussed for point C, that the fuel streams on a macro scale are less premixed compared to the constant velocity scaling. Indeed, figure 5, which shows the stoichiometric iso-surface for the five different CFD simulations, reveals that each of the fuel stream is recognizable as a single "jet" at 250 kW when constant residence time scaling is applied. All other simulations show a continuous, though wrinkled, iso-surface and hence a fuel rich inner recirculation zone. Note that all subfigures are scaled to the same bluff body diameter. It can also be seen that the iso-surface is characterized by four tips that move closer together for constant velocity scaling and finally collapse to a single tip

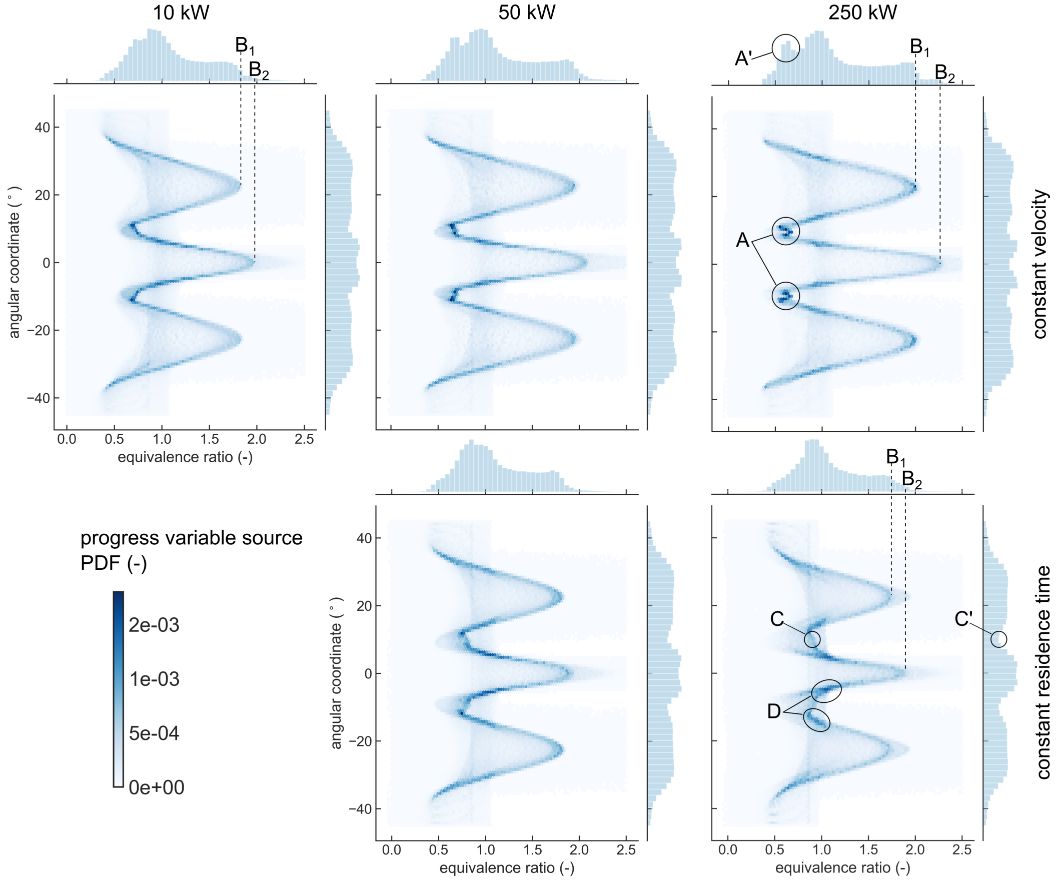

Figure 4: Hexbin plot of the the progress variable source term probability density distribution integrated along axial and radial direction, plotted in a two dimensional space formed by the equivalence ratio and the angular coordinate. The marginal plots show the probability density function of the progress variable source term along the corresponding axes.

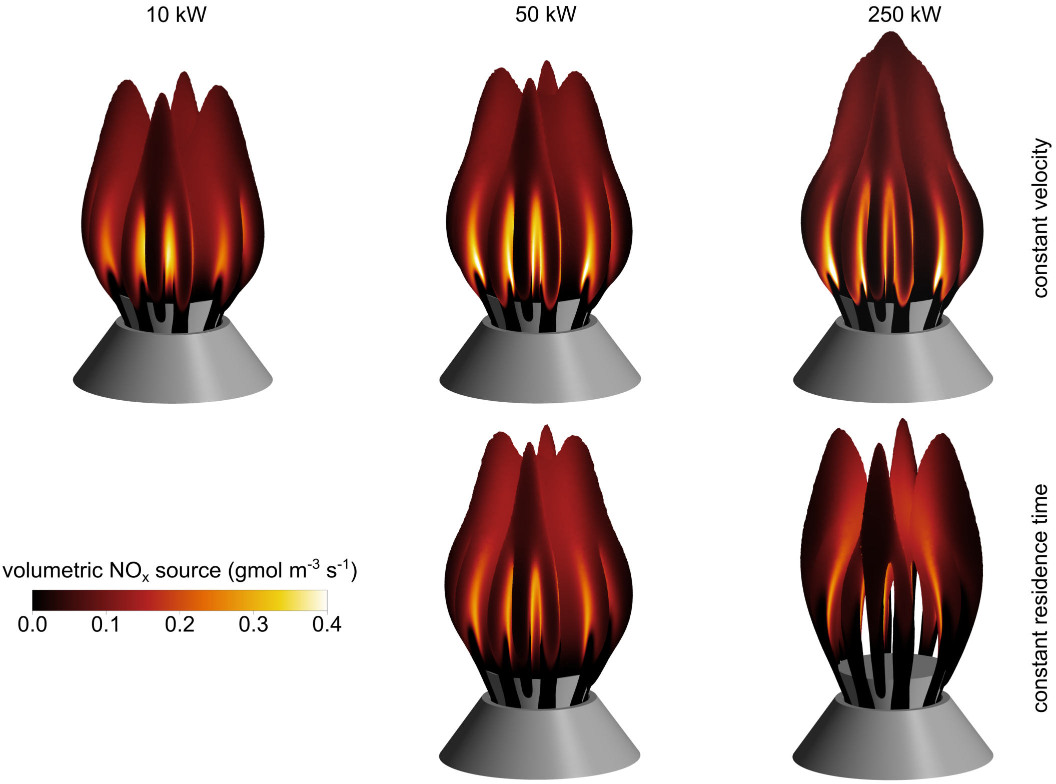

Figure 5: Iso-surface of the stoichiometric equivalence ratio coloured by the NO_x formation rate.

at 250 kW, while they get further separated when constant residence time scaling is applied.

3.2. NO_x formation

The stoichiometric iso-surface in figure 5 is coloured by the volumetric $\mathrm{NO_x}$ formation rate. The peak rate is in all cases reached in between primary and secondary fuel ports in the concave region formed by the iso-surface. This is in general the location where a stoichiometric mixture of fuel and combustion air meets hot products that are recirculated in the inner recirculation zone. At laboratory scale of 10 kW the peak values appear as a single region spanning from the primary to the secondary fuel stream. Scaling the burner up by means of constant velocity scaling leads to the formation of two separate elongated regions with elevated $\mathrm{NO_x}$ formation rates that merge again after a certain distance downstream of the bluff body trailing edge. The local peak formation rate on the stoichiometric iso-surface for constant residence time scaling is, however, generally lower compared to the constant velocity scaling approach. The overall distribution at a thermal input of 50 kW is relatively similar between the two scaling approaches. At 250 kW, on the other hand, they lead to a significant different appearance of the iso-surface. Even though clear differences can be seen in figure 5 it is not possible to conclude on the overall $\mathrm{NO_x}$ performance based on a local volumetric source term as the volumes for the different scaling approaches are significantly different. Figure 6 shows the global $\mathrm{NO_x}$ emissions at different scales for constant velocity and constant residence time scaling. Both methodologies lead to increasing $\mathrm{NO_x}$ emissions at increasing scales. However, constant velocity scaling reaches higher $\mathrm{NO_x}$ levels. None of the approaches reaches a plateau within the investigated range. Note, that the largest reported simulation for constant velocity scaling in this section is 450 kW; the 500 kW case is a special case and will be discussed in section 3.3.

The fluid domain was subdivided into six sub domains during post processing, similar to the approach presented by Hsieh et al. [29], in order to identify regions that contribute to the trend seen in figure 6. This approach is furthermore intended to provide the basis for a future development of a reduced order scaling model. The regions are the wall jet (WJ), flame (FL), inner recirculation zone (IRZ), outer recirculation zone (ORZ), immediate post flame (IPF) and post flame (PF) as illustrated in figure 7. The inner recirculation zone is defined by the central region of negative axial

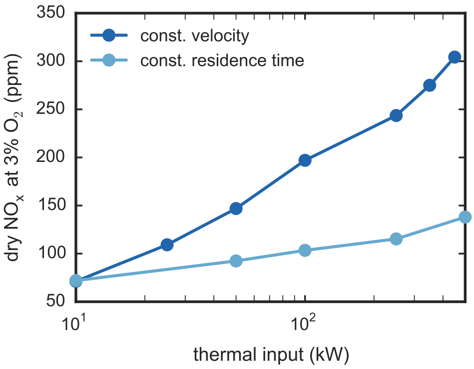

Figure 6: Global NO$_x$ emissions monitored at the chamber outlet.

velocity immediately downstream of the bluff body. The wall jet, flame and immediate post flame regions were defined based on 10% of the maximal axial velocity, while the region outside of them was assigned to the outer recirculation zone. The wall jet regions extends in axial direction until the bluff body trailing edge, followed by the flame region that extends downstream as far as the inner recirculation zone. The immediate post flame reaches from the end of the inner recirculation zone until the end of the outer recirculation zone followed by the post flame that describes the remaining flow region until the chamber outlet.

Figure 8 presents the total NO$_x$ formation rate based on the described domain subdivision. For clarity, only the three main contributing regions, immediate post flame, flame and inner recirculation zone are shown. The formation rate for all other regions is in general more than one order of magnitude smaller than the formation rate in the inner recirculation zone, confirming the findings by Hsieh et al. [29]. The constant velocity approach leads, with increasing scales, to a more rapid increase of the formation rate in the immediate post flame and flame region compared to constant residence time scaling. This difference is largest for the flame region. The inner recirculation zone on the other hand shows an opposite trend. The rate increases here for constant residence time scaling,

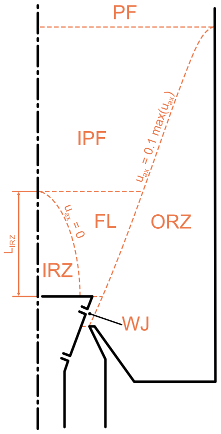

Figure 7: Illustration of the post processing regions. Note the zones are not to scale and the fuel ports are drawn in the same plane for illustration purpose.

while it stays relatively constant for constant velocity scaling.

The immediate post flame, flame and inner recirculation zone regions remain the dominating regions even when looking at NO_x formation in terms of a mean volumetric rate as shown in figure 9. However, the order of the three regions changes. The inner recirculation zone and the flame region are dominating in this context, with the inner recirculation zone having the highest volumetric rate at scales below 50 kW and the flame region dominating at scales above 50 kW. Constant residence time scaling leads in all three regions to larger volumetric NO_x formation rate than constant velocity scaling, which is the opposite trend than what was seen in figure 8 for the flame and the immediate post flame regions. This can be attributed to the different volumes and different residence times accordingly. The residence time is per definition constant for constant residence time scaling and the volumes, V, change proportional to the ratio of the thermal input $V^*/V \propto Q^*/Q$. Volumes for constant velocity scaling on the other hand increases according to $V^*/V \propto (Q^*/Q)^{3/2}$ which leads to increased residence times, promoting overall higher NO_x levels. This is in the inner recirculation

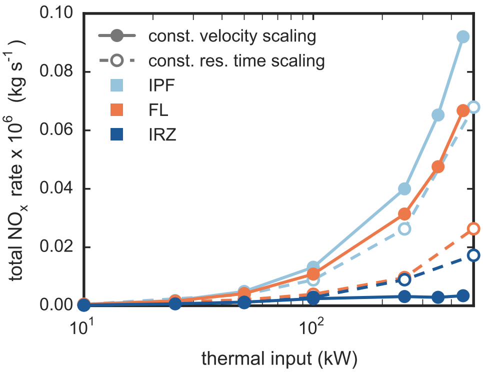

Figure 8: Volume integral of the volumetric NO_x formation rate. Solid lines and filled marker show constant velocity scaling, while dashed lines and open marker show constant residence time scaling.

zone, however, compensated by a significant decrease of the mean volumetric rate for constant velocity scaling and an increase of the mean volumetric rate for constant residence time scaling.

Analysing regional mean values has the apparent disadvantage of neglecting potentially strong local variances. This is more severe in the immediate post flame due to its large extend and the flame region where the local equivalence ratio varies significantly along the angular and radial coordinates, including rich fuel streams as seen in figure 5. A volume averaged value is thus a more reasonable representation of the inner recirculation zone, which can be interpreted as a perfectly stirred reactor. Assessing simulations by means of contour plots, on the other hand, avoids this shortcoming as can be seen in figure 10, which compares the PPBB burner at the 10 kW and the 100 kW scale based on the constant velocity scaling approach, as this represents a more severe increase in global NO_x. The contours are scaled to the same bluff body diameter, D, and the 100 kW simulation is rotated by 180° around the burner axis to allow for a direct comparison. The inner recirculation zone can be recognized by the iso-lines corresponding to zero axial velocity. The normalized dimensions of the inner recirculation zone are comparable in both cases. In general, all conducted simulations predict a recirculation zone length of approximately 1.7 D. It can be seen that, at the laboratory scale of

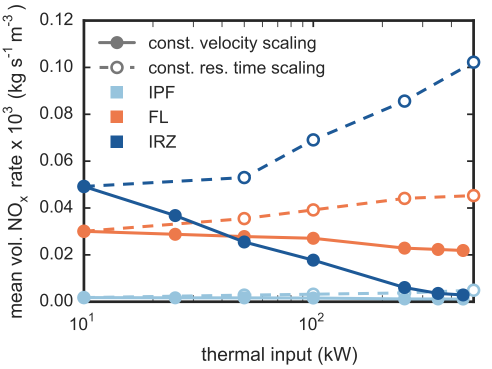

Figure 9: Volume weighted average volumetric NO$_x$ formation rate. Solid lines and filled marker show constant velocity scaling, while dashed lines and open marker show constant residence time scaling.

10 kW, mainly the upper part of the inner recirculation zone contributes to the NO$_x$ formation. The formation rate is in this region significantly lower at 100 kW. The contour plot shows furthermore a decrease of the formation rate in the flame and immediate post flame region, similar to what has been seen in figure 9. However, the local volumetric NO$_x$ formation rate close to the flame anchor point is larger for 100 kW compared to 10 kW.

Thermal NO$_x$ is the dominating NO$_x$ route for the combustion of pure hydrogen at low pressures and the temperature distribution is, therefore, an important factor for the overall NO$_x$ formation rate. Figure 11 shows the mean temperature in the three dominating regions. The mean temperature in the inner recirculation zone is relatively constant and decreasing slightly at larger scales, for both scaling methodologies. Hence, the temperature cannot be the leading cause of the different trend for constant velocity and constant residence time scaling seen in figure 9. The spacial temperature distribution within the recirculation zone is, furthermore, relatively constant while the NO$_x$ formation rate varies as has been seen in figure 10. The mean temperatures in the flame and immediate post flame region change slightly more with an approximately 8% decrease in the flame region and an similar large increase in the immediate post flame, when scaling with constant residence time from

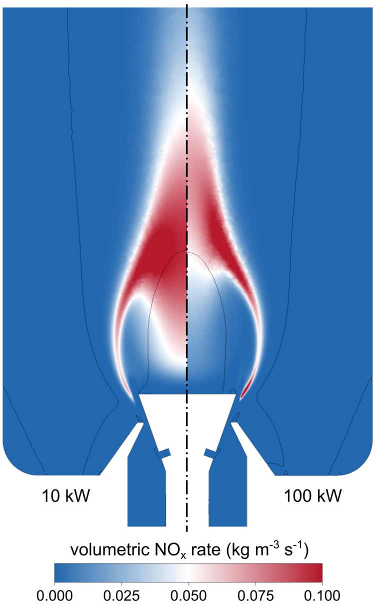

Figure 10: Volumetric NO_x formation rate contours for 10 kW (left) and 100 kW (right) thermal input, where the latter was scaled based on constant velocity scaling. The black iso-lines indicate a zero axial velocity component. Note that the dimensions in the figure are normalized by the bluff body diameter.

10 kW to 500 kW. The mean temperature stays, on the other hand, nearly constant when constant velocity scaling is employed.

Since the temperatures in the flame and inner recirculation zone are generally sufficiently high for the formation of thermal NO_x, local species concentrations become the governing factor affecting NO_x formation. Thermal NO_x formation is described by the extended Zeldovich mechanism [53]. Hence, the driving radicals are O and OH, where the latter is important particularly at near stoichiometric conditions and fuel rich mixtures. Figure 12 shows the OH mass fraction distribution for the laboratory scale burner compared to the burner scaled to 100 kW following the two investigated scaling methodologies. The iso-lines show zero axial velocity to indicate the extend of the inner

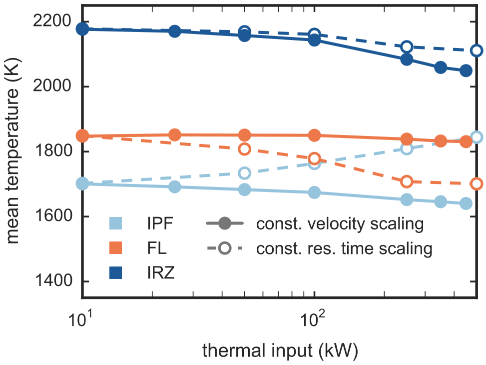

Figure 11: Volume weighted average temperature. Solid lines and filled marker show constant velocity scaling, while dashed lines and open marker show constant residence time scaling.

recirculation zone. It can be seen that the OH contours display a similar distribution as seen in figure 10 for the volumetric NO_x formation rate, with constant velocity scaling leading to lower and constant residence time scaling leading to higher OH mass fractions in the inner recirculation zone compared to the base case. A similar distribution in all three simulations was found for the O mass fraction, which is not shown here. The production of OH and O radicals is almost entirely attributed to the flame sheet. Note that this is not referring to the flame region defined for post processing. Hence, the concentration of these two radicals in the inner recirculation zone is dependent on the flow conditions and the entrainment into inner recirculation zone.

3.3. Constant velocity scaling up to 500 kW

The main flow features of the PPBB burner, namely an inner recirculation zone and a larger outer recirculation, where preserved in all simulations presented in the previous sections. The dimensions of these zones were, furthermore, relatively constant with a length of approximately 1.7 bluff body diameters for the inner and approximately 11 bluff body diameters for the outer recirculation zone. However, scaling the burner up to a scale of 500 kW based on constant velocity led to a fundamentally

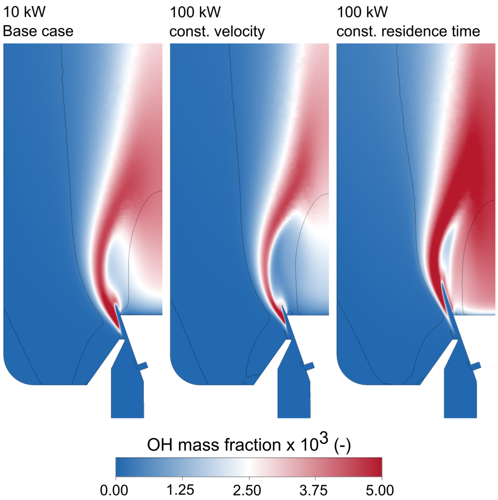

Figure 12: Contours of the OH mass fraction distribution. The black iso-lines indicate a zero axial velocity component. The size of all figures is normalized by the bluff body diameter.

different flow field, causing the flame to impinge onto the combustion chamber wall, as can be seen in figure 13. The temperature contours, overlaid by the velocity vector field for the 10 kW and the 500 kW constant velocity simulations are compared in this figure. Applying constant residence time scaling on the other hand allowed to scale the burner successfully up to 500 kW, although, with the disadvantage of reaching high velocities. The simulation of the 250 kW and 500 kW scale with constant residence time scaling reached a local Mach number of 0.35 and 0.44 respectively, which exceed the upper limit of 0.3 generally applied as best practice for incompressible solvers. Both cases are still considered as subsonic flows, however, the model uncertainties introduced by neglecting compressibility effects become larger with increasing velocities.

Figure 13 shows the breakup of the inner recirculation zone at the 500 kW scale. Instead of the inner recirculation zone a set of two equally sized vortices is formed in the outer chamber region, which was previously characterized by a single large recirculation zone and smaller secondary vortices

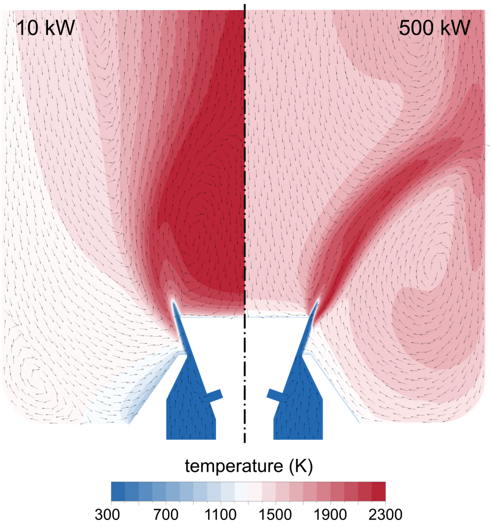

Figure 13: Temperature contours overlaid by the velocity vector field for 10 kW (left) and 500 kW (right) thermal input, where the latter was scaled based on constant velocity scaling. The size of both contours is normalized by the bluff body diameter.

in regions of flow separation from the chamber wall. Note that only one of these secondary vortices is visible due to the coarsened resolution in the vector plot. These vortices cause the flame to be bend outwards leading to an impingement of high temperature flow onto the chamber wall. The breakup of the inner recirculation zone at this scale was only observed under reacting conditions. An additional non-reacting simulation was conducted in which the original flow field, similar to the smaller scales, was preserved.

Based on the employed steady state RANS simulations it is not possible to determine if the breakup under reacting conditions is a transient flow instability or if the flow will remain permanently attach to the chamber wall. This could possibly be assessed by conducting unsteady RANS or scale resolving simulations. However, the more profound question is what causes the breakup of the inner recirculation zone. An apparent difference between the investigated scaling principles is the fuel concentration in the recirculation zone, which is an important factor for the flame stability [54]. Constant velocity scaling leads to an increased recirculation zone equivalence ratio, reaching 1.13 at the 450 kW scale, while constant residence time scaling leads to a decrease, reaching a lean equivalence ratio of 0.9 at the 500 kW scale. However, this effect is expected to be of less importance, since neither of the scaling laws leads to equivalence ratios far from stoichiometry.

Another important factor for the recirculation zone characteristic is the interaction between flow field generated by the burner and the combustion chamber, which is 3.75 bluff body diameters wide in this case. The conducted CFD simulation together with particle image velocimetry measurements by Dutka et al. [7] showed an increased recirculation zone length when the PPBB burner is operated inside of a combustion chamber compared to the unconfined configuration, which agrees with findings in the literature [55, 56]. A crucial parameter, in this context, is the blockage ratio; generally defined as the ratio of the bluff body cross-sectional area to the cross-section of the burner housing. Schefer et al. [54] found that increasing the blockage ratio from 0.25 to 0.8 increases, under certain conditions, the recirculation zone length by a factor of 2.5 and significantly increases flame stability. However, even though the ratio between chamber and bluff body as well as the blockage ratio are important for the flame stability, they cannot explain the difference between constant velocity scaling and constant residence time scaling, as ratios are preserved by the investigated scaling methodologies. Hence, the breakup of the inner recirculation zone is most likely associated with a fundamental difference between the applied scaling methodologies. An inherent difference of the investigated scaling laws is the ratio between velocity and length scales, U_0/D_0, which is per definition constant for constant residence time scaling and decreases for constant velocity scaling. Hence, the annular jet flow for constant velocity scaling has a lower momentum compared to the flow for constant residence time scaling. The recirculation zone needs, furthermore, to span a significant larger distance when constant velocity scaling is applied as the bluff body diameter is larger compared to constant residence time scaling. This may indicate that the bluff body diameter and the annular throat cross section require independent scaling similar to what has been suggested by Cheng et al. [39].

It is not yet known if the breakup of the inner recirculation zone would also occur in an unconfined burner configuration. Hence, adjusting the chamber to bluff body diameter ratio may lead to improved stability. Furthermore, the effect of different lance heights (i.e., the elevation of the bluff body with respect to the burner throat) on the recirculation zone could be explored. Tong et al. [57] suggested that the flame stability can be improved by modifying the bluff body position. However, altering the position of the conical bluff body changes inevitable also the cross-sectional throat area. This changes consequently the velocity of the annular jet flow, which will impact the flame stability as well and needs therefore to be investigated further.

4. Conclusion

Eleven CFD simulations of a complex burner configuration, at various scales ranging from 10 kW to 500 kW, were conducted. The characteristic combustion regimes and the NO_x emissions at the different scales were analysed, employing a novel approach of combining hexagonal binning and combustion regime diagrams. The scaling of the burner was conducted following two different scaling principles; the constant velocity and the constant residence time scaling.

The investigated flame is mainly characterized by the thin reaction zone regime, at laboratory scale. Employing constant velocity scaling shifts the flame towards lower Karlovitz numbers, which results in parts of the flame to burn in a non-premixed mode in the corrugated flamelet and wrinkled flamelet regimes, and other parts to burn in a premixed mode that spans multiple regimes up to Karlovitz numbers of 100. The thin reaction zone regime remains, on the other hand, representative when constant residence time scaling is employed. Constant residence time scaling preserves, furthermore, the global Damköhler number. However, the detailed analysis of the combustion characteristics by means of CFD based regime diagrams showed that a considerable part of the flame follows a constant Karlovitz number, which is unexpected in relation to the theory of constant residence time scaling and evidenced the need for individual scaling laws for different burner regions.

Increasing the burner scale led, independent of the applied scaling law, to an increase of the total NO_x emissions. No plateau was reached within the investigated range. The immediate post flame, flame and inner recirculation zone regions dominate the NO_x formation while the influence of the post flame and outer recirculation zone regions are negligible, which may explain the failure of global furnace residence time models to predict NO_x emissions at different burner scales.

Constant residence time scaling led, in the analysed burner regions, generally to larger mean volumetric NO_x formation rates, while constant velocity scaling led to higher total NO_x formation rates, which is associated with its larger volumes and longer residence times. The only exception from this observation is the inner recirculation zone, where the total NO_x formation rate is lower for constant velocity scaling than for constant residence time scaling. This was linked to the effect that the different scaling approaches have on the flow conditions and entrainment into the inner recirculation zone, which consequently affects the O atom and OH concentrations, the dominating parameter for the NO_x formation in the inner recirculation zone.

A fundamental change of the flow field was observed in the narrow band between 450 kW and 500 kW scale when constant velocity scaling was applied. At this scale the inner recirculation zone breaks up and a vortex pair is formed in the outer region of the combustion chamber that causes the flame to be bend outwards and consequently impinge onto the chamber wall. Constant residence time scaling, on the other hand, preserved the inner recirculation zone at all investigated scales. The blockage ratio, the bluff body position, and the ratio between bluff body diameter and chamber diameter are not affected by the scaling methodology. This leads to the conclusion that the sudden breakup is caused by the different effect of the scaling laws on the velocity to length scale ratio and momentum of the annular jet flow, and needs to be investigated further.

Acknowledgement

This publication has been produced with support from the BIGCCS Centre, performed under the Norwegian research program Centres for Environment-friendly Energy Research (FME). The authors acknowledge the following partners for their contributions: Gassco, Shell, Statoil, TOTAL, ENGIE and the Research Council of Norway (193816/S60). The CFD simulations were performed on resources provided by UNINETT Sigma2 - the National Infrastructure for High Performance Computing and Data Storage in Norway.

References

[1] H. Kobayashi, A. Hayakawa, K. Somarathne, E. Okafor, Science and technology of ammonia combustion, Proceedings of the Combustion Institute 37 (1) (2019) 109–133. doi:10.1016/j.proci.2018.09.029.

[2] D. Dunn-Rankin, P. Therkelsen (Eds.), Lean Combustion, 2nd Edition, Academic Press, 2016.

[3] M. Zajadatz, R. Lachner, S. Bernero, C. Motz, P. Flohr, Development and Design of Alstom's Staged Fuel Gas Injection EV Burner for NOx Reduction, in: Volume 2: Turbo Expo 2007, ASME, 2007, pp. 559–567. doi:10.1115/GT2007-27730.

[4] A. Uemichi, K. Kouzaki, K. Warabi, K. Shimamura, M. Nishioka, Formation of ultra-lean comet-like flame in swirling hydrogenair flow, Combustion and Flame 196 (2018) 314–324. doi:10.1016/j.combustflame.2018.06.019.

[5] P. Stuttaford, H. Rizkalla, Y. Chen, B. Copley, T. Faucett, Extended Turndown, Fuel Flexible Gas Turbine Combustion System, in: Volume 2: Combustion, Fuels and Emissions, Parts A and B, ASME, 2010, pp. 483–492. doi:10.1115/GT2010-22585.

[6] A. Haj Ayed, K. Kusterer, H.-W. Funke, J. Keinz, C. Striegan, D. Bohn, Improvement study for the dry-low-NOx hydrogen micromix combustion technology, Propulsion and Power Research 4 (3) (2015) 132–140. doi:10.1016/j.jppr.2015.07.003.

[7] M. Dutka, M. Ditaranto, T. Løvås, NOx emissions and turbulent flow field in a partially premixed bluff body burner with CH4 and H2 fuels, International Journal of Hydrogen Energy 41 (28) (2016) 12397–12410. doi:10.1016/j.ijhydene.2016.05.154.

[8] K. Souflas, P. Koutmos, On the non-reacting flow and mixing fields of an axisymmetric disk stabilizer, under inlet mixture stratification and preheat, Experimental Thermal and Fluid Science 99 (2018) 357–366. doi:10.1016/j.expthermflusci.2018.08.008.

[9] D. Spalding, H. Hottel, S. Bragg, A. Lefebvre, D. Shepherd, A. Scurlock, The art of partial modeling, Symposium (International) on Combustion 9 (1) (1963) 833–843. doi:10.1016/S0082-0784(63)80090-9.

[10] J. Beér, The Significance of Modelling, Journal of Insitute of Fuel 39 (1966) 466–473.

[11] S. R. Turns, Understanding NOx formation in nonpremixed flames: experiments and modeling, Prog. Energy Combust. Sci. 21 (1995) 361–385.

[12] G. A. Lavoie, A. F. Schlander, A Scaling Study of NO Formation in Turbulent Diffusion Flames of Hydrogen Burning in Air, Combustion Science and Technology 8 (5-6) (1973) 215–224. doi:10.1080/00102207308946645.

[13] N. Peters, An Asymptotic Analysis of Nitric Oxide Formation in Turbulent Diffusion Flames, Combustion Science and Technology 19 (1-2) (1978) 39–49. doi:10.1080/00102207808946862.

[14] M. C. Drake, R. J. Blint, Thermal NOx in stretched laminar opposed-flow diffusion flames with CO/H2/N2 fuel, Combustion and Flame 76 (2) (1989) 151–167. doi:10.1016/0010-2180(89)90064-3.

[15] R. Barlow, C. Carter, Raman/Rayleigh/LIF measurements of nitric oxide formation in turbulent hydrogen jet flames, Combustion and Flame 97 (3-4) (1994) 261–280. doi:10.1016/0010-2180(94)90020-5.

[16] C. D. Carter, R. S. Barlow, Simultaneous measurements of NO, OH, and the major species in turbulent flames, Optics Letters 19 (4) (1994) 299. doi:10.1364/OL.19.000299.

[17] J. Kent, R. Bilger, The prediction of turbulent diffusion flame fields and nitric oxide formation, Symposium (International) on Combustion 16 (1) (1977) 1643–1656. doi:10.1016/S0082-0784(77)80443-8.

[18] J.-Y. Chen, W. Kollmann, PDF modeling and analysis of thermal NO formation in turbulent nonpremixed hydrogen-air jet flames, Combustion and Flame 88 (3-4) (1992) 397–412. doi:10.1016/0010-2180(92)90042-N.

[19] R.-H. Chen, J. F. Driscoll, Nitric oxide levels of jet diffusion flames: Effects of coaxial air and other mixing parameters, Symposium (International) on Combustion 23 (1) (1991) 281–288. doi:10.1016/S0082-0784(06)80271-7.

[20] N. Smith, R. Bilger, J.-Y. Chen, Modelling of nonpremixed hydrogen jet flames using a conditional moment closure method, Symposium (International) on Combustion 24 (1) (1992) 263–269. doi:10.1016/S0082-0784(06)80035-4.

[21] G. Szego, B. Dally, G. Nathan, Scaling of NOx emissions from a laboratory-scale mild combustion furnace, Combustion and Flame 154 (1-2) (2008) 281–295. doi:10.1016/j.combustflame.2008.02.001.

[22] S. R. Turns, F. H. Myhr, Oxides of nitrogen emissions from turbulent jet flames: Part IFuel effects and flame radiation, Combustion and Flame 87 (3-4) (1991) 319–335. doi:10.1016/0010-2180(91)90116-S.

[23] S. R. Turns, F. H. Myhr, R. V. Bandaru, E. R. Maund, Oxides of nitrogen emissions from turbulent jet flames: Part IIFuel dilution and partial premixing effects, Combustion and Flame 93 (3) (1993) 255–269. doi:10.1016/0010-2180(93)90107-E.

[24] A. Lutz, R. Kee, R. Dibble, J. Broadwell, A model for detailed chemical kinetics in turbulent nonpremixed jet flames, in: 29th Aerospace Sciences Meeting, American Institute of Aeronautics and Astronautics, Reston, Virigina, 1991. doi:10.2514/6.1991-478.

[25] N. A. Røkke, J. E. Hustad, O. K. Sønju, A study of partially premixed unconfined propane flames, Combustion and Flame 97 (1) (1994) 88–106. doi:10.1016/0010-2180(94)90118-X.

[26] A. Santos, M. Costa, Reexamination of the scaling laws for NOx emissions from hydrocarbon turbulent jet diffusion flames, Combustion and Flame 142 (1-2) (2005) 160–169. doi:10.1016/j.combustflame.2005.03.004.

[27] R. Weber, Scaling characteristics of aerodynamics, heat transfer, and pollutant emissions in industrial flames, Symposium (International) on Combustion 26 (2) (1996) 3343–3354. doi:10.1016/S0082-0784(96)80182-2.

[28] S. Joo, J. Yoon, J. Kim, M. Lee, Y. Yoon, NOx emissions characteristics of the partially premixed combustion of H2/CO/CH4 syngas using artificial neural networks, Applied Thermal Engineering 80 (2015) 436–444. doi:10.1016/j.applthermaleng.2015.01.057.

[29] T.-C. Hsieh, W. J. Dahm, J. F. Driscoll, Scaling Laws for NOx Emission Performance of Burners and Furnaces from 30 kW to 12 MW, Combustion and Flame 114 (1-2) (1998) 54–80. doi:10.1016/S0010-2180(97)00289-7.

[30] M. Sadakata, Y. Hirose, Scaling law for pollutant emission from a combustion furnace, Fuel 73 (8) (1994) 1338–1342. doi:10.1016/0016-2361(94)90310-7.

[31] R. Weber, J. F. Driscoll, W. J. Dahm, R. T. Waibel, Scaling Characteristics of Aerodynamics and Low-NOx Properties of Industrial Natural Gas Burners. The SCALING 400 Study. Part I: Test Plan, Tech. rep., GRI Topoical Report 93/0227, Gas Research Institute, Chicago (1993).

[32] U. Bollettini, F. Breussin, R. Weber, A study on scaling of natural gas burners, IFRF Combustion Journal.

[33] R. Weber, F. Breussin, Scaling properties of swirling pulverized coal flames: From 180 kW to 50 MW thermal input, Symposium (International) on Combustion 27 (2) (1998) 2957–2964. doi:10.1016/S0082-0784(98)80155-0.

[34] N. Megalos, N. Smith, D. Zhang, The potential for low NOx from a precessing jet burner of coal, Combustion and Flame 124 (1-2) (2001) 50–64. doi:10.1016/S0010-2180(00)00173-5.

[35] J. M. Ballester, C. Dopazo, N. Fueyo, M. Hernández, P. J. Vidal, Investigation of low-NOx strategies for natural gas combustion, Fuel 76 (5) (1997) 435–446. doi:10.1016/S0016-2361(97)85521-4.

[36] J. P. Smart, W. L. D. Van Kamp, The Impact of Scaling Criteria on the Characteristics of Pulverised Coal Flames, Developments in Chemical Engineering and Mineral Processing 7 (3-4) (1999) 301–331. doi:10.1002/apj.5500070305.

[37] J. A. Cole, T. P. Parr, N. C. Widmer, K. J. Wilson, K. C. Schadow, W. R. Seeker, Scaling criteria for the development of an acoustically stabilized dump combustor, Proceedings of the Combustion Institute 28 (1) (2000) 1297–1304. doi:10.1016/S0082-0784(00)80343-4.

[38] S. Kumar, P. J. Paul, H. S. Mukunda, Investigations of the scaling criteria for a mild combustion burner, Proceedings of the Combustion Institute 30 II (2) (2005) 2613–2621. doi:10.1016/j.proci.2004.07.045.

[39] R. Cheng, D. Yegian, M. Miyasato, G. Samuelsen, C. Benson, R. Pellizzari, P. Loftus, Scaling and development of low-swirl burners for low-emission furnaces and boilers, Proceedings of the Combustion Institute 28 (1) (2000) 1305–1313. doi:10.1016/S0082-0784(00)80344-6.

[40] B. Farcy, L. Vervisch, P. Domingo, Large eddy simulation of selective non-catalytic reduction (SNCR): A downsizing procedure for simulating nitric-oxide reduction units, Chemical Engineering Science 139 (2015) 285–303. doi:10.1016/j.ces.2015.10.002.

[41] Ø. Spangelo, O. Sonju, T. Slungaard, M. Ditaranto, US 20090220899 A1 (2009).

[42] M. Dutka, Emissions of nitrogen oxides from partially premixed flames stabilized on a conical bluff body, Ph.D. thesis, NTNU (2015).

[43] M. Dutka, M. Ditaranto, T. Løvås, Application of a Central Composite Design for the Study of NOx Emission Performance of a Low NOx Burner, Energies 8 (5) (2015) 3606–3627. doi:10.3390/en8053606.

[44] M. Dutka, M. Ditaranto, T. Løvås, Emission characteristics of a novel low NO x burner fueled by hydrogen-rich mixtures with methane, Journal of Power Technologies 95 (2) (2015) 105–111.

[45] C. Meraner, T. Li, M. Ditaranto, T. Løvås, Cold flow characteristics of a novel bluff body hydrogen burner, International Journal of Hydrogen Energy 43 (14) (2018) 7155–7168. doi:10.1016/j.ijhydene.2018.02.062.

[46] C. Meraner, T. Li, M. Ditaranto, T. Løvås, Combustion and NO x Emission Characteristics of a Bluff Body Hydrogen Burner, Energy & Fuels (2019) acs.energyfuels.9b00313doi:10.1021/acs.energyfuels.9b00313.

[47] B. Magnussen, On the structure of turbulence and a generalized eddy dissipation concept for chemical reaction in turbulent flow, in: 19th Aerospace Sciences Meeting, American Institute of Aeronautics and Astronautics, Reston, Virigina, 1981, pp. 1–6. doi:10.2514/6.1981-42.

[48] B. Magnussen, B. Hjertager, On mathematical modeling of turbulent combustion with special emphasis on soot formation and combustion, Symposium (International) on Combustion 16 (1) (1977) 719–729. doi:10.1016/S0082-0784(77)80366-4.

[49] J. Li, Z. Zhao, A. Kazakov, F. L. Dryer, An updated comprehensive kinetic model of hydrogen combustion, International Journal of Chemical Kinetics 36 (10) (2004) 566–575. doi:10.1002/kin.20026.

[50] N. Lewin-Koh, Hexagon Binning: an Overview, Tech. rep., TU Dortmund (2009).

[51] N. Peters, The turbulent burning velocity for large-scale and small-scale turbulence, Journal of Fluid Mechanics 384 (1999) S0022112098004212. doi:10.1017/S0022112098004212.

[52] D. G. Goodwin, R. L. Speth, H. K. Moffat, B. W. Weber, Cantera: An object-oriented software toolkit for chemical kinetics, thermodynamics, and transport processes (2018). doi:10.5281/zenodo.1174508.

[53] Y. B. Zeldovich, The oxidation of nitrogen in combustion and explosions, Acta Physicochimica U.R.S.S. 21 (1946) 577–628.

[54] R. W. Schefer, M. Namazian, J. Kelly, M. Perrin, Effect of Confinement on Bluff-Body Burner Recirculation Zone Characteristics and Flame Stability, Combustion Science and Technology 120 (1-6) (1996) 185–211. doi:10.1080/00102209608935573.

[55] D. F. G. Durão, J. H. Whitelaw, Velocity characteristics of the flow in the near wake of a disk, Journal of Fluid Mechanics 85 (02) (1978) 369. doi:10.1017/S0022112078000683.

[56] A. M. K. P. Taylor, J. H. Whitelaw, Velocity characteristics in the turbulent near wakes of confined axisymmetric bluff bodies, Journal of Fluid Mechanics 139 (-1) (1984) 391. doi:10.1017/S0022112084000410.

[57] Y. Tong, M. Li, J. Klingmann, S. Chen, Z. Li, Experimental Investigation on the Influences of Bluff-Body's Position on Diffusion Flame Structures, in: Volume 1: Boilers and Heat Recovery Steam Generator; Combustion Turbines; Energy Water Sustainability; Fuels, Combustion

and Material Handling; Heat Exchangers, Condensers, Cooling Systems, and Balance-of-Plant, ASME, 2017, p. V001T04A009. doi:10.1115/POWER-ICOPE2017-3090.

ISBN 978-82-326-4164-2 (printed version)
ISBN 978-82-326-4165-9 (electronic version)
ISSN 1503-8181

NTNU
Norwegian University of
Science and Technology

Christoph Meraner

Doctoral theses at NTNU, 2019:284

NTNU

Doctoral Thesis

NTNU
Norwegian University of
Science and Technology
Faculty of Engineering
Department of Energy and Process Engineering

Doctoral theses at NTNU, 2019:284

Christoph Meraner

On the Scalability of a Partially Premixed Low NO_x Hydrogen Burner

NTNU
Norwegian University of
Science and Technology